Quantitative Electron Paramagnetic Resonance Studies of Charge Transfer in Organic Semiconductors

Dissertation zur Erlangung des
naturwissenschaftlichen Doktorgrades
an der Julius-Maximilians-Universität Würzburg

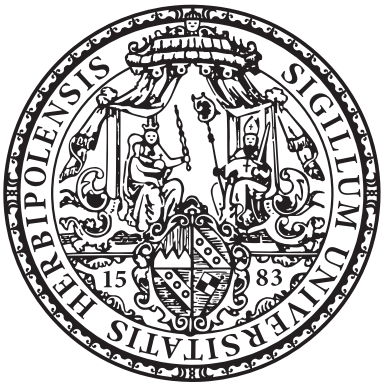

vorgelegt von

Michael Tilman Auth

aus Neustadt am Main

Würzburg 2019

Eingereicht am: 02.07.2019
bei der Fakultät für Physik und Astronomie

1. Gutachter: Prof. Dr. Vladimir Dyakonov
2. Gutachter: Prof. Dr. Tobias Hertel
3. Gutachter:
der Dissertation.

Vorsitzende(r):
1. Prüfer: Prof. Dr. Vladimir Dyakonov
2. Prüfer: Prof. Dr. Tobias Hertel
3. Prüfer: Prof. Dr. Bernd Engels
im Promotionskolloquium.

Tag des Promotionskolloquiums: 08.10.2019

Doktorurkunde ausgehändigt am:

Contents

1 Introduction

"And god created all vegetation and all living creatures on the planet"
Book of Genesis, a novel a few hundred years a. Chr. n.

Only centuries ago people believed, and some still do nowadays, that the versatility of all living things on the planet is a proof of god. That is of course a topic that belongs in the world of beliefs. But what we do know now is that the beauty and versatility of life is proof of the versatility of carbon, often discussed as the true "source of life". Life is on this planet because carbon can form complex structures, among them the most complex of all, DNA. If we take a look into the carbon-related discoveries of the last centuries we end up with an uncountable number of publications spread over all different fields of research. Similarly, this work investigates carbon structures of various flavours in shapes like chains, rings, balls, and even tubes. Regarding these structures, the process of charge transfer was the one we focused on. First, we want to talk about special carbon structures already used in devices improving our quality of life by supplying energy from light. In the field of solar energy organic photovoltaics (OPV) [1] could deliver devices with extremely short amortization times of only a few years as shown in recent publications [2], similar to the new emerging perovskite solar modules [3]. As even the youngest among us know and demand in their "Fridays for Future" demonstrations, this is exactly what we need to limit the global temperature increase to 2°C, an aim stated in the 2015 United Nations Climate Change Conference in Paris [4]. Solar cells take the energy deposited on the planet by the sun to generate electricity we can then use without depleting other resources. In this work we will elucidate the energetic landscape of an OPV cell via electron paramagnetic resonance (EPR) to learn more about the interactions of orbitals, namely in fullerene based devices.
If we do not stop at organic solar cells but also think about the whole field of electronics, we end up at organic transistors. One of the most promising candidates there, the single-wall carbon nanotube (SWNT) has been intensively investigated for a few years, recently yielding preliminary results [5, 6]. For their application, *p*- and *n*-doping of the organic materials has to be possible. Being able to control the type and amount of charge carriers is a general challenge of modern electronics. Therefore, by means of quantitative EPR we will investigate the unintentional as well as deliberate doping of

semiconducting (6,5)-SWNTs. Here we don't want to forget to mention that nanotubes are also useful for nano biology "electronics". Nanotubes connect or boost signals of neuronal synapses in brain cells [7, 8] for neural prosthetics with synthetic brain material or others.
These semiconducting SWNTs are also promising candidates to improve already working devices due to their unique structure and electronic properties. In the final chapter of this work we will investigate their possible contribution in the case of the aforementioned OPV cells. The focus is set on charge transfer (CT) between the (6,5)-SWNTs and polymers as well as fullerenes, investigated by EPR.
In this work we start with a detailed introduction to the physics behind electron paramagnetic resonance. Afterwards, the complex structures formed by carbon are presented. How they were investigated via EPR spectroscopy is given separately. The first chapter of results focuses on CT in OPV cells. The second chapter of results is split into three subsections, starting with the unintentional as well as deliberate doping of SWNTs. The last section is a cross section presenting the CT properties of SWNTs with OPV materials. Every chapter starts with an individual introduction. Since continuous wave (CW)-EPR measurements are a valuable source of information for various interactions on a molecular level, we investigated many other systems too. Supporting information we gained for other projects at our department or the graduate college GRK 2112, for which I was the doctoral students representative, were partly published and are listed in the publications in the end.

2 Electron Paramagnetic Resonance (EPR) Theory

In this chapter we will take a look at the general physical background necessary for this work. In the beginning we will introduce the concept of spin and the various ways it interacts with its environment. Afterwards we will briefly see how we put that into practise to perform electron spin resonance, i.e. electron paramagnetic resonance (EPR) experiments. Finally, we will take a closer look at the parameters influencing the EPR signal shape, intensity, and the information we can determine thereof. Theoretical background only useful in distinct chapters of this work will be explained in the beginning of the corresponding ones.

2.1 Spin Physics

2.1.1 The Magnetic Moment of an Electron

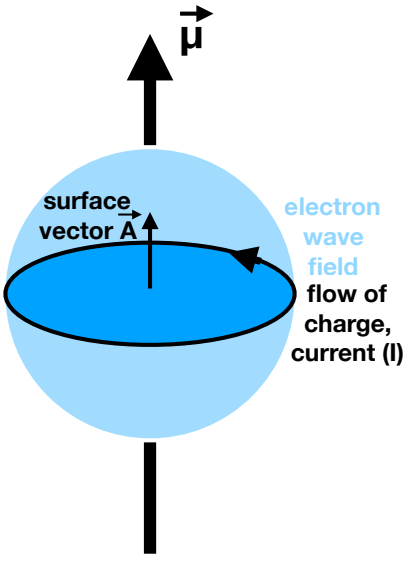

Figure 2.1: Visualisation of the electron's spin.

To get a better feeling for the 'mysterious' spin property we want to note that the picture of the spin as a rotating charge is wrong and should rather be seen as an angular momentum, which is caused by a flow of energy in the (electrons) wave field. This is nicely derived in a theoretical paper by Ohanian bearing the fitting name "what is spin" [9]. Accordingly, the electron's magnetic moment can be seen as caused by a flow of charge in its' own wave field as shown in Figure 2.5. There, we give the quantum mechanical as well as the classical properties as a visualisation for the reader. For simplicity, the following section relates to classical descriptions of the magnetic moment that can be found in [10, 11, 12, 13, 14]:

$$\vec{\mu} = I\vec{A} \tag{2.1}$$

where I represents the ring current, caused by the electron, and $\vec{A}$ the surface vector being perpendicular to the surface bounded by the electron's ring current. Classically, this ring current is caused by an angular momentum $\vec{L} = m\vec{\omega}r^2$, including the particle mass m, angular frequency ω and radius r. Together with the ring current $I = \frac{q}{T} = \frac{-e\omega}{2\pi}$, including the particle's charge q and period T, we derive the magnetic moment:

$$\vec{\mu} = \frac{-e}{2m_e}\vec{L} = \frac{-e\hbar}{2m_e}\frac{\vec{L}}{\hbar}$$

where $\frac{e\hbar}{2m_e} = \mu_B$ is the Bohr magneton, including the electron's elementary charge e, mass m_e and the reduced Planck constant $\hbar$. If we now place a spin inside a static external magnetic field a torsional moment appears causing the magnetic moment to precesses around it. The angular momentum L doesn't change its absolute value, but its orientation

$$\vec{L} = \vec{\mu} \times \vec{B} = \frac{-\mu_B}{\hbar}(\vec{L} \times \vec{B}) \tag{2.2}$$

with the frequency $\omega_L = \frac{\vec{\mu_B}\vec{B}}{\hbar}$. Paul Dirac's relativistic quantum theory [15] predicts a spin correction factor g, confirmed by experiments, yielding the Larmor frequency:

$$\omega_L = \frac{\mu_B g B_z}{\hbar} = g\gamma B_z \tag{2.3}$$

including the gyromagnetic ratio γ. This Larmor frequency is exactly the frequency needed to flip a spin. The free electron's g-factor g_e can be exactly calculated theoretically in quantum electrodynamics (QED) and is measured to an incredible accuracy of $1.7 \cdot 10^{-13}$ being $g_e = 2.00231930436256(35)$ [16]. For the most general case of an electron with both spin (s) and orbital angular momentum (l) we define the total angular momentum $\vec{J} = \vec{S} + \vec{L}$ ranging from $|S-L|, |S-L+1|, ...|S+L|$. Finally, we determine the magnetic moment to be:

$$\vec{\mu} = -\left(\frac{3}{2} + \frac{S(S+1) - L(L+1)}{2J(J+1)}\right)\mu_B\frac{\vec{J}}{\hbar} = -g_j\mu_B\frac{\vec{J}}{\hbar} \tag{2.4}$$

with the g-factor g_j, named Landé factor. This g-value is thus a measure of the spin-orbit coupling (SOC), i.e. the contribution of the spin and orbital motion to its total angular momentum [17].

2.1.2 The Spin Hamiltonian

As the source and character of the quantum mechanical spin is now determined, we will elucidate it's numerous interactions. The general spin hamiltonian for more than one electron interacting with nuclear spins was first derived by Abragam and Pryce as a part of the overall hamiltonian [18]. For convenience it is presented as in Stefan Stolls thesis [19]. If one wants to calculate the spin hamiltonian for his system ab initio, his work is highly recommended. He also wrote the EPR spectra simulation program easyspin used for all simulations done in this work [20]. Similar descriptions but with a slightly different perspective helpful to the reader are given by Assenheim [17], Bolton and Weil [21]. Manifestations of the various spin interactions are step wise explained, simulated and presented together with exemplary EPR spectra in [22]. The hamiltonian is

$$\begin{aligned}\mathscr{H} &= \mathscr{H}_{EZI} + \mathscr{H}_{HFI} + \mathscr{H}_{ZFI} + \mathscr{H}_{EEI} + \mathscr{H}_{NZI} + \mathscr{H}_{NQI} \\ &= \mu_B \vec{S}\mathbf{g}\vec{B} + \vec{S}\mathbf{A}\vec{I} + \vec{S}\mathbf{D}\vec{S} - \vec{S}_1\mathbf{J}\vec{S}_2 - \mu_N\vec{B}\mathbf{g_N}\vec{I}_Z + \vec{I}\mathbf{Q}\vec{I}\end{aligned} \tag{2.5}$$

with vectors and matrices shown as $\vec{X}$ and $\mathbf{X}$, respectively. The various interactions are presented schematically in Figure 2.2a for a system of two electrons and two nuclei in an external magnetic field B.

- $\mathscr{H}_{EZI}$: Electron Zeeman interaction of electron spin 1 with B
- $\mathscr{H}_{HFI}$: Hyperfine interaction between electron spin 1 and nuclear spin 1
- $\mathscr{H}_{ZFI}$: Zero-Field interaction for an electron spin system S>1/2
- $\mathscr{H}_{EEI}$: Electron Exchange interaction between electron 1 and 2
- $\mathscr{H}_{NZI}$: Nuclear Zeeman interaction of nuclear spin 1 with B
- $\mathscr{H}_{NQI}$: Nuclear quadrupole interaction for a spin system I>1/2

To get an idea about the strength of the interactions a valuation in Hz is given in Figure 2.2b with values from [10] and [23].

$\mathscr{H}_{EZI}$ Electron Zeeman Interaction

The interaction of ions with an external magnetic field has first been observed by Pieter Zeeman in 1896 [24]. He deduced the ion's motion, which we now know as spin, as the reason for the widening of optical lines in flames. Stern and Gerlach discovered the quantisation of the ion motion's angular momentum in 1922 by the deflection of a silver atom beam in an inhomogeneous magnetic field [25]. They concluded the parallel and antiparallel alignment of the particle's magnetic moment with respect to the external

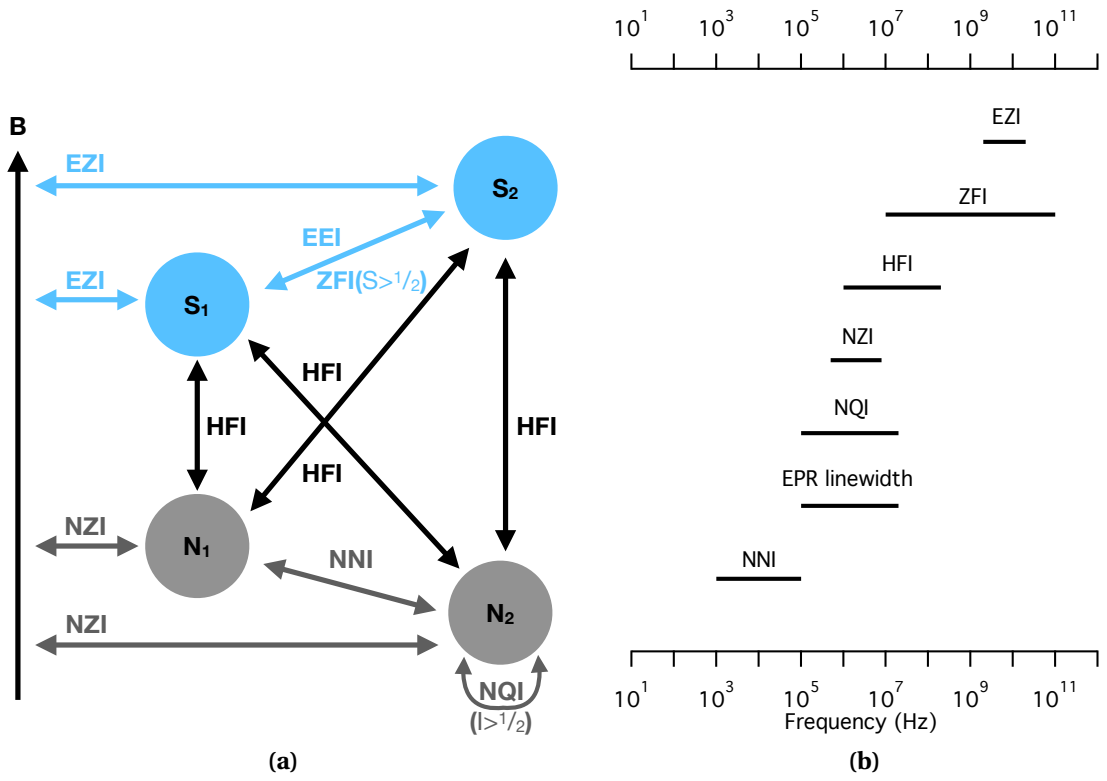

Figure 2.2: Various interactions for two electrons and two nuclei in an external magnetic field and their possible interaction strengths in Hz. For comparison: 1 G=0.1 mT=2.8 MHz=9.34·10^{-5}1/cm=1.1·10^{-3}J/mol.

magnetic field. Two cases of this quantisation are observable, called the normal and the anormal Zeeman effect. There we need to consider the angular momentum quantum number $J = S + L$, including the total spin quantum number $S = \sum_i s_i$, a sum over all spins, and the total orbital angular momentum quantum number $L = \sum_i l_i$, a sum over all momenta. On the one hand we have the normal Zeeman effect which considers only even numbers of electrons, yielding $S = 0$. In this case a correct description is possible by only considering L. On the other hand there is the anormal Zeeman effect, actually representing the more general case by considering both S and L. The name is misleading but historically defined by the chronology of the discoveries. Hence, the atomic magnetism generally results from the particles orbital momentum and its spin. The Zeeman energy for such a particle is given by:

$$E_{Zeeman} = -g\mu_B B m_J \tag{2.6}$$

including the g-factor g, the Bohr magneton μ_B, the external magnetic field, or more precisely, the magnetic induction B and the projection of the angular momentum quantum number on the direction of B, m_J. The unpaired electron in organic radicals

mostly exhibits an orbital momentum close to zero (L≈0). Thus J almost equals S and g≈2.

$\mathcal{H}_{HFI}$ Hyperfine Interaction

The hyperfein interaction (HFI) has to be taken into account if electrons couple to nuclear spins. Therefore, we get additional contributions from dipole-dipole as well as exchange (Fermi-contact) interactions. As we have seen previously, the HFI Hamiltonian is given as

$$\mathcal{H}_{HFI} = \vec{S} \cdot \mathbf{A} \cdot \vec{I}$$

with **A**=a_{iso}+T'. The isotropic contribution due to the Fermi-contact is

$$a_{iso} = \frac{2\mu_0}{3} g_e \mu_B g_N \mu_N \rho_N$$

with ρ_N the spin density at a certain nucleus N. T represents the anisotropic part of the dipole-dipole interaction of the electron's and nucleus' spin with

$$T = \frac{\mu_0}{4\pi} g_e \mu_B g_N \mu_N \left[\frac{3\vec{r}\vec{r}}{r^5} - \frac{1}{r^3} \right]$$

$\vec{r}$ is the distance between both dipoles in a point dipole approximation. T' would also contain the spin-orbit coupling (SOC) of the electron's orbital motion with the nucleus. As it is negligible for all couplings in organic radicals, we stay with T [22].
If hyperfine interactions are observable, further hamiltonians considering the nuclear zeeman interaction $\mathcal{H}_{NZI}$ and for a total nuclear spin I>1/2 the nuclear quadrupole interaction $\mathcal{H}_{NQI}$ is non-zero. It should be noted that both are merely visible in CW-EPR as they are both in the range of the homogeneous linewidth (see Figure 2.2b). Furthermore, without intermixing of the electron and nuclear spin states the NZI can't be detected in EPR, as shown in Figure 2.3a.

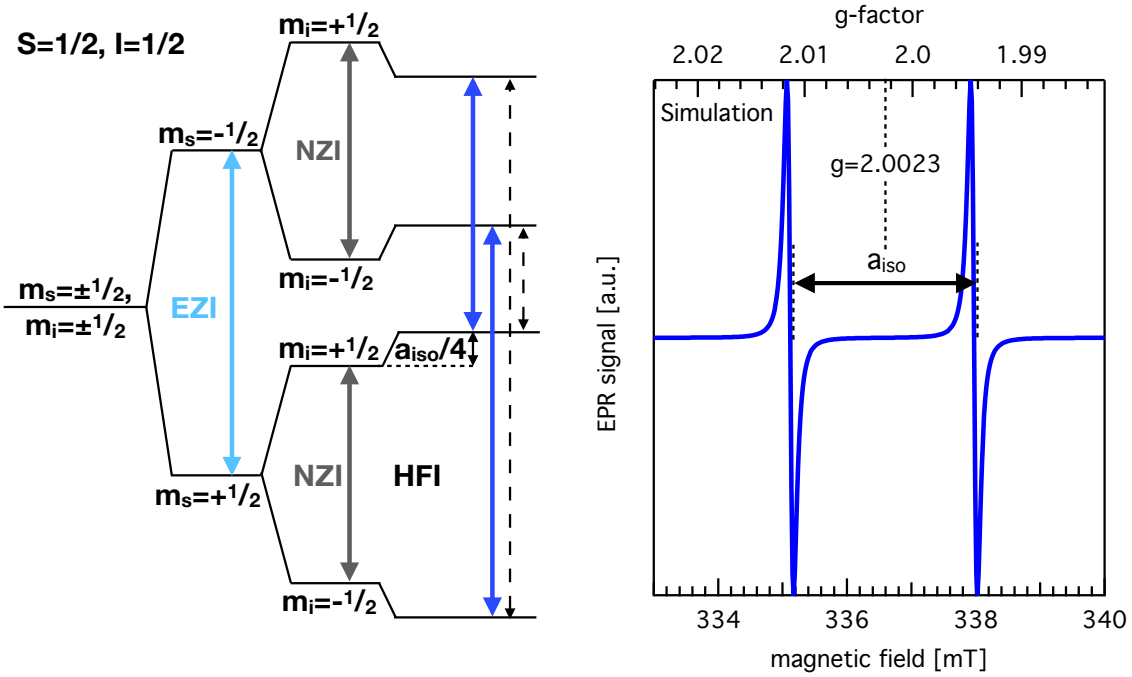

Figure 2.3: a) Energy levels for a S=1/2 system coupling to an I=1/2 nucleus. The solid black arrows are the allowed transitions according to the selection rules $\Delta m_s = 1$, $\Delta m_i = 0$ for non intermixing spin states, i.e. samples in solution. For intermixing spin states, i.e. solid samples, the forbidden transitions (black dashed arrows) become partly allowed. A corresponding EPR spectrum is shown exemplarily in **b)**

Figure 2.3a illustrates a s=1/2 system coupling to an i=1/2 nucleus. There, we assume only isotropic interaction as we would for samples in solution where brownian motion averages out all anisotropic contributions. Therefore, we restrict the hamiltonian to not intermixing spin states, i.e. only the $S_z I_z$ contributions from $A_{\alpha\omega} S_\alpha I_\omega$ with $\alpha = X, Y, Z$ and $\omega = x, y, z$. This is called the high field approach mostly fulfilled for radicals at X-Band. It simply states that the EZI dominates all other interactions. Therefore, we consider the EZI, the NZI and the HFI:

$$\begin{aligned} H_{s=1/2,i=1/2} &= \frac{2\pi}{h} g_e \mu_B B_0 S_z + \frac{2\pi}{h} g_n \mu_B B_0 I_z + \frac{a_{iso}}{\hbar^2} S_z I_z \\ &= -g_e \mu_B B_0 m_s + g_n \mu_B B_0 m_i + a_{iso} m_s m_i \end{aligned} \tag{2.7}$$

In solid state we would need to consider anisotropic interactions as well, i.e. intermixing spin states with $S_z I_x$, $S_z I_y$. Where we again used the high field approach to ignore S_y and S_x. This case is quantitatively similar to what is depicted in Figure 2.3a, just with another hyperfine splitting a instead of a_{iso} and a corrected NZI, both due to the effect of the electron spin on the different nuclear spin orientations. Most interestingly, the forbidden transitions with $\Delta m_S = \pm 1$, $\Delta m_I = \pm 1$ become partly allowed.

$\mathscr{H}_{ZFI}$ Zero-Field Interaction

For a spin system with S>1/2, i.e. single occupied orbitals in a single atom or molecule we observe dipole-dipole interactions as well as the SOC of the corresponding magnetic moments. Together they are summed up as zero-field interaction (ZFI) as they are field independent. They do lift the states degeneracy at zero field and give valuable chemical information about the binding states structure. High ZFI can indicate low symmetry while quantum chemical calculations can then determine the bonding character [22].

$\mathscr{H}_{EEI}$ Electron-Exchange Interaction

In the case of two interacting electrons from two atoms or molecules we need to consider dipole-dipole coupling and SOC as well as the wave function overlap. For organic biradicals the exchange interaction J is mostly dominated by the overlap of the electrons' wave functions. The EEI is basically an electron pair binding, only visible if it is weak and therefore no antiparallel alignment of the spins occurs, i.e. $S \neq 0$. Generally, ferromagnetic interaction results in a high spin, i.e. S=1 triplet state, while antiferromagnetic interaction yields a S=0 singlet. The former might be explained by the Hund's rule dictating maximum spin in degenerate orbitals, the later with antiparallel spins for electrons in the same orbital according to the Pauli principle.

2.1.3 Simulation of EPR Spectra

All EPR spectra simulations in this work were carried out using EasySpin Versions (5.0.19) till (5.2.20) [20], implemented in Matlab [26]. The simulation procedure "pepper" was used for numerical simulations. The fitting of simulated spectra to experimental spectra was done via the "esfit" procedure. The fitting process uses the Nelder-Mead method, also called downhill simplex method, based on a heuristic optimisation process mostly applied to non-linear problems. Corresponding to the previous section we will show an exemplary spectrum for a Spin 1/2 particle with an isotropic hyperfine splitting a_{iso}. The resulting spectrum is shown in Figure 2.3b. The experimental conditions "Exp" EasySpin needs for spin center simulations, as well as the parameters for the spin systems are given. To tell EasySpin ranges within which parameter can be varied, distinct variation ranges can be given via "Vary_". The last line code starts the fitting algorithm "esfit", also starting "pepper" simulations of the spin centers given via "Sys_", to fit the "ExperimentalSpectrum", under the experimental conditions given in "Exp".

```
% experimental conditions
Exp.mwFreq=9.432; // in GHz
```

```
Exp.Range = [333, 340]; // in mT
Exp.nPoints=601; // number of datapoints
Exp.Temperature=30; // in K
Exp.Harmonic=1; // gives the first harmonic/EPR signal
Exp.Mode='perpendicular'; // B1 perpendicular to B0
Exp.ModAmp=0.10; // modulation amplitude in mT

% spin 1/2 center parameters
Sys_HFI.S = 1/2; // spin system with S=1/2
Sys_HFI.g=2.0023 // free electron g-factor
Sys_HFI.lwpp = [0,0.1]; // lorentzian linewidth of 0.1 mT
Sys_HFI.Nucs='15N'; // HFI to one 15N nucleus with I=1/2
Sys_HFI.A = [30 30 30]; // isotropic HFI a_iso with 30 MHz

% simulate and plot the system
[EPRfield,EPRsignal]=pepper(Sys_HFI,Exp);
plot(EPRfield,EPRsignal);

% starting the fit algorithm
esfit('pepper',ExperimentalSpectrum,{Sys_HFI},{Vary_HFI},Exp);
```

Summary:

So far, we derived a semi-classical description of the electron's magnetic moment $\vec{\mu} = -g_j \mu_B \frac{\vec{J}}{\hbar}$. In the spin hamiltonian we saw how the spin interacts with its environment, especially mentioning here the Zeeman splitting energy $\Delta E_{Zeeman} = g\mu_B B$. The former equation yields transition frequencies in the microwave regime for free electrons. What, above all, influences the shape of these transitions in the EPR experiment will be discussed in the following.

2.2 The Principles of EPR

If now a spin carrying particle is placed in a static magnetic field B and irradiated by photons of matching energy $E_{ph} = \omega\hbar$ a change of state can be induced according to equation(2.6). For a free spin $\frac{1}{2}$ particle, what is frequently the case for electrons in organic semiconductors the resonance condition for a transition between the parallel and antiparallel state is $\Delta m_S = 1$. This is leading to a transition energy:

$$\Delta E_{Zeeman} = g\mu_B B. \tag{2.8}$$

We then find the frequency of the matching photon to be:

$$\omega = \frac{-\mu_B g B}{\hbar} \tag{2.9}$$

for common electromagnets reaching 0.1 to 1.5 Tesla, this frequency is in the GHz, i.e. microwave (MW) regime.

Multiplicity

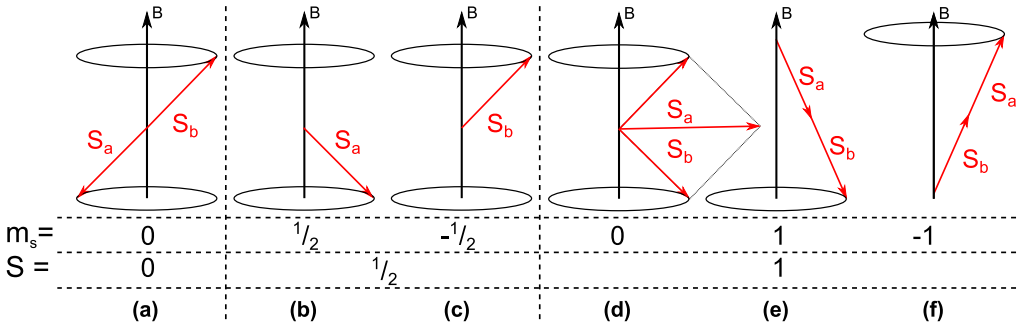

Figure 2.4: Visualisation of the distinct configurations possible for two spins S_a & S_b in an external magnetic field B, with kind permision from [27]. **(a)** $S_a + S_b = 0$ is called singlet, **(b)**&**(c)** $S_a = -S_b = \frac{1}{2}$ are called doublet and represent a spin in antiparallel and parallel alignment to B, respectively. **(d)**, **(e)** & **(f)** $S_a + S_b = 1$ are called triplet.

We have seen that equation 2.6 depends on the angular momentum quantum number $J = S + L$. As the EPR experiment doesn't change the orbital angular momentum quantum number L, we only need to consider the spin quantum number S. Depending on the sum over all involved spins $S = s_a + s_b + \ldots$, there is only a particular number of distinct configurations possible, given by the multiplicity $2 \cdot S + 1$ [12]. If we observe only one Spin (s=1/2) it is called a doublet, because $2 \cdot S + 1 = 2$. For two involved Spins the configuration is called a singlet, if $2 \cdot S + 1 = 1$, and a triplet, if $2 \cdot S + 1 = 3$ (see Figure 2.4). The projection of the spin quantum number S on the external magnetic field B is defined as m_s.

2.2.1 The EPR Signal's Shape and Broadening Mechanisms

At first we will use the Bloch equations to determine the macroscopic behaviour of a sample measured in an EPR experiment. Afterwards we will see what broadens the EPR signal and what an important role the g-factor plays for the signal interpretation.

The Bloch Equations

As mentioned before, magnetic moments can align parallel and antiparallel with respect to the static external magnetic field, again oriented in z-direction B_Z. Since both cases are possible, eliminating each others effect on the overall magnetisation, we need to know their difference. The population rate Δp represents the difference of the probabilities for the parallel and antiparallel state given by Boltzmann [12]:

$$\Delta p = \frac{1 - e^{-\frac{\Delta E}{k_B T}}}{1 + e^{-\frac{\Delta E}{k_B T}}} \tag{2.10}$$

with the Boltzmann constant k_B, the sample temperature T and the energy difference between both states ΔE. In the case of a single electron, we get $\Delta E = -g\mu_B B$. Now we can define the overall magnetisation M_0 for a paramagnetic material with the volume V in our sample as [23, 28, 21]:

$$\vec{M}_0 = \frac{1}{V} \sum_{i=1}^{N_{spins}} \vec{\mu}_i = \Delta p N \vec{\mu} \tag{2.11}$$

with the total amount of spins N_{spins} and the magnetic moment $\vec{\mu} = \frac{g\mu_B}{2}$ oriented in z-direction. If we now apply a second magnetic field in another direction than z, we can change the magnetisation orientation similar to the angular momentum L:

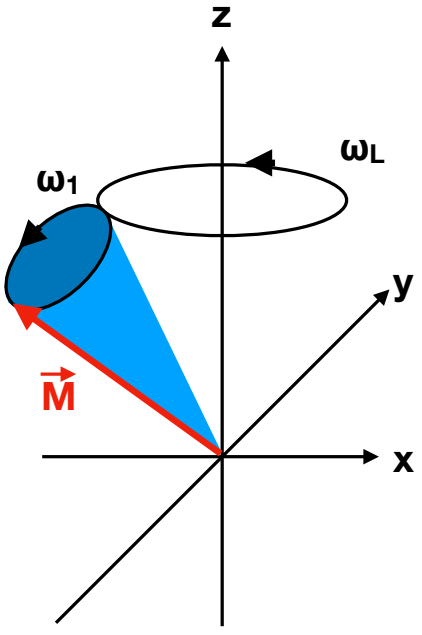

Figure 2.5: Nutation of the magnetization $\vec{M}$ with ω_L and ω_1.

$$\frac{d\vec{M}_0}{dt} = \vec{M}_0 \times \frac{-g\mu_B \vec{B}(t)}{\hbar}. \tag{2.12}$$

In thermal equilibrium the magnetisation $\vec{M}$ aligns with the static magnetic field B_Z. An additional microwave field B_{MW} perpendicular to B_Z then effectively changes the direction of $\vec{M}$. We define the direction of B_{MW} to be the x-axis leading to a precession around this with $\omega_1 = \frac{g_x \mu_B B_{MW}}{\hbar}$. Together with the Larmor precession ω_L around the z-axis, described previously in chapter 2.1.1, they superimpose to a so called nutation motion.

To calculate the magnetisation in all spa-

tial directions let's assume the perpendicular resonant field to be described by $B_{MW}(t) = B_{MW}\cos\omega_{(MW}t)$. To get $B_{MW}(t)$ time independent we change our cartesian plane into a rotating frame with the rotation frequency ω_{MW}. Furthermore, we need to consider relaxation effects diminishing the magnetisation. First we want to mention that spontaneous emission scales with f^3 the cubed frequency [29], and is not of relevancy for spin crossover frequencies below 1 THz [23]. The two relevant processes are spin-flips, an elongated spin flipping back into the direction of the external magnetic field, and spin-flip-flops, two elongated spins exchanging their direction with respect to the external magnetic field. First causes longitudinal relaxation quantified by the T_1 time and later transversal relaxation i.e. coherence decomposition, quantified by the T_2 time. As spin-flip-flops are obviously twice as efficient as spin-flips we can conclude $2T_2 \leq T_1$. We then determine the general Bloch equations for the change of the macroscopic magnetisation:

$$\frac{dM_x}{dt} = -\Omega_{Off}M_y - \frac{M_x}{T_2} \tag{2.13}$$

$$\frac{dM_y}{dt} = \Omega_{Off}M_x - \frac{M_y}{T_2} - \omega_1 M_z \tag{2.14}$$

$$\frac{dM_z}{dt} = -\omega_1 M_y - \frac{M_z - M_0}{T_1} \tag{2.15}$$

with $\Omega_{Off} = \omega_L - \omega_{MW}$ representing the resonance frequency offset.

Relaxation and Other Signal Broadening Mechanisms

Let's take a look on how magnetic moments interact with microwave photons. As our spin flipping microwave field is perpendicular to the external magnetic field aligning the spins in the z-direction we only detect microwave absorption in the x-y plane. Due to a continuous microwave irradiation we can consider a steady state system for microwave absorptions and emissions. In this case the time derivations in the general Bloch equations (2.15) vanish and we can easily solve this ordinary system of equations to get the distinct magnetisation components [23, 28]:

$$M_x = M_0\omega_1 \frac{\Omega_{Off} T_2^2}{1+\Omega_{Off}^2 T_2^2 + \omega_1^2 T_1 T_2} \tag{2.16}$$

$$M_y = -M_0\omega_1 \frac{T_2}{1+\Omega_{Off}^2 T_2^2 + \omega_1^2 T_1 T_2} \tag{2.17}$$

$$M_z = M_0\omega_1 \frac{1+\Omega_{Off}^2 T_2}{1+\Omega_{Off}^2 T_2^2 + \omega_1^2 T_1 T_2} \tag{2.18}$$

These equations can be simplified even more for low microwave intensities with $\omega_1^2 T_1 T_2 << 1$. Because M_x and M_y are then $\propto \omega_1$ this is called the linear regime.

$$M_y(\Omega) = -M_0\omega_1 \frac{T_2}{1+\Omega_{Off}^2 T_2^2} \tag{2.19}$$

In this case, the microwave photon absorption got a Lorentzian lineshape with a linewidth $\propto \frac{1}{T_2}$, often referred to as the natural linewidth. This can also be understood by recalling the energy uncertainty $\Delta E \geq \frac{\hbar}{2\Delta\tau}$ where $\Delta\tau$ can be related to the accuracy or duration of the measurement or the lifetime of the observed state [14, 30]. This time fluctuation $\Delta\tau$ in our case for spins changing their orientation is given by the spin coherence decay time T_2. Other broadening mechanisms present in EPR experiments can be separated into homogeneous and inhomogeneous, leading mainly to Lorentzian and Gaussian lineshapes, respectively [10].
Mechanisms shortening T_2, like saturation dealt with in the following section, lead to homogeneous broadening.
All other mechanisms lead to inhomogeneous broadening. Among them are technical acquisition parameters like integration times or the so called modulation broadening. The magnetic field modulation, shown in the experimental section 4.2 in Figure 4.3, has to be small compared to the natural linewidth otherwise the EPR signal will be drawn-out. A common physical effect are unresolved hyperfine interactions, caused by dipole-dipole interactions of the spin with different nuclei.
In gases and solutions anisotropic interactions are averaged out, but they can still contribute to spin-flips, i.e. longitudinal relaxation. This occurs, if the magnetic field of the anisotropic interaction varies on a timescale similar to the spin-flip crossover frequency. Possible candidates are rotary motions or relative molecule movements [31]. As spin-flip-flops are energy conserving they actually get faster for slower movements. This is a result of the spectral density function, which tells us the frequency of a transition with respect to its' energy [32]. The phenomenological T_2 time introduced in the bloch equations therefore contains the contributions of the spin-flips (T_1) and spin-

flip-flops (T'$_2$). For isotropic field fluctuations, as in liquids, we find $\frac{1}{T_2} = \frac{1}{T_2'} + \frac{1}{2*T_1}$ [33]. In powders, amorphous systems and glasses all orientations are uniformly distributed. In the case of anisotropic interactions we get an inhomogeneous gaussian distribution of the resonance frequency. This case can be identified with a hole burning experiment, where a homogeneously broadened line would simply saturate homogeneously [23]. Generally we get much faster transversal (T_2) than longitudinal (T_1) relaxations in solid state.

Signal Saturation

Let us now consider the case of high microwave intensities $\omega_1^2 T_1 T_2 >> 1$. At the point of resonance $\Omega_{Off} = 0$, M_x vanishes and we get:

$$M_y(\Omega_{Off} = 0) = \frac{M_0}{\omega_1 T_1} \tag{2.20}$$

which decreases for increasing MW power (ω_1). A reason for this is the stimulated flipping of spins and the compensation of the population difference ΔpN. If one needs to find the linear regime to avoid saturation in an EPR experiment, saturation curves have to be measured. Without overlapping signals and other broadening mechanisms it's sufficient to plot the experimentally determined peak to peak signal amplitude vs. the root of the MW power, as $B_1 \propto \sqrt{P_{MW}}$ [10].

The g-Tensor

As we have seen previously in the spin hamiltonian, there are many interactions possible. In an EPR experiment (see chapter 4 for comparison) all of these can lead to a splitting of the simple lorentzian- into a multi peak EPR absorption signal. This multi peak signal may not be mistaken as a splitting of the g-factor (see equation 2.8) into a g-tensor, which might be caused by the charge carriers environment deforming its' isotropic wave distribution. Additionally, the spin and orbital angular momenta couple, which is an relativistic effect as from the point of view of the electron the nucleus moves around it. The SOC increases for atoms with higher atomic number $\propto Z^4$ [12]. SOC for ions with occupied d shells is given by Abragam and Pryce [18]. SOC generally mixes singly occupied molecular orbitals in the excited and ground states, whereat mainly the energetically closest states contribute [22]. Coupling to filled molecular orbitals increases g, while coupling to empty molecular orbitals reduces g. Ways to determine the g matrix are given in detail in [33], and [21]. To avoid confusion we will take a closer look at that g-tensor now, which can always be diagonalised to:

$$\vec{g} = \begin{pmatrix} g_{xx} & 0 & 0 \\ 0 & g_{yy} & 0 \\ 0 & 0 & g_{zz} \end{pmatrix}$$

As you can see in Figure 2.6, a g-tensor for different spin-1/2 systems can have different symmetry characteristics. These are called isotropic $g_{xx} = g_{yy} = g_{zz}$, axial $g_{xx} = g_{yy} \neq g_{zz}$ or rhombic $g_{xx} \neq g_{yy} \neq g_{zz}$. The microwave absorption for the corresponding systems is shown in red. Due to the lock-in detection method, based on the modulation of the magnetic field explained in detail in chapter 4.2, an EPR signal represents the 1st derivative of the microwave absorption shown in blue. The number of intersections with the zero line is the first hint on the amount of investigated spin systems. If one applies this knowledge with respect to the aforementioned signal saturation behaviour it is possible to distinguish the different spin environments even in the case of overlapping signals.

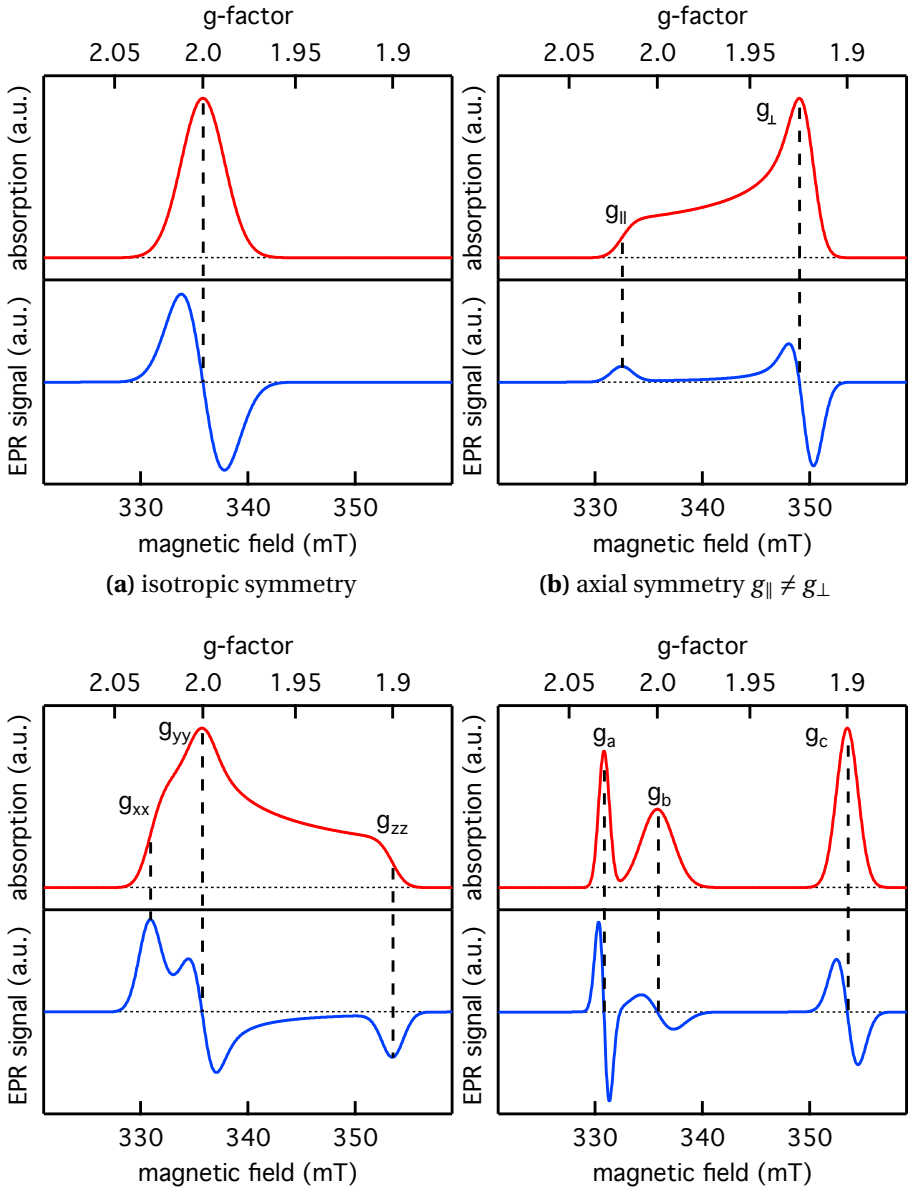

(a) isotropic symmetry

(b) axial symmetry $g_{\parallel} \neq g_{\perp}$

(c) rhombic symmetry $g_{xx} \neq g_{yy} \neq g_{zz}$

(d) independent systems g_a, g_b, g_c

Figure 2.6: Simulated microwave absorption spectra for spin-1/2 systems in red and their 1st derivatives in blue, with kind permission from [27]. Due to lock-in detection the 1st derivative corresponds to the measured EPR signal, explained in chapter 4.2. The g-tensor characteristics are called **(a)** isotropic ($g_{xx} = g_{yy} = g_{zz} = 2.0$), **(b)** axial ($g_{\parallel} \neq g_{\perp}$) and **(c)** rhombic symmetry ($g_{xx} \neq g_{yy} \neq g_{zz}$). **(d)** Three different electron environments leading to distinct and distinguishable g-factors and linewidths.

2.2.2 Quantitative EPR

In this chapter we have already discussed a few effects influencing the EPR lineshapes. Considering these effects as well as all set-up and sample parameters (see section 4.2 for comparison) one can obtain the total number of spins N_{Spins} causing a distinct EPR signal. As the spins absorb microwave photons we find their amount to be directly proportional to the area A under the microwave absorption spectrum. Regarding that the EPR signal represents the absorption's 1st derivative, we need to integrate our EPR spectra twice to obtain A. The ratio N_{Spins}/A is given for this case by [10]:

$$\frac{N_{EPR}}{A} = \frac{V_S T_S D K}{Q_n \eta g^2 S(S+1)\omega_0} \cdot \frac{1}{H_r H_m} \cdot \Sigma \tag{2.21}$$

where Σ represents all sources of noise, like detector-, amplifier- and microwave source noise. D is a multiplicity factor for hyperfine structures, K is a constant, Q_n is the cavity quality factor, η is the sample filling factor (the sample's relative volume inside the EPR cavity), S is the spin quantum number, ω_0 is the cavity resonance frequency, H_r and H_m are the resonance magnetic field and the field modulation, respectively. V_S and T_S are the sample's volume and temperature, respectively. The g-factor squared g^2 in this equation is a result of the sample magnetisation in a magnetic field, described by the Boltzmann distribution and simplified by a Taylor series approximation. g represents an average g-factor calculated by the components of the principal axis of the g tensor $g_{avg} = \frac{g_{xx}+g_{yy}+g_{zz}}{3}$, as discussed in chapter 2.2.1,
As these parameters are difficult to determine they occasionally result in huge error bars and it is reasonable why quantitative spin numbers are usually not discussed in EPR literature. But, there are two approaches to use this on the first glance impracticable equation: First, one could do a full spectrometer characterisation, determining the above mentioned parameters. Here it should be mentioned that some of these parameters are like the human mood, changing from day to day. Second, one could compare their sample to a reference sample with a known number of spins and a similar size and paramagnetic behaviour. In the second case, the two samples should be measured right after each other, keeping all set-up parameters unchanged [34, 35]. If this is done carefully, equation 2.21 can be simplified to

$$\frac{N_U}{N_R} = \frac{A_U}{A_R} \cdot \frac{D_U}{D_R} \cdot \left(\frac{g_R}{g_U}\right)^2 \cdot \frac{S_R(S_R+1)}{S_U(S_U+1)} \tag{2.22}$$

where indices $_U$ and $_R$ represent the unknown- and reference sample, respectively. In this work, we will mainly deal with Spin 1/2 particles displaying negligible hyperfine splittings. Therefore we simplify further to get

$$N_U = \frac{A_U}{A_R} \cdot \left(\frac{g_R}{g_U}\right)^2 \cdot N_R. \tag{2.23}$$

This equation will give us the amount of spins responsible for an EPR signal, if we know the corresponding g-factors and spectra areas A.

Summary:

At first we derived the Zeeman splitting energy of the spins $\Delta E_{Zeeman} = g\mu_B B$ from the electron's magnetic moment. Together with the population difference Δp for parallel and antiparallel spin configurations, given by the Boltzmann distribution, transitions can be induced via microwave absorption. Various effects in the spin hamiltonian altering this transition's signal shape in the EPR experiment have been briefly discussed. Also the change and saturation behaviour of the total net magnetisation has been shown by means of the Bloch equations. We have seen that different electron environments lead to distinct g-factors and linewidths, shown in Figure 2.6. Finally, we determined how to quantify the number of probed spins with a reference sample while considering the relevant spectroscopic- and spectrometer parameters.

3 Organic Semiconducting Materials

In this chapter we will focus on organic semiconductors [36], investigating the processes and interactions causing the unique C-atom to form layers, chains and tubes, i.e. graphene, polymers and nanotubes, respectively. We will use that knowledge to learn more about their electrical properties ranging from insulating, to semiconducting, to metallic like. A detailed theoretical description for the macroscale formation of carbon structures like graphene, fullerenes and nanotubes is given in [37, 38]. The basis of all organic chemistry is the hybridisation of orbitals. Due to this phenomenon, reorientation of orbitals various atoms can bond to form new structures with incredible new properties unlike what would be expected from the atoms alone. Carbon, the main building block in organic semiconductors, can hybridise into various configurations by combining 2s- and 2p-orbitals as shown in Figure 3.1. They form new bonding orbitals and transition from atomic orbitals (AO) to molecular orbitals (MO) [39, 40].

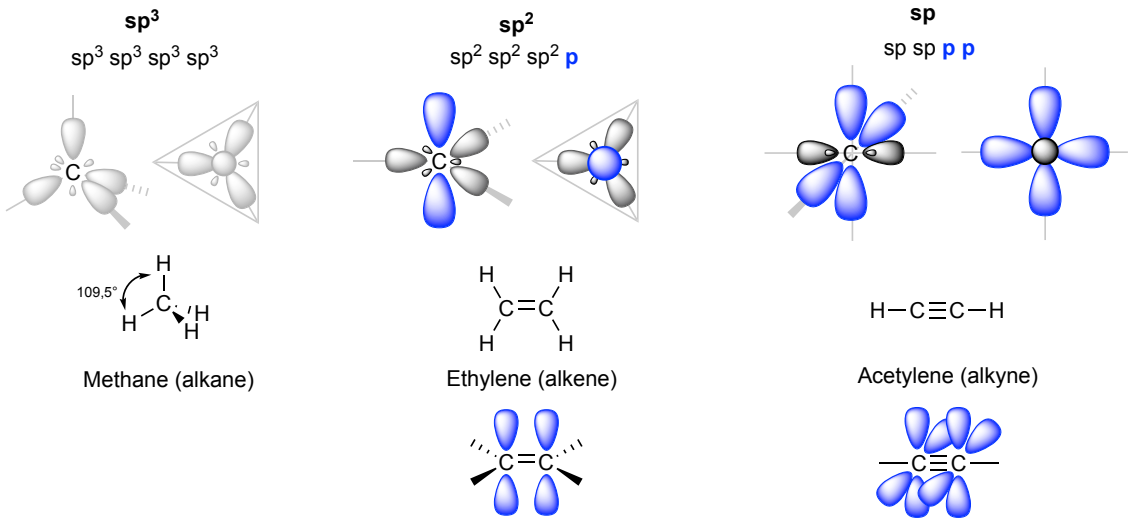

Figure 3.1: Schematic representation of hybridised carbon in sp^3-, sp^2- and sp-configuration. The main contribution to the conductivity in organic semiconductors is carried by the π orbitals marked in blue. Made with [41].

In its ground state the carbon orbitals are occupied as $1s^2\ 2s^2\ 2p^2$, as shown in Figure 3.2a. If, as shown here, another carbon atom perturbs the system we can imagine the 2s and 2p energy splitting to be compensated. In this case we need to construct the new MOs by linear combinations of the old AOs, a process called hybridisation. Due to this ability to form combined orbitals, the $2s^2\ 2p^2$ orbitals can hybridise in order to bond with other atoms. Depending on the binding partners they hybridise in sp^3-, sp^2- or sp-configuration. An example for sp^3 hybridisation (alkane) is the tetrahedrally shaped Methane molecule (CH_4), resulting in four double occupied σ-MOs spread by 109,5°. Two Methane molecules can then bind to form Ethene (C_2H_6) with a single bonding σ-MO. A double bonding in plane molecule (σ and π-MO) is possible due to sp^2 hybridisation (alkene) as in Ethylene (C_2H_4). As a result of sp hybridisation (alkyne) triple bonds (σ and two π-MOs) as in Acetylene (C_2H_2) are also possible.

3.1 Polymers

A great overview over what has and might be done with conjugated polymers was recently given by Swager [42].

Conjugated systems, as shown in Figure 3.2a, are bond by in plane σ-bonds due to sp^2 hybridisation and perpendicular out of plane π-bonds (p orbitals). In the π system the electrons can move freely. These chains can also form cyclic rings like Benzol (C_6H_6). Bonding Benzol rings can result in graphene layers. The orbital's corresponding energies are depicted right in Figure 3.2a and change from single C-atoms to C_2H_4 to chains and rings. Adding more and more carbon to systems with a delocalisation of p-orbitals, i.e. conjugated π-systems, causes the formation of a highest occupied molecular orbital (HOMO) and a lowest unoccupied molecular orbital (LUMO) from the π & π^* orbitals, respectively. They also mainly contribute to the conductivity of organic semiconductors, unlike the strongly localised σ-bonds. As π-bonds are weaker than σ bonds, the lowest excitation occurs between π and $\pi*$ with around 1.5eV to 3eV [36]. Note, that the depiction of single and double bonds in conjugated systems is merely for illustration purposes. The π electrons are delocalised and all carbons in the system are equivalent.

Nevertheless, the unperturbed HOMO and LUMO calculations from simple π Hückel theory or linear combinations of atomic orbitals (LCAO) may not reproduce reality. There, various aggregations like H- and J-aggregates, chain conformation or length might have a significant influence on the energetic landscape. For poly(3-hexylthiphene) (P3HT) this has been shown theoretically and experimentally by Böckmann et al. [43], for the conformation transfer from solution to crystal phase.

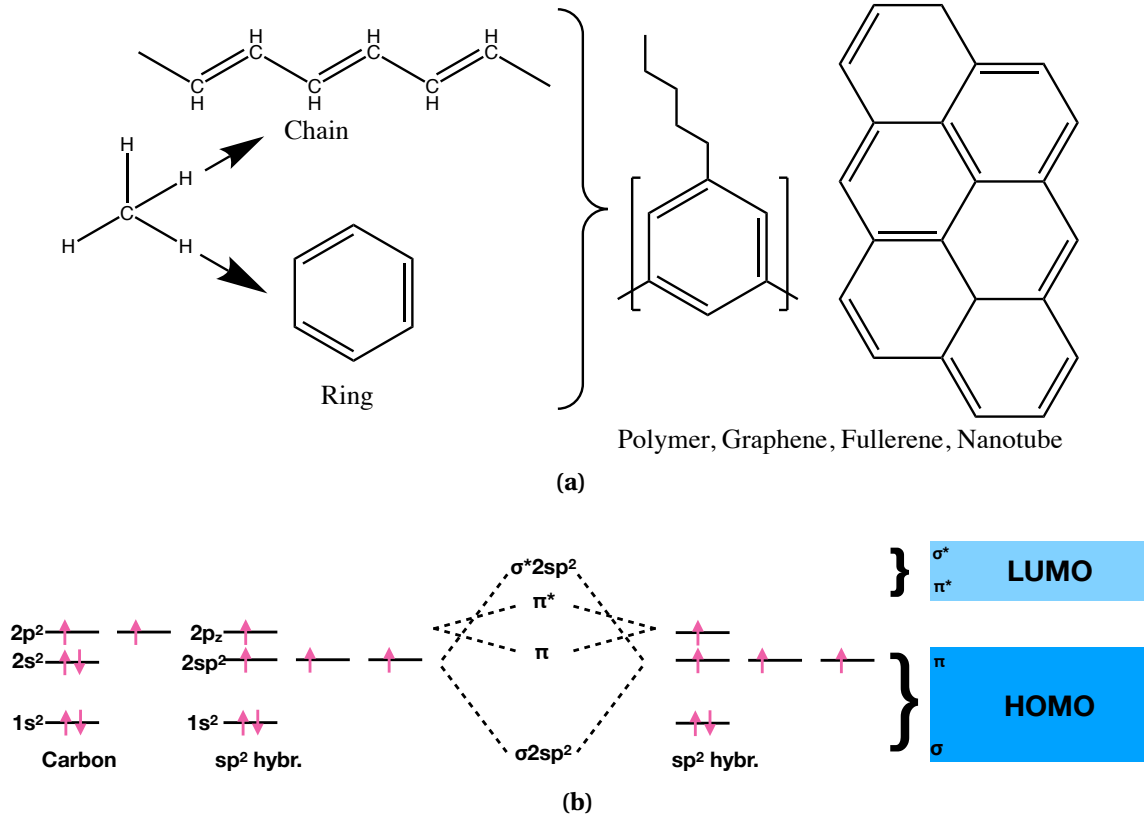

Figure 3.2: Scheme of a) Carbon hybridisation leading to the formation of chains, rings, and finally forming polymers, graphene, fullerenes and nanotubes b) Bonding hybridized carbon orbitals leading to the formation of HOMOS and LUMOs, due to the delocalised π-MOs.

3.2 Fullerenes

Fullerenes look like a football, as exemplarily depicted in Figure 3.3 for C_{60}, i.e. a carbon ball made of 60 C-atoms. They are also assigned to the group of carbon clusters. The fullerenes earned their name due to their architectural similarity to structures from the canadian architect Buckminster Fuller [12]. To calculate fullerene energy levels highly difficult numerical calculations need to be performed based on density functional theory (DFT). A comprehensive guide to DFT was written by Koch and Hohlhausen [44]. Due to the uncertainties and different simplifications used for the various basis sets in DFT, errors are difficult to determine. As we will see in chapter 5, very often there are too many interactions possible to find the correct numbers only by a theoretical approach. Nevertheless, theoretical calculations are

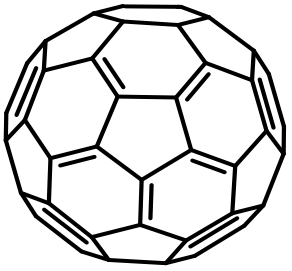

Figure 3.3: Visualisation of the C_{60} fullerene.

highly necessary to discover possible interesting states and properties. For example Shubina et al. predicted the possibility of electrons delocalising over a fullerene dimer [45], which we were able to detect. Furthermore, fullerenes are used as electron acceptors together with the previously discussed polymers which act as donors in organic solar cells. There also another class of carbon structures is used, the carbon nanotubes discussed in the next section.

3.3 Single-Wall Carbon Nanotubes (SWNT)

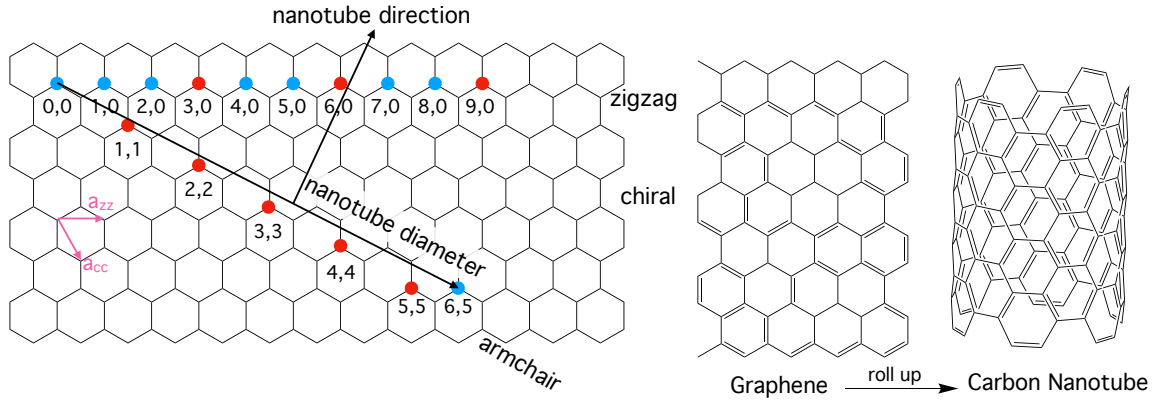

Figure 3.4: Red represents metallic, **blue** semiconducting carbon nanotubes. Orientation of the unit vectors $\vec{a}_{CC}$ and $\vec{a}_{ZZ}$ is shown in **pink**. The (n,m) configurations are given in the Graphene layer categorised as "zig-zag", "armchair" und "chiral", adapted from [46]. We also did add black arrows indicating the (6,5)-carbon nanotube diameter and tube direction. Rolling up the graphene layer yields the according type of carbon nanotube.

In graphene solely the carbon atoms form three double σ in plane bonds to adjacent carbon atoms yielding a hexagonal, alveolar structure. As mentioned earlier, the current is mediated only by the π electrons whose structure can be predicted by Hückel theory. As a visualisation for carbon nanotubes we think of a rolled-up, one atom thick layer of carbon atoms, i.e. graphene as indicated in Figure 3.4b. A more detailed description on the formation mechanisms of carbon nanotubes can be found in [38], where they use molecular simulations to visualise the nucleation and growth process on different catalysts yielding carbon nanotubes with various chiralities . One way to produce carbon nanotubes is the not very efficient but easy to implement electric arc technique. There, we generate electric arcs between carbon electrodes under helium atmosphere [47]. Another possibility is laser ablation of carbon targets generating high yields of single-wall carbon nanotubes (SWNTs) [48].

All carbon nanotubes are classified by one property alone, called chirality [49]. Let's take a step back and think again of a Graphene layer. The chirality is given in the form (n,m), separated into three sub categories called: $(n,0)$ "zig-zag", (n,n) "armchair" and all other cases "chiral" as indicated in Figure 3.4a. These names result from the structure of the nanotube endings. If the fraction $\frac{n-m}{3}$ yields a straight number the corresponding chirality represents a metallic (red dot) otherwise semiconducting (blue dot) carbon nanotube, "armchair" tubes are always metallic.
Furthermore, the values of (n,m) correspond to the number of unit vectors (shown in magenta) in the graphene layer needed to follow the C-C bonds around the whole tube diameter arriving at the joint. The unit vectors are $\vec{a}_{CC}$ and $\vec{a}_{ZZ}$, the later one being parallel to the "zig-zag" direction. A "joint vector" is then given by $\vec{C} = n \cdot \vec{a}_{ZZ} + m \cdot \vec{a}_{CC}$. Therefore, the nanotube diameter (d) can be simply calculated based on the chirality (n,m), i.e. it's base vectors, via $d = \frac{a}{\pi}\sqrt{(n+m)^2 - nm} \cdot 10^{-3}$nm [46]. The distance between two hexagons is $a = 0.246$ nm [50], being also the length of the uni vectors $\vec{a}_{CC}$ and $\vec{a}_{ZZ}$.

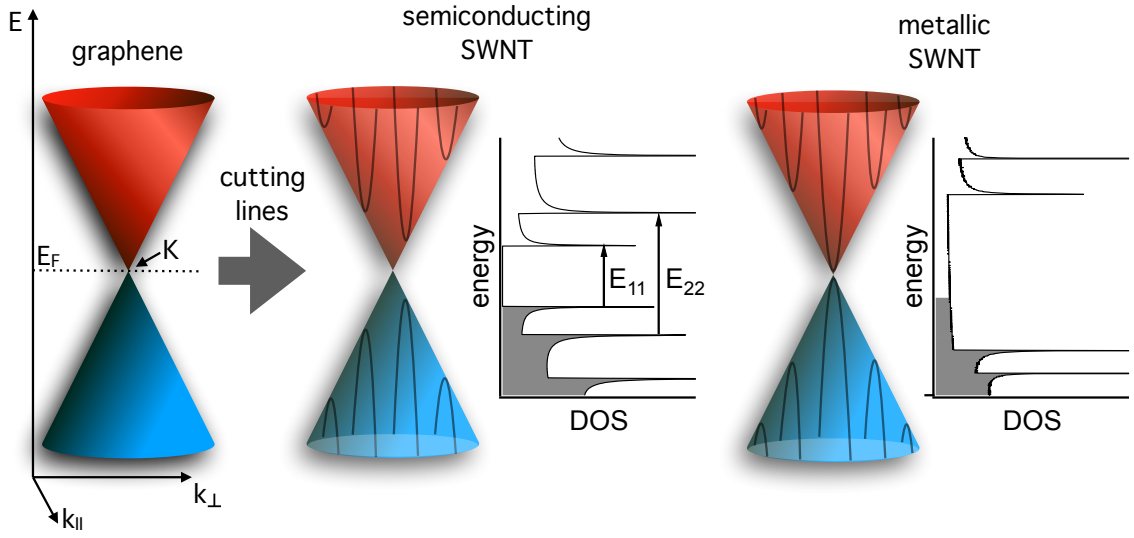

Figure 3.5: Schematic representation of the 2D graphene energy bands and the cutting lines approach for 1D semiconducting and metallic nanotubes. The corresponding density of states (DOS) for a semiconducting (6,5) and metallic (6,0) tube are shown on the right, respectively.

Let us now focus on the electrical properties of carbon nanotubes. Here, especially metallic tubes exhibit extraordinary electrical conductivity, called ballistic charge transport. Also for Graphene layers ballistic charge transport, i.e. Quantum Spin Hall Effect has been reported [51]. In this case almost no scattering processes occur and the electrical resistance nearly vanishes. A condition for ballistic charge transport is a mean

free path higher than the length of the medium on which the charges reside. The mean free path is defined as the distance an electron can travel without scattering [52]. Even if it is not ballistic charge transport by definition, the mean free path in carbon nanotubes can be extraordinary long. Nevertheless, semiconducting nanotubes can exhibit extraordinary electrical conductivity too [53]. Especially in networks, their extreme electrical conductivity makes them interesting for optoelectronic applications [54].

Calculating the SWNTs energy levels is somewhat different than for the previous cases of polymers and fullerenes, as we are using an indirect approach starting from graphene. Therefore, to determine the electronic and phonon dispersion of the near infrared absorption of SWNTs we refer to the concept of cutting lines from Saito and Dresselhaus [49], helpfully reprocessed in a review by Samsonidze et al. [55]. Please note, that the cutting lines approach only works for nanotubes with a diameter > 0.6 nm. Smaller diameters exhibit a curvature that induces mixing of σ and π bands, which is not included in the calculations for the graphene bands. A similar, but on space group theory based approach on nanotube electronic and phononic symmetry is given in [56], yielding the same results. At first we will need to determine the 2D graphene energy bands in reciprocal space by using a for example π-band nearest neighbour tight-binding model, schematically shown as dirac cones in Figure 3.5. According to the (n,m) nanotube's base vectors given in the previous section, we project equidistant lines into the graphene's conduction and valence bands in reciprocal space. The amount of lines is given by the size of the nanotubes unit cell in real space. The line length and spacing is given by the vectors spanning the unit cell in direction of the tube length or diameter, respectively. These lines do then correspond to the nanotube's 1D energy bands. If the cutting lines cross the K point, the edge of two lines in the first brillouin zone, the nanotube doesn't have a band gap and is therefore metallic, otherwise semiconducting. Both cases are shown on the right and left of Figure 3.5, respectively. According to the DOS equation for the effective mass m_{eff} approximation in 1 dimension

$$g_{1D}(E) = \frac{\sqrt{2}}{\pi}\left(\frac{\sqrt{m_{eff}}}{\hbar}\right)(E - E_C)^{-\frac{1}{2}}$$

with E_C the conduction band edge energy, we determine the distributions for valence and conduction bands as shown to the right of every dirac cone in Figure 3.5. The sharp peaks are cases of very strong resonance of the system and referred to as the van Hove singularities.

4 Experiment

As we are now familiar with the physical processes involved in EPR measurements, we will take a look on sample preparation and shift our focus to the technical aspects of signal detection in our experimental setup.

4.1 Sample Preparation

Organic materials are in general quite sensitive to oxygen contamination driving chemical reactions. Therefore, reducing oxygen concentration is crucial. If not done carefully chemical reactions i.e. sample degradation might occur, especially if the samples are illuminated. If possible, all preparation steps are performed inside a glove box with an oxygen free nitrogen atmosphere.

4.1.1 Solar Cells

A detailed description about organic solar cell preparation is given in a book by Brabec et al. [1], including common device layouts. Highly efficient but elaborate tandem solar cells are discussed in [57].

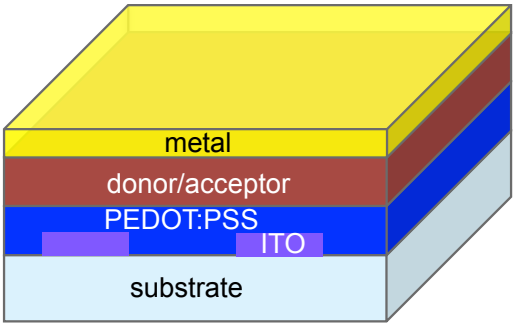

Figure 4.1: Scheme of a possible device architecture. Our cell structure is as follows substrate/ITO/PEDOT:PSS/Active Layer(s)/Metal.

The layers of an organic solar cell are generally deposed onto sapphire glas coated with transparent indium tin oxide (ITO), used as anode. One possibility to apply the active layer is evaporation inside an evaporation chamber via thermal vaporisation of the materials in resistive heated crucibles. Another option is drop casting of the materials in solution. Depending on the sample, the cells were grown layer by layer, or two materials at the same time resulting in material intermixture. For the active material, intermixture yields an efficient separation of excitons

as the interface is now distributed throughout the whole bulk. With these two techniques single-, bi-, trilayer and bulk heterojunction cells were produced. The layer thicknesses vary from a few to a few hundred nm. Such low thicknesses are possible due to the direct absorption of organic semiconductors yielding very high absorption coefficients, orders of magnitude higher than for indirect absorption processes in inorganic semiconductors. For EPR experiments a reduced device architecture without anode and cathode was used, as extraction of the charge carriers is not necessary. Therefore, we limit ourselves to a substrate/donor/acceptor structure. As substrates we utilise thin polyethylene foil, as it can easily be cut and stacked to increase the material amount in the space limited EPR cuvettes of the spectrometer resulting in a stronger signal.

4.1.2 EPR samples

Thin Film Samples

Film samples were prepared under nitrogen atmosphere inside a glovebox. The compounds were dissolved and diluted in their respective solvent(s) separately. Afterwards, they were mixed and often shaken to speed up intermixture before poured into an EPR tube. To minimise air contact EPR tubes are closed with plastic caps inside the glovebox before taken out. After removing the plastic cap outside the glovebox the tube is immediately connected to a vacuum pump, five times flushed with helium and then sealed off with a blow torch between (0.2 to 20) mbar helium atmosphere.

Solution Samples

Samples in solution are poured into an EPR tube using a thin polyethylene tube attached to a pipette. This is preferable over simply letting the solution run down the inner sidewalls of the EPR tube. Thereby, adhesion of the solution on the sidewalls causing material loss and uncertainty can be avoided. Finally, the EPR tube is carefully flushed with Helium and connected to a sealed Helium balloon with overpressure, as shown in Figure 4.4. This overpressure prevents air from entering the system due to minor leakage.

Spin References

For samples, used for quantitative spin measurements, special preparations need to be made. Some sample preparations including dilution processes were done in a nitrogen glovebox, as we are dealing with organic radicals which are very sensitive to oxygen.

At first, a little bit cotton wadding was put into the EPR tubes before pouring 100μL solution into it. The EPR tubes are evacuated, while flushing over five times with helium, and sealed off under around 10-20 mBar helium atmosphere. Vacuum pumping removes the solvent and the powder is spread over the fabric. Due to this cotton wadding, crystallizing molecules will orient themselves spatially randomly. This results in an evenly distributed g-tensor necessary for the spin number calculations (see chapter 2.2.2). Furthermore, the cotton wadding will keep the liquid sample down in the tube during the whole process. Figure 4.2 shows a spin reference sample, containing 47 μg $CuSO_4$. Due to these small amounts, the materials themselves are generally not visible by eye. In the picture one can merely see the white cotton wadding.

Figure 4.2: Spin reference sample containing $CuSO_4$. Due to the small amounts of material one can merely see the white cotton wadding.

4.2 The EPR Spectrometer

4.2.1 Detection Method

The electron paramagnetic resonance (EPR) experiment is based on the Zeeman effect. The energetic splitting of a spin carrying particle inside an external magnetic field is directly proportional to the magnetic field strength. If the energy of an incident photon $E = h\nu_{MW}$ matches the energy splitting according to equation (2.6), the electron's spin resonance condition $\Delta m_J = \Delta m_S = 1$ is fulfilled and we get:

$$\Delta E_{Zeeman} = g_J \mu_B B = h\nu_{MW} \tag{4.1}$$

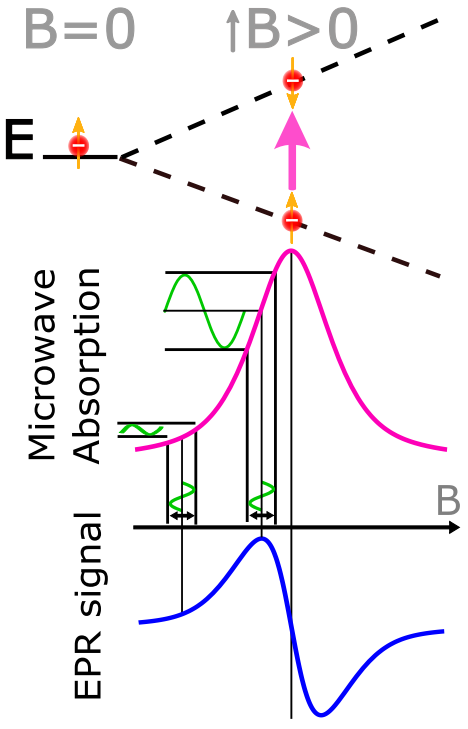

Figure 4.3: Electron(**red**), i.e. spin 1/2 particle, Zeeman splitting. Microwave absorption(**pink**) is shown as well as the magnetic field modulation(**green**) producing the EPR signal(**blue**), adapted from [27].

There are two possibilities to put EPR measurements into practise. First, one can keep the magnetic field constant and vary the radiation frequency, or second, keep the radiation frequency constant and sweep the magnetic field. As the implementation is more feasible for the second case we detect the EPR signal intensity while sweeping the magnetic field. Additionally, an alternating field (green) is superimposed with the stepwise sweeping magnetic field inducing an microwave absorption modulation as depicted in figure 4.3. This allows for an implementation of lock in detection techniques which yield tremendously higher sensitivities. For this reason the measured EPR signal (blue) is the first derivative of the microwave absorption (pink). How this is done experimentally will be shown in the following chapter.

4.2.2 Setup

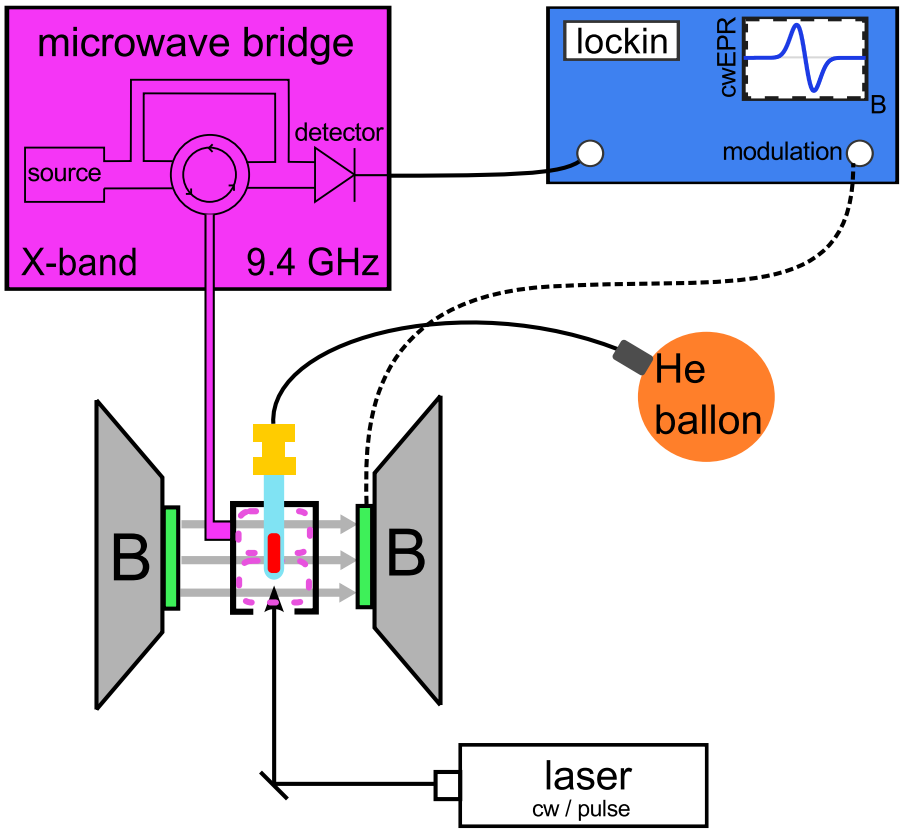

Figure 4.4: X-Band EPR set up scheme, starting from the upper left, we have the reflex klystron and microwave bridge (magenta), lock-in amplifiere (blue), magnetic field coils (grey), sample (red) connected to a He ballon (orange) inside the resonance cavity (black) and laser illumination, adapted from [27].

Our set-up is a home made construction especially designed for X-Band EPR experiments, shown in figure 4.4. We will start our description from the inside out. Firstly, the sample (red) is prepared and put into an EPR tube (turquoise), made of high-purity quartz glass. In the cases where we needed direct access to the samples the tubes weren't sealed but rather connect to a compensation ballon filled with helium (orange). The tube in turn is bathed in a helium flow cryostat and placed inside a TE102 resonance cavity Bruker Modell ER4104OR (black) with a resonance frequency around 9.432 GHz. The temperature can be controlled between 3.6 K to 300 K, by a LakeShore temperature controller Modell 335. Furthermore, the cavity is flushed by dry air to avoid water condensation and crystallisation, an important detail improving temperature stability, regulation and most prominently a change of the cavity's resonance frequency. The Bruker ESP300 spectrometer contains a magnetic field controller Bruker Modell ER032M which operates the magnets (grey), providing homogeneous magnetic

fields between 0.01 to 1.3 Tesla. A 100 kHz sinus field is superimposed to the main magnetic field (green), adjusted by an arbitrary waveform generator Keithley LXI 3390. For CW EPR the reflex klystron inside the microwave bridge Bruker Modell ER041MR (magenta) provides radiation in the microwave frequency regime up to 200 mW. For time resolved EPR (trEPR) we us a faster, but not as sensitive microwave bridge Bruker Modell ER047MRP. The frequency is detected by a frequency counter Marconi Instruments Modell EIP 28B. The microwave bridge guides a part of the radiation back and forth the cavity and another part into the reference arm. After destructive interference of the reference wave with the returned wave the remaining microwave intensity is detected by a lock-in amplifier AMETEK Modell Signal Recovery 7230 DSP (blue).
The main control unit is a computer running labview (not depicted). This magnetic field modulation produces the absorption modulation (green) shown in figure 4.3. All in all we detect the absorption change versus the magnetic field change, i.e. the first derivative of the microwave absorption signal.
To obtain g-factors in high precision, the magnetic field is detected with a high precision nuclear magnetic resonance (NMR) magnetometer Bruker Modell ER035M. Further information about this spectrometer can be found in [58].

5 Charge Transfer in Organic Photovoltaics (OPV)

In this chapter, we will at first recall the basic processes in organic photovoltaics (OPV). Afterwards, we will present the materials used in this work. A basic j-V characterisation of the devices built with the aforementioned materials will be given. There, we did vary the materials stoichiometry resulting in a voltage sweep. The underlying mechanism for the change of the device voltage will be investigated by EPR, to reveal if it is caused by the energetic landscape on the molecular level. A theoretically predicted and for the first time experimentally observed fullerene-fullerene excited state after charge transfer (CT) will be discussed in the end. The voltage sweep as well as the fullerene-fullerene excited state indicate the reorganisation of molecular orbitals in nearby fullerenes after excitation.

5.1 OPV Theory

Polyacetylen, the first conductive conjugated polymer was already discovered in 1977 by Heeger , MacDiarmid and Shirakawa [59], which received the corresponding chemistry Noble prize in 2000. Besides, before 2000 no notable organic solar cell efficiencies were reported (cells in 1986 had about 1% power conversion efficiency [60]). By that we can see when organic semiconductors attracted wide notice and that we are looking at a fairly young and still developing field of research.

5.1.1 Physical Processes

The underlying mechanisms enabeling the conversion of solar energy into electrical energy in organic solar cells is depicted step by step in Figure 5.1. The first necessary step is to deposit a sufficient amount of energy in the system, facilitated by the materials abilities to absorb radiation. In OPV this radiation is mediated by solar photons with wavelengths somewhere in the visible region. Due to the direct absorption of photons in organic semiconductors absorption coefficients are generally very high ($\approx \frac{10^{-7}}{m}$),

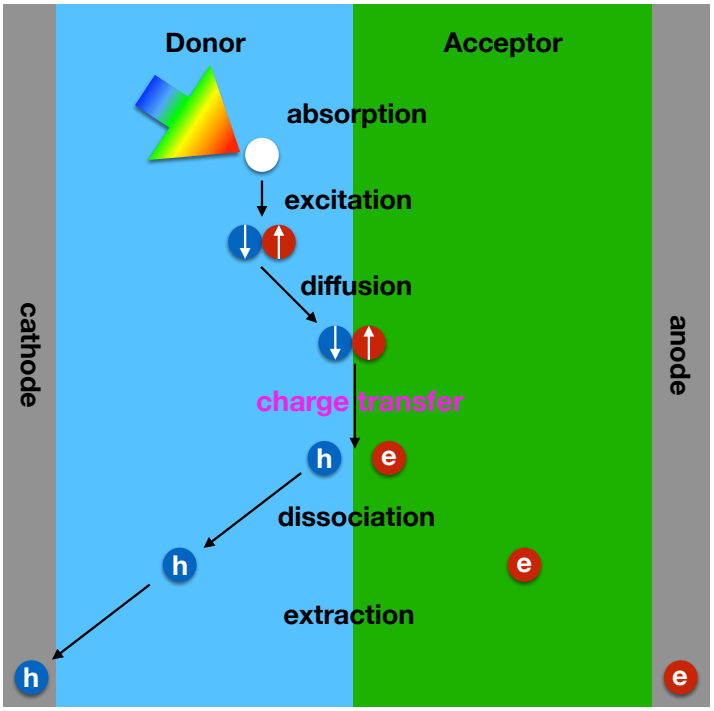

Figure 5.1: Scheme for photocurrent generation in an organic solar cell from absorption till extraction, indicated with black arrows. White arrows represent the singlet exciton spin configuration. Charge transfer marks the point where the exciton dissociates into two spin $S = 1/2$ particles, electron (e) and hole (h), which can be detected via EPR.

orders of magnitude above indirect absorption in inorganic semiconductors. The following excitation of the material generates a strongly bound electron hole pair, often just localised over one molecule, called frenkel exciton [61]. The high binding energy (0.1 to 1 eV) is caused by weak screening due to the materials low dielectric constant ($\epsilon \approx 2-4$). Within it's lifetime of piko- to nanoseconds the exciton can diffuse to a donor acceptor interface, if it is within the exciton diffusion length of a few nanometer. There the strongly bound exciton is separated and charge transfer occurs resulting in an electron-hole polaron pair. After the charge carrier dissociation we have separated electrons and holes with a spin $S = 1/2$ detectable via EPR. The following transport of the polarons and the extraction at the electrodes results in a photocurrent. The open circuit voltage V_{OC} of the system depends on the recombination parameters and the illumination intensity [62], the later will be kept constant in the following measurements. Furthermore, it scales linearly with the energetic separation between the donor's highest occupied molecular orbital (HOMO) and acceptor's lowest unoccupied molecular orbital (LUMO) known as the CT energy E_{CT},

$$V_{OC} \propto \frac{E_{CT}}{q} = \frac{HOMO_{Donor} - LUMO_{Acceptor}}{q} \tag{5.1}$$

where q is the elementary charge.

5.1.2 j-V Characteristics and Photovoltaic Performance

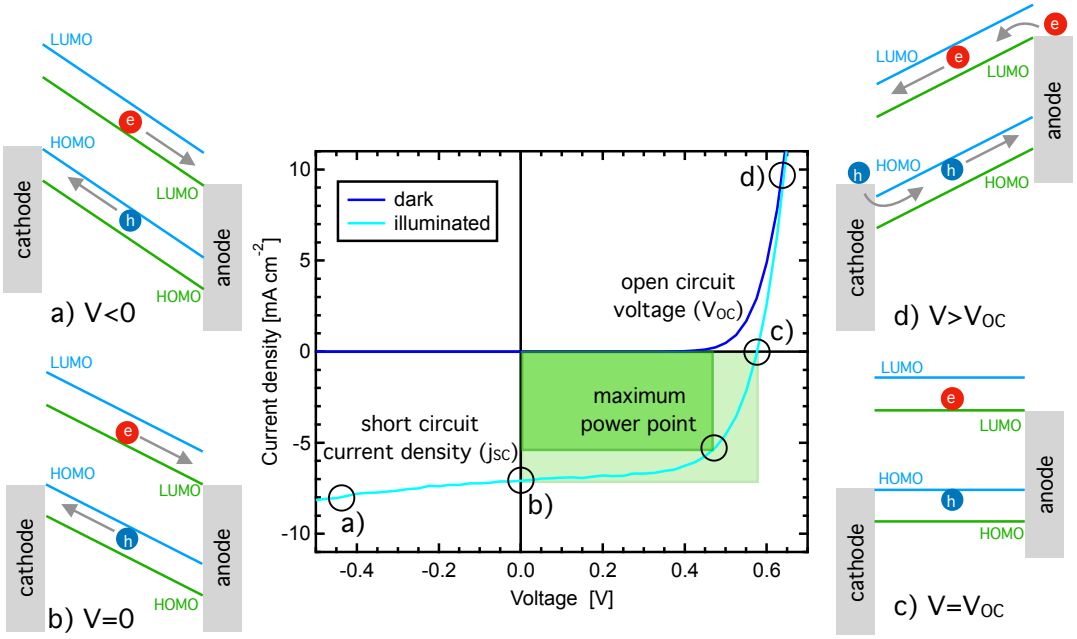

Figure 5.2: Middle: Organic solar cell (P3HT:$PC_{60}BM$) j-V curves in the dark (dark blue) and illuminated (bright blue). Donor (blue) and acceptor (green) HOMO and LUMO levels are schematically shown for different external voltages. The maximum power point (MPP) is also shown. The conversion efficiency (η) is given as the ratio between illumination- and electrical power $\eta = \frac{P_{MPP}}{P_{illum}}$.The filling factor (FF) corresponds to the bright- divided by the dark green rectangle, i.e. $FF = \frac{P_{MPP}}{j_{SC} \cdot V_{OC}}$. Figure adapted from [63].

To evaluate the performance of any type of solar cell we need to measure the current voltage characteristics. For that, we apply an external voltage, measure the corresponding current and normalise it to the active area of the solar cell. This is done with- (illuminated) and without illumination (dark), as shown exemplary in the central Figure in scheme 5.2. Without illumination we simply observe a typical diode curve. With illumination on the other hand, we determine the behaviour of our active cell. If we apply a negative voltage, V<0 see point a), we apply an external electric field efficiently extracting the photogenerated charge carriers. If no external voltage is applied, V=0 see point b), we can determine the short circuit current density j_{SC}. For a positive external voltage we observe a decreasing current out of the device. At the point of zero

current we can determine the open circuit voltage, V=V_{OC} see point c). There, the internal field of the cell is compensated and all photogenerated charge carriers recombine. If we increase the voltage further, V>V_{OC} see point d), we reverse the internal field of the cell and inject charge carriers into the system. To reach the highest efficiency we need to operate our cell at its maximum power output. It is determined by the turning point of the power density j(V)·V, i.e. the maximum power point (MPP) indicated by the dark green rectangle. If we divide it by the bright green rectangle, a product of the j_{SC} and V_{OC}, we determine the fill factor (FF) indicating the squareness of the j-V curve. If we know the irradiation power due to the illumination (P_{illum}), the power conversion efficiency (η) is simply given by

$$\eta = \frac{P_{mpp}}{P_{illum}} = \frac{V_{mpp} j_{mpp}}{P_{illum}} = \frac{j_{SC} V_{OC} FF}{P_{illum}} \tag{5.2}$$

As external conditions influence the various parameters in this equation, a standard measurement procedure is applied, which is defined by a device temperature of 25°C, an irradiance of 100 $\frac{mW}{cm^2}$ and an AM1.5G reference spectrum. The air mass (AM) takes the irradiation angle of the solar light at cos(1/15)=48° for mid-latitudes into account. The global (G) considers the direct and diffuse solar irradiation averaged over one year.

5.2 Charge Transfer Processes in OPV

Generally, organic semiconductors consist of a conjugated π-system of carbon as described in detail in chapter 3. Here, we will build devices with fullerenes as acceptors and a polymer and small molecule as donor, presented in the next chapter. Recently, fullerene-free OPV devices did reach power conversion efficiencies above 14 % for single junctions and 17% for tandem cells [64, 65]. Theoretical calculations even suggest an upper limit of 20-24 % for single junctions [66]. Most of the older well-performing devices used $C_{70}{}^{-}$ instead of $C_{60}{}^{-}$fullerene derivatives, due to their higher optical absorption coefficients [67]. This results in a generally higher photocurrent. If one investigates the absorbance of the different fullerenes, their HOMOs and LUMOs should also be determined as the device voltage strongly depends on them (see equation 5.4). For the voltage, the electron donor HOMO and the electron acceptor LUMO are relevant. By comparing the molecular orbitals, shown in Figure 5.6, an interesting difference in the fullerene acceptors' LUMO levels can be seen indicating different V_{OC} values. Here, the question of charge transfer in solar cells with fullerene mixtures immediately arises. We wanted to know which fullerene would dominate the CT process, as the most occupied fullerene would also dictate the cells' voltage. More generally, we

were interested to see if the pure material's energy levels are preserved in mixtures and if we can still treat them as separate. This question motivated us to build various cells with one electron donor material and a varying stoichiometry between two fullerene electron acceptors. There, we indeed observed a gradual change of the V_{OC} in the working device. Recent papers by Schwarze et al. [68], Felekidis et al. [69], Mollinger et al. [70], Sweetnam et al. [71], and Poelking et al. [72] reported similar tuning effects of the ionization energies, bandgaps and V_{OC} of organic semiconductors by blending them in various ratios. These are even more reasons to focus especially on mixing various fullerene derivatives and elucidate the effect on the molecular energy levels, as these are decisively influencing the voltage of the whole OPV device.
As mentioned previously, quantitative EPR is perfectly suitable to determine and quantify the spacial localisation of charge carriers and thereby their distribution. Furthermore, low temperature EPR seems to be perfectly suitable to represent reality as the low energy (thermalized) CT states are the main precursors to free charges [73].

5.2.1 Materials and Energy Levels

Electron Donors

For simplicity the chemically correct name *Poly*(3 – *hexylthiophene* – 2,5 – *diyl*) will be referred to as P3HT in the following. It is a dark brown powder, absorbing at $\lambda_{Abs} = 442\ nm$ and emitting at $\lambda_{PL} = 564\ nm$ in Tetrahydrofuran(THF) solution [74]. The HOMO and LUMO are at -5 eV and -3 eV respectively [75]. It is a hole transporting polymer.

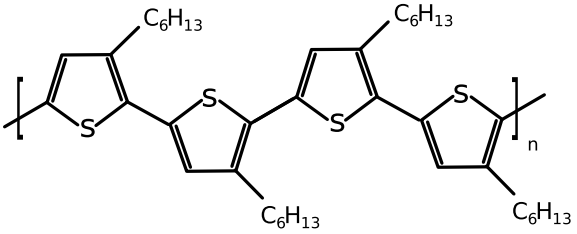

Figure 5.3: Structure of P3HT *Poly*(3 – *hexylthiophene* – 2,5 – *diyl*), in short P3HT

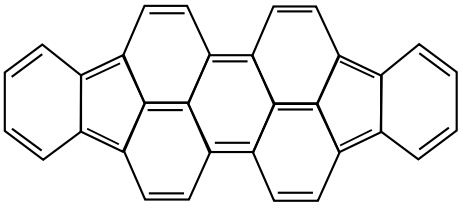

Figure 5.4: Chemical structure of [*Diindeno*(1,2,3,–*cd*,18,28,38 – *lm*)*perylen*], short DIP, revealing it's plane shape.

For simplicity the chemically correct name [*Diindeno*(1,2,3 – *cd*,18,28,38 – *lm*)*perylen*] will be referred to as DIP in the following. It is a planar molecule, 18.4 Å long and 7 Å wide [76]. The HOMO- and LUMO-levels are at −5.4 eV and −2.9 eV, respectively, leading to a bandwidth in the visible regime of 2.2 eV [77], corresponding to a wavelength of 564 nm. It is a small hole transporting

molecule

Electron Acceptors

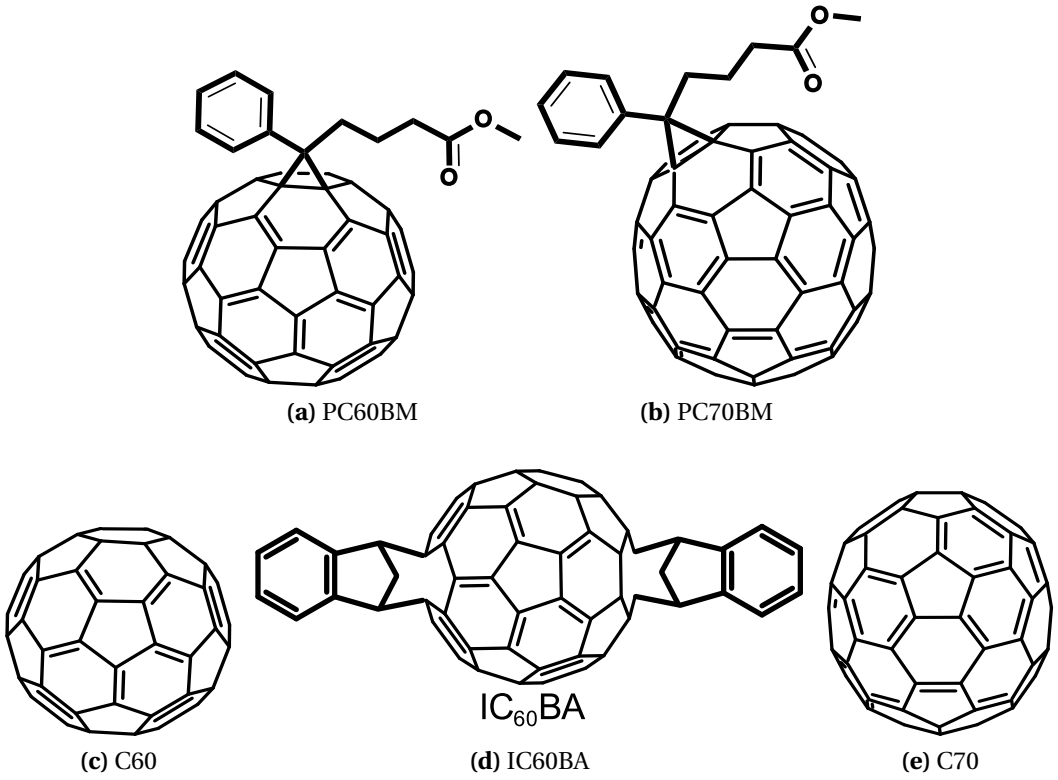

(a) PC60BM **(b)** PC70BM

(c) C60 **(d)** IC60BA **(e)** C70

Figure 5.5: Structures of **(a)** [6,6] − *Phenyl* − *C*61 − *butyric-acid* − *methyl-ester* ($PC_{60}BM$) **(b)** [6,6] − *Phenyl* − *C*71 − *butyric-acid* − *methyl-ester* ($PC_{70}BM$) **(c)** C_{60} **(d)** 1',1",4',4"-*Tetrahydro-di*[1,4]*methanonaphthaleno*[1,2:2',3',56,60:2",3"][5,6]*fullerene-C60* ($IC_{60}BA$) **(e)** C_{70}.

The main part of the fullerenes consists of C_{60} (Figure 5.5c) and C_{70} (Figure 5.5e) carbon balls named buckyball (see chapter 3.2 for additional information). The fullerene HOMO and LUMO level energies are mostly determined by cyclic voltammetry and shift depending on the used solvents. The HOMO and LUMO levels of C_{60} are approximately at −6.1 eV and −4.5 eV, respectively [78, 75], resulting in a 1.6 eV bandgap [79], corresponding to a wavelength of 775 nm. The HOMO and LUMO levels of C_{70} are similar to C_{60} and approximately at −6.2 eV and −4.6 eV, respectively [78, 80, 75], resulting in a 1.8 eV bandgap [81], corresponding to a wavelength of 729 nm. They are not suitable for solution processing and need to be evaporated. Nevertheless, we used them to get a better insight into the contribution of the fullerene side chains on the molecular energy levels in blends. The PCBM fullerenes chemically correct

names are [6,6] – *Phenyl* – *C*61 – *butyric-acid* – *methyl-ester* ($PC_{60}BM$ in Figure 5.5a), [6,6] – *Phenyl* – *C*71 – *butyric-acid* – *methyl-ester* ($PC_{70}BM$ in Figure 5.5b) and 1',1",4',4"-*Tetrahydro-di*[1,4]*methanonaphthaleno*[1,2:2',3',56,60:2",3"][5,6]*fullerene-C60* ($IC_{60}BA$ in Figure 5.5d). $PC_{60}BM$ and $PC_{70}BM$ are both not only very similar in shape, but also similar concerning their physical properties. They are two of the best known fullerenes investigated in organic photovoltaics and belong to the group of electron transporting organic semiconductors. As $IC_{60}BA$, they do have side chains for better solubility facilitating solution processing. The HOMO and LUMO levels energies do vary with the used measurement method, the ones of $PC_{60}BM$ are between -6.0 to -5.9 eV and -4.3 to -3.7 eV, of $PC_{70}BM$ between -5.9 eV and -4.2 to -3.9 eV and of $IC_{60}BA$ between -6.0 to -5.6 eV and -4.0 to -3.5 eV, respectively.

Comparing Molecular Orbitals

To get a first insight into their behaviour in a working solar cell device, we compared the aforementioned HOMO- and LUMO levels of the electron donors and acceptors presented in Figure 5.6. A direct LUMO level comparison of cyclic voltammetry data of $PC_{60}BM$ and $PC_{70}BM$ shows an energy difference of (6-10) meV [82, 83, 84, 85]. $IC_{60}BA$ and $PC_{70}BM$ LUMO levels differ by (170-210) meV [86, 87, 82, 88, 89, 90]. For C_{60} and C_{70} fullerenes without side chains a LUMO level difference of around 100 meV can be determined [91, 92, 93, 78, 80]. The reported differences in physical properties of C_{60}, C_{70} and their derivatives are small, but nonetheless they demonstrate that the molecules are energetically not identical.

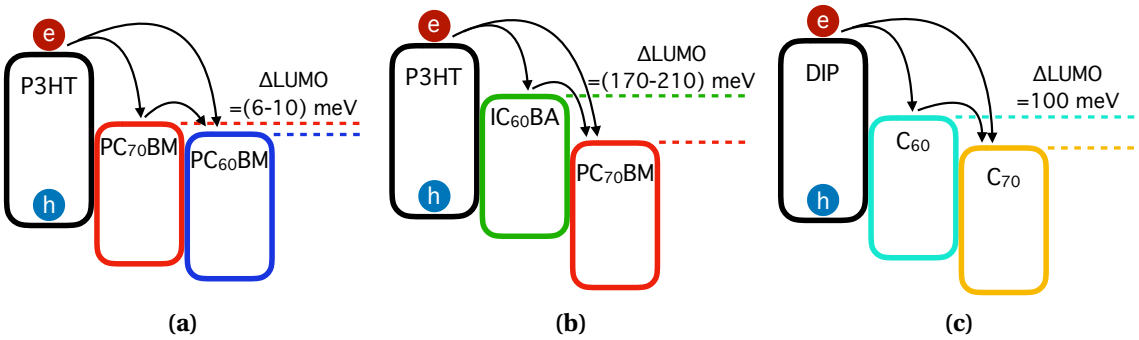

Figure 5.6: Schematic representation of the HOMO and LUMO energy levels of the pure materials. The fullerenes LUMO level differences in a blend would be **(a)** 10 meV for $PC_{60}BM$:$PC_{70}BM$, **(b)** (170-210) meV for $IC_{60}BA$:$PC_{70}BM$ and **(c)** 100 meV C_{60}:C_{70}. The arrows represent possible charge transfer pathways indicating the question of carrier distribution in blends.

5.2.2 Sample- and Preparation Details

Solar Cells

A common cell structure scheme was shown previously in chapter 4 Figure 4.1. PCBM fullerene derivatives are suitable for solution processing and therefore spin-coating as preparation method for the organic bulk heterojunction solar cells was chosen. At first, a ≈40 nm thick layer *poly*(3,4-*ethylenedioxythiophene*):*poly*-(*styrenesulfonate*), short PEDOT:PSS, purchased from Heraeus (Clevios AL4083), is spin-coated on top of a glass substrate covered with a 150 nm thick indium tin oxide (ITO) electrode. PEDOT:PSS is a hole transport- and electron blocking layer to increase the device performance. It is also water based and has to be annealed for 10 min. at 130° C to remove any residual humidity. Afterwards the substrates are moved into a nitrogen atmosphere glove box to avoid exposure to oxygen and humidity. PCBM solutions ($30^{mg}/_{ml}$) were also produced inside this glove box by dissolving the PCBM powders separately in chlorbenzol (CB). The blends were mixed before they are spin coated on top of PEDOT:PSS resulting in an active layer thickness of around 100 nm. For the final step it is necessary to remove a small part of the active materials layer to be able to contact the ITO bottom electrode. The active material is simply wiped of with a solvent soaked cotton swab. Then, cells are transfered into an evaporation chamber (base pressure $<1 \cdot 10^{-6}$ mbar) to deposit the calcium (Ca) and aluminium (Al) cathode. A shadow mask is used to get an active area of 3 mm^2. The 3 nm thick Ca layer is evaporated with a rate of 0.2-0.3 $^{Å}/_{s}$ followed with 120 nm Al with 3-7 $^{Å}/_{s}$. If oxygen and hydrogen removal was necessary, sample annealing under vacuum at 140° C was performed. j-V sweeps were performed directly after the evaporation inside the glovebox to characterise the devices. The illumination source was a simulated AM1.5G spectrum. Unlike PCBMs, C_{60} and C_{70} are fullerenes without side chains facilitating solubility, hence they are preferably evaporated to deposit the active layer. This results in a very homogeneous distribution of both fullerenes, i.e. a heterointerface throughout the whole layer. The C_{60} and C_{70} samples were prepared by *Michael Brendel*. Depending on the sample, the cells were grown layer by layer, or both fullerenes were deposited at the same time. With these two techniques, bilayer or mixed layer cells were produced. The DIP layer was 30 nm thick, single or co-deposited fullerene layers 35 nm.

EPR samples

As these samples are actual active solar cell layers an utterly different way of production was used as described in chapter 4.1.2. In comparison to a working solar cell device there is no need to extract charge carriers, therefore one can omit the electrodes.

To reach proper signal to noise ratios in EPR it is necessary to have enough active material in the spectrometer. Therefore, a polyethylen overhead projector foil of 0.1 mm thickness from Avery was used as substrate. The active layers are applied as described previously. Simply (in reality it's of course never that simple) cut the foil into slices of ≈3x20 mm and stacked between 10 to 14 layers in one EPR tube. Afterwards, the tube was evacuated and flushed with helium a few times over a period of 15minutes. Sample annealing at 140° C was performed if necessary. As absorbed water evaporates at these temperatures, five to ten times helium flushing removes almost every residue. Finally, the tubes were sealed off under 10 mBar helium atmosphere.

5.2.3 Solar Cell Characterisation

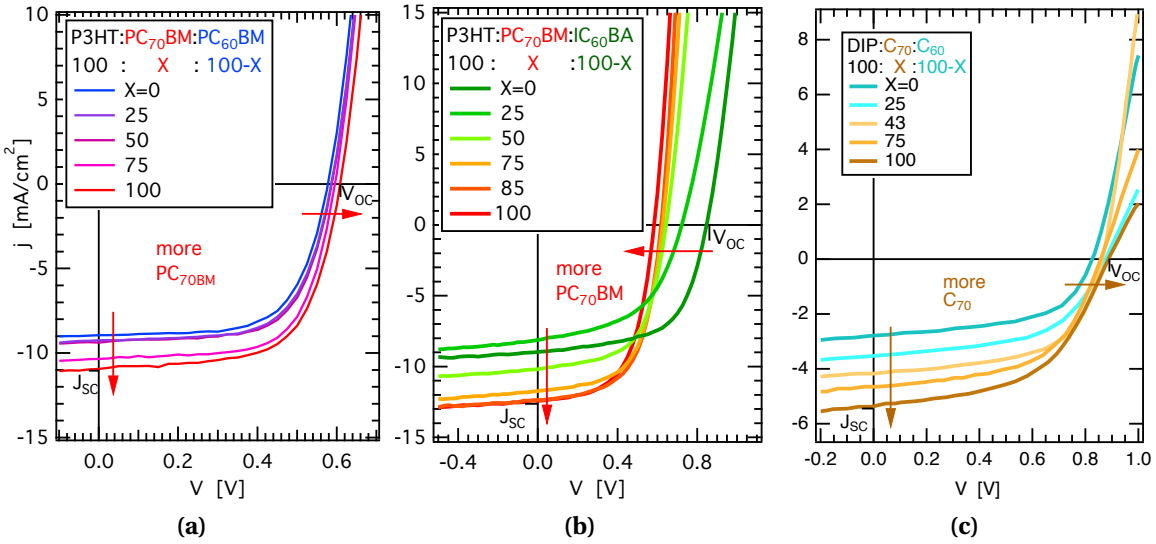

Figure 5.7: Averaged j-V curves of **(a)** $PC_{70}BM$:$PC_{60}BM$ and **(a)** $PC_{70}BM$:$IC_{60}BA$ fullerene blends with the polymer P3HT, **(c)** C_{60} and C_{70} fullerene blend with the small molecule DIP [*C_{60}:C_{70} cells were build and measured by Michael Brendel* [93]. X represents the weight percent of C_{70} derivatives with respect to the second fullerene. In all cases, increasing the amount of C_{70} derivatives continuously increases the short circuit current j_{SC} due to C_{70}'s higher optical absorption. **(a)** The V_{OC} follows the $PC_{70}BM$ weight percent, leading to a minor increase of (30±2) mV. **(b)** The V_{OC} radically drops with increasing $PC_{70}BM$ amount by (250±10) mV . **(c)** The V_{OC} follows the C_{70} weight percent, leading to an increase of (50±5) mV.

Figure 5.7 shows the averaged current-voltage (j-V) curves for cells with one donor (P3HT, DIP) together with two fullerene acceptors of varying stoichiometry. The ratio between donor and the total fullerene content remains constant. Every curve was determined by averaging between 5-15 devices, errors are given by the standard de-

viations. As indicated, X represents the weight percent of the C_{70} derivative, 100-X the weight percent of the C_{60} derivative. In all cases, the short circuit current (j_{SC}) increases for an increasing amount of C_{70} derivatives. This j_{SC} gain is directly explained with their higher optical absorption in comparison to C_{60} derivatives.

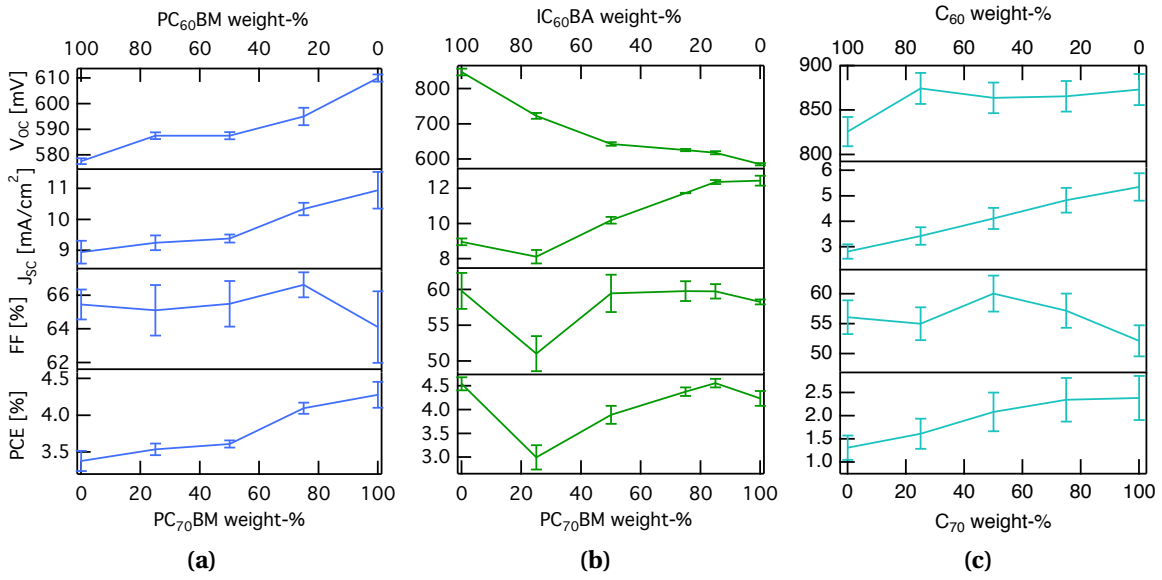

Figure 5.8: V_{OC}, j_{SC}, FillFactor (FF) and Power Conversion Efficiency (PCE), including their standard deviation for the aforementioned solar cells. **(a)** $PC_{70}BM$:$PC_{60}BM$ and **(b)** $PC_{70}BM$:$IC_{60}BA$ blends with P3HT and **(c)** C_{70}:C_{60} with DIP. Error bars represent the standard deviations.

j-V characteristics for different stoichiometric ratios of $PC_{70}BM$:$PC_{60}BM$ are given in Figure 5.7a. The extracted solar cell parameters are shown in Figure 5.8a. Due to the higher optical absorption of $PC_{70}BM$, the j_{SC} increases from 9 $\frac{mA}{cm^2}$ to 11 $\frac{mA}{cm^2}$ for 0 % to 100 % weight percent $PC_{70}BM$, respectively. Additionally, the j-V curves are indicating a slight increase in V_{OC} of 30 mV from 580 mV to 610 mV with the $PC_{70}BM$ amount. This is a surprising result, as the $PC_{70}BM$ LUMO is assumed to lie only around 10 meV lower in energy than the $PC_{60}BM$ LUMO (see Figure 5.6a). The j-V curves of different stoichiometric ratios of $PC_{70}BM$:$IC_{60}BA$ are shown in Figure 5.7b. In this configuration j_{SC} increases from 9$\frac{mA}{cm^2}$ to 13$\frac{mA}{cm^2}$ for 0 % to 100 % weight percent $PC_{70}BM$, respectively. In contrast, V_{OC} decreases tremendously upon addition of $PC_{70}BM$. From 0 % to 100 %, it drops quite substantially by 250 mV from 820 mV to 600 mV. As the $PC_{70}BM$ LUMO lies around (170-210) meV lower in energy than the $IC_{60}BA$ LUMO, shown in Figure 5.6a), the V_{OC} decrease is close to what would be expected according to equation 5.4. The j-V curves of different stoichiometric ratios of co-evaporized C_{60}:C_{70} layers are shown in Figure 5.6c. In this configuration j_{SC} increases from 3 $\frac{mA}{cm^2}$ to 5 $\frac{mA}{cm^2}$ for 0 % to 100 % weight percent C_{70}, respectively. There, the V_{OC} increased by around 50 mV from

825 mV for 0 % to 875 mV for 100 % weight percent C_{70}. Similar to the $PC_{70}BM$:$PC_{60}BM$ sample, this result was quite surprising, as the C_{70} LUMO lies around 100 meV lower in energy than C_{60}, as shown previously. As we can see, the LUMO level differences of the pure materials are not always transferred into the open circuit voltages of the devices. This is not unexpected, as the V_{OC} could also be influenced by a change of the recombination parameters, but they can't be determined by EPR and are beyond the scope of this work. Furthermore, the recombination processes can be assumed to be negligible at cryogenic temperatures at which our EPR measurements are performed [94]. Thus, to determine if the V_{OC} changes are caused by changes in the LUMOs we investigate the electron distribution on the molecular level via quantitative EPR.

5.3 Energy Difference Between Molecular Orbitals of Distinct Fullerenes

In this section we will reveal the actual energetic landscape of our organic solar cells by means of qualitative and quantitative EPR. Concerning their EPR spectra it is known that electrons and holes in organic semiconductors often deviate significantly in spectral position and shape. Thus, it is possible to distinguish between electrons localised on the distinct fullerene derivatives, making the electron population densities of the two fullerenes directly accessible. Utilising the Boltzmann distribution correlated with the respective material amounts in the cells, we are able to estimate the actual energetic difference for an electron being localised on either fullerene. This energy difference is the actual ΔLUMO of the two mixed fullerenes, which significantly deviates from the reported literature values for the separate materials. These information indicate the formation of an effective LUMO level between the excited fullerenes and reveals that they can not be treated separately if mixed. The orbital reorganisation in blended C_{60} and C_{70} fullerenes is observed for the first time and strongly supports our findings.

5.3.1 Dependence of EPR Signal Intensities on Stoichiometry

The light induced EPR spectra (solid lines) of the solar cell blends are shown in Figure 5.9, determined by subtracting the spectrum without illumination from the spectrum illuminated with a white light LED. They are superpositions of the individual components shown as dashed lines and can be disassembled by simulations via EasySpin [20]. The necessary exact P3HT, $PC_{70}BM$ and $PC_{60}BM$ g-tensor values are known in literature [95, 96, 97]. C_{60}^{-} is reported in literature, but the given g-tensors do vary [98, 99, 100].

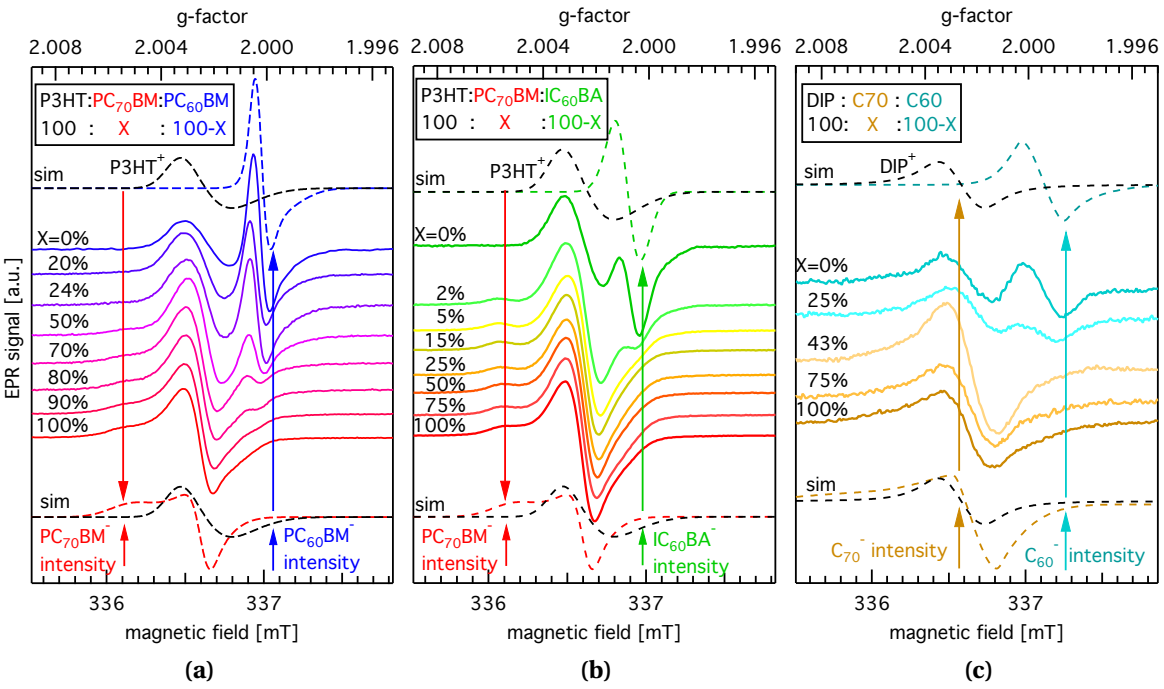

Figure 5.9: EPR spectra (solid lines) of solar cell blends with different stoichiometric fullerene ratios under white light illumination, taken at T=30K. Dashed lines show simulations of the donor cations ($P3HT^+$ and DIP^+) (black) and the acceptor anions $PC_{60}BM^-$(blue), $PC_{70}BM^-$(red), $IC_{60}BA^-$(green), C_{60}^- (turquoise) and C_{70}^- (gold). Vertical arrows are added as a guide to the eye to follow the fullerene intensity changes. **(a)** P3HT:$PC_{70}BM$:$PC_{60}BM$ samples, indicating signal intensities proportional to the corresponding material amounts. **(b)** P3HT:$PC_{70}BM$:$IC_{60}BA$ samples show a rapid decrease in $IC_{60}BA$ intensity after adding a few (2-5) percent $PC_{70}BM$. **(c)** DIP:C_{60}:C_{70} samples indicate a C60- signal intensity weaker than the corresponding material amounts. The extraordinary strong signal at 43% C_{70} is a special case and will be discussed separately in chapter 5.3.2.

Utilizing the mentioned parameter sets for an elaborate EPR investigation all distinct ion spectra could be simulated. Here it is important to note that the surrounding matrix changes the g-tensor of the surrounded material, thus the literature parameters were slightly adjusted to our systems [101, 102, 103, 104]. The g-tensor values for the fullerenes are given in table 5.1. Errors for g-values are ±0.0005 for C_{60}^-, ±0.005 for C_{70}^-, ±0.00005 for $PC_{60}BM^-$, ±0.00005 for $PC_{70}BM^-$ and ±0.00005 for $IC_{60}BA^-$. They do vary due to different signal to noise ratios and the overlap of the signals. P3HT values were $g_{xx} = 2.0030(0.002)$, $g_{yy} = 2.0022(0.0015)$ and $g_{zz} = 2.0009(0.0015)$ including the g_{Strain} values in brackets. The distinct g-factor distribution g_{Strain} is responsible for the EPR signal width, with $\sigma_{g_{Strain}} = 0.0001$ being equal to $\sigma_{\Delta H} = 0.010\,\text{mT}$ at the experimental frequency of 9.432 GHz. Due to the poor g-factor resolution and missing literature values we used a single g-factor for DIP, yielding $g = 2.0033$ and a gaus-

sian broadening of 0.2 mT. The donor cations ($P3HT^+$, DIP^+) (black) and fullerene acceptor anions $PC_{60}BM^-$ (blue), $PC_{70}BM^-$ (red), $IC_{60}BA^-$ (green), C_{60}^- (turquoise) and C_{70}^- (gold) are shown as dashed lines in Figure 5.9.

g	C_{60}^-(strain)	C_{70}^-(strain)	$PC_{60}BM^-$(strain)	$PC_{70}BM^-$(strain)	$IC_{60}BA^-$(strain)
g_{xx}	2.0000 (0.0014)	2.0085 (0.00193)	2.00052 (0.00041)	2.00543 (0.00193)	2.00075 (0.00064)
g_{yy}	2.0000 (0.0002)	2.0030 (0.00064)	2.00031 (0.00057)	2.00265 (0.00064)	2.00023 (0.00083)
g_{zz}	1.9993 (0.0038)	2.0020 (0.00203)	1.999 (0.00190)	2.00235 (0.00203)	2.00295 (0.00091)

Table 5.1: The determined g-tensor values for all fullerenes studied in this work.

In all cases, the amount of the C_{70} derivative increases from top to bottom, ranging from 0 % to 100 %. The gradual change of the spectra from X=0% (only P3HT:$PC_{60}BM$) to 100% (only P3HT:$PC_{70}BM$) can be seen in Figure 5.9a. It is a manifestation of the shifting intensities of the $PC_{60}BM^-$ and $PC_{70}BM^-$ signals in the spectrum as indicated by the blue and red arrows, respectively. *[P3HT:$PC_{60}BM$:$PC_{70}BM$ EPR sample preparation and evaluation done by Andreas Sperlich].* The signals intensities seem to be in perfect agreement with the corresponding fullerene material ratios present. Additionally, exemplary measurements have been performed by *Andreas Sperlich* with different polymers, indicating no influence on the electron distributions between the two fullerenes. For P3HT together with $PC_{70}BM$:$IC_{60}BA$ a much more rapid change of $IC_{60}BA$ intensity can be seen in Figure 5.9b, as indicated by the green vertical arrows. Only a minor amount of $PC_{70}BM$ (2-5%) causes the $IC_{60}BA$ signal to almost vanish completely (dark to light green spectrum). For more than just a few percent $PC_{70}BM$ and $IC_{60}BA$ signal can't be observed. Figure 5.9c shows the spectra for samples with DIP and C_{60}:C_{70}. The C_{60}^- signal can't be seen above C_{70} concentrations of 25%. Considering the intensity shift, the C_{60} electron affinity seems to lie somewhere between that of $PC_{60}BM$ and $IC_{60}BA$. The extraordinary strong signal for an almost equal ratio of C_{60} and C_{70}, i.e. X=43% C_{70}, is a special case. It will be discussed separately in section 5.3.2 of this chapter.

To determine an accurate correlation between the EPR signal intensities and the corresponding material weight percent a more sophisticated evaluation is needed. Therefore, we reproduce the EPR spectra for every fullerene ratio by varying the distinct signals (dashed lines) contributions in EasySpin simulations. The so gained intensities are plotted versus their weight percent in the corresponding samples presented in the next section.

Modelling EPR Intensities based on a Boltzmann Distribution

Let us first recall the working question: Can we treat fullerenes in mixtures as if they are separate? If we assume that to be true, we can also assume a two level system

for the electrons on the fullerenes. The energy separation ΔE is given by the LUMO levels difference (see chapter 5.2.1). Therefore, the electrons probability distribution between these two fullerene levels (N_{100-X},N_X) in percent should be described by the Boltzmann distribution:

$$\frac{N_{100-X}}{N_X} = \frac{X}{100-X} \exp\left(\frac{-\Delta E}{k_{BT}}\right) \tag{5.3}$$

where $\frac{X}{100-X}$ is given by the stoichiometric fullerene weight ratio corresponding to the statistical weight of the two LUMO levels, T is the temperature and k_B the Boltzmann constant. The extracted fullerene EPR signal intensities versus their corresponding weight ratios X and 100-X are shown in Figure 5.10. Errors in intensity are due to the low signal to noise ratios and overlapping signals resulting in fitting uncertainties. Errors in the weight ratios are due to the uncertainties in weighting. As they are in the range of the marker size they are omitted for clarity.

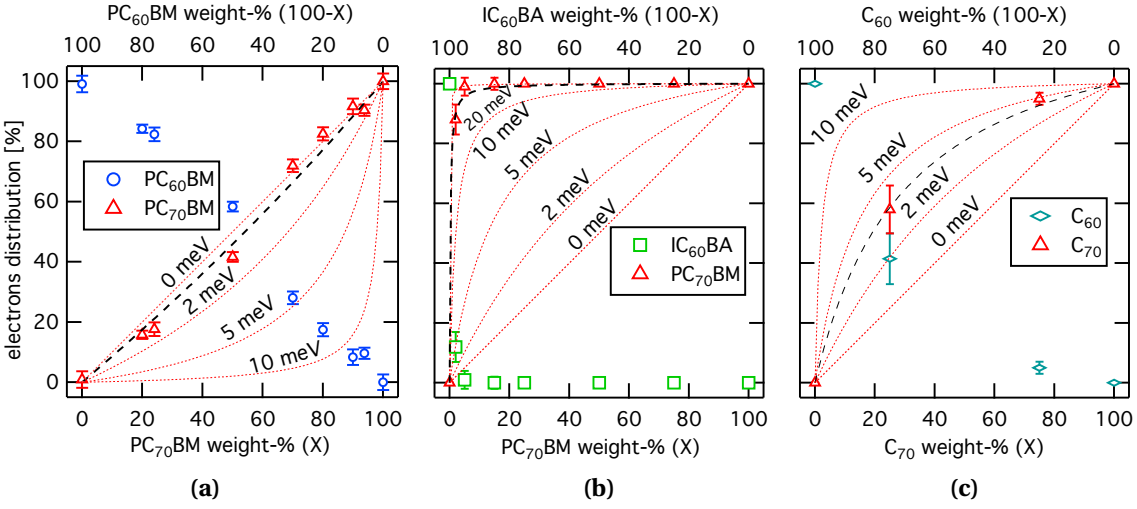

Figure 5.10: Electron distributions N_{100-X},N_X versus fullerene weight ratios X and 100-X between **(a)** $PC_{70}BM$ & $PC_{60}BM$, **(b)** $PC_{70}BM$ & $IC_{60}BA$ and **(c)** C_{70}:C_{60}. Dotted red curves are exemplary Boltzmann distributions for the energy of an electron being **(a)** a few meV higher on the C_{70} derivative and **(b)** & **(c)** a few meV lower on the C_{60} derivative. The black dashed lines are fits using equation 5.3. They yield LUMO level energy differences below 2meV for $PC_{70}BM$ & $PC_{60}BM$, (10-20) meV for $PC_{70}BM$ & $IC_{60}BA$ and (2-5) meV for C_{70}:C_{60}. *[P3HT:PC_{60}BM:PC_{70}BM EPR sample preparation and evaluation done by Andreas Sperlich]*

To get an idea about the extraordinary energy difference sensitivity of the electrons distribution at 30 K we added exemplary Boltzmann distributions (red dotted) for various LUMO level differences from 5 to 20 meV. If they are in the lower right of the graph, the C_{70} derivative lies lower in energy than the C_{60} derivative, if they are in the upper left it is the other way around. Considering the error bars, a fit of the distribution equa-

tion 5.3 to the data points results in the black dashed lines. Figure 5.10a does present the aforementioned evaluation for the case of the $PC_{70}BM$:$PC_{60}BM$ blend. One can see an almost even distribution between the two fullerenes, indicating that the energy difference lies well below 2meV. This result is below the energy difference of (6-10) meV as expected from the energies of the pure materials. $IC_{60}BA$:$PC_{70}BM$ fullerene blends are shown in Figure 5.10b. The fit indicates a remarkably low energy difference of (10-20) meV, considering the (170-210) meV of the pure materials as discussed previously. All in all, we determine a tremendous energy shift of at least 150 meV while going from separate fullerenes to a blend. For the C_{60}:C_{70} mixed layers our EPR intensity analysis are plotted in Figure 5.10c. The fit of the EPR intensities indicates an energy difference of only (2-5) meV. A comparison with the pure materials energy levels, shown previously, reveals a huge shift of (90-100) meV between separate fullerenes and the blend. For all fullerene derivatives used in this chapter we could see a shift of the molecular orbital energies, i.e. formation of an effective LUMO, if we go from separate fullerenes to fullerenes in a blend. The energy shifts lie between 6 to 200 meV, clearly indicating that we can't treat fullerenes in mixtures as if they are energetically separate. Furthermore, we did find a strong hint for the interaction of molecular orbitals in fullerene mixtures. A detailed description shining light on the orbital reorganisation in excited fullerenes is given in the next section.

5.3.2 Orbital Reorganisation Upon Fullerene Blending

The C_{60} & C_{70} blend EPR signal

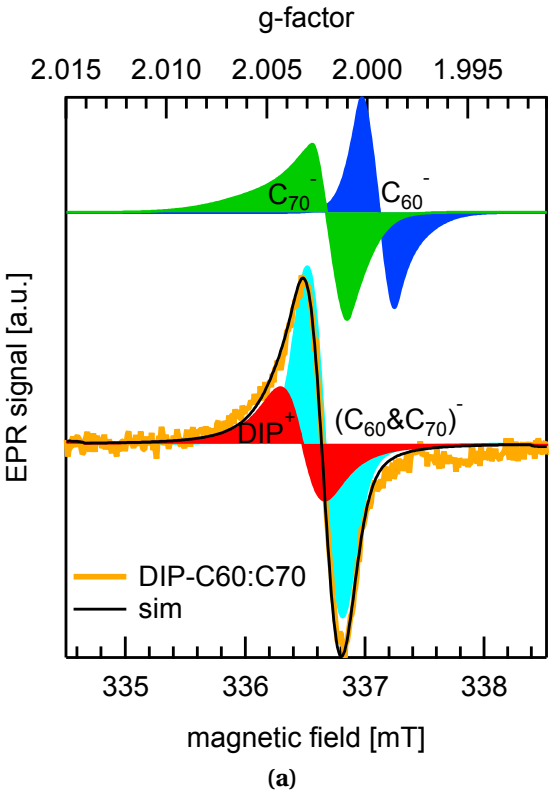

(a)

g	C_{60}^-	$(C_{60}\&C_{70})^-$	C_{70}^-
g_{xx}	2.0003	2.0026	2.0085
g_{yy}	1.9995	2.0015	2.0030
g_{zz}	1.9982	2.0008	2.0020

(b)

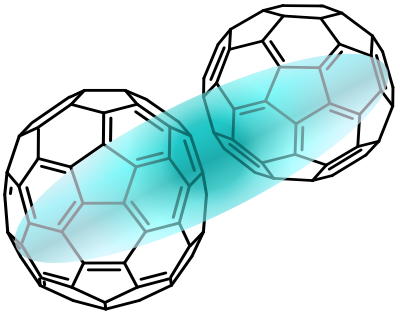

(c)

Figure 5.11: a) Light induced EPR spectrum of an active layer for a DIP solar cell with a 57%:43% mixed C_{60}:C_{70} fullerene blend. The DIP^+ signal (red) could be detected, but not C_{60}^- (blue) or C_{70}^- (green). Instead, a new state is observed which we named $(C_{60}\&C_{70})^-$ (turquoise). **b)** g-tensors of the relevant materials. As the $(C_{60}\&C_{70})^-$ state's g-values lie "in between" them of C_{60}^- & C_{70}^- a delocalised state over both fullerenes seems most reasonable. **c)** Schematic representation of a delocalised electron between C_{60} & C_{70}. Note, the highest density lies in between the fullerenes.

For an almost equal mixture of C_{60} & C_{70} (57%:43%) in a fullerene blend together with DIP an unexpected light induced EPR signal could be detected, the spectrum (yellow) is shown in Figure 5.11a. It is determined by subtracting the spectrum without illumination from the spectrum illuminated with a white light LED. The contribution of DIP (red) was already discussed in the previous section. The signatures for C_{60}^- (blue) and C_{70}^- (green) are added for comparison. Surprisingly, a superposition of these two signals can not reproduce the EPR signal contribution (turquoise) in the ternary blend, determined via EasySpin simulations (black). This turquoise signal, clearly deviating from the pure C_{60}^- (blue) and C_{70}^- (green) EPR signatures, is named $(C_{60}\&C_{70})^-$ and results from a comprehensive EPR study. The determined g-tensor is given in table 5.11b

and shows values "in between" that of C_{60}^- & C_{70}^-, given for comparison. Due to the low signal to noise ratio and especially the signal overlap we have to assume g-value errors around ±0.0005.

The $(C_{60}\&C_{70})^-$ g-tensor indicates a low anisotropy of the state and an orbital contribution from both fullerenes. Therefore, we assume a "delocalised electron" where the electron wave function delocalises over two, or even more fullerenes of the C_{60} and C_{70} type. A quite similar signal has been observed for a soluble C_{60}-C_{70} heterodimer by Poluektov et al. [96]. Their heterodimer consists of one C_{60} & one C_{70} fullerene each with a pyrrolidine ring connected via a benzene ring.

Nevertheless, our assumption of an excited electron state connecting two fullerenes is consistent with theoretical predictions by Menon et al. based on tight-binding molecular dynamic simulations after UV illumination resulting in C_{60} dimers [105]. Additionally, Shubina et. al. described the delocalisation of electron wave functions in C_{60} fullerene clusters by DFT calculations [45]. There, a single occupied σ-bond is formed between the fullerenes, creating Van der Waals oligomers. Their predicted signal could not be seen by EPR in pure C_{60} or C_{70} clusters, but could be detected in C_{60}:C_{70} mixtures. A reason for that might be the significantly different wave function and therefore EPR signal in the case of coupling between different fullerene types. Their calculations indicate the orbital coupling of up to four fullerenes. If the coupling state would be delocalised over more than two fullerenes, we would expect an equally smeared out g-tensor. If that is the case we might not be able to detect an EPR signal as it is widely distributed and merges with the background noise. Therefore, we assume an electron wave function distributed between C_{60} and C_{70}. First, our results support the theoretical predictions by Shubina et al., and second, they indicate that the delocalisation is not restricted to C_{60} fullerene clusters. It also does occur between C_{60} and C_{70} fullerenes and probably their derivatives. To our knowledge, this has been observed experimentally for the first time upon blending of distinct fullerenes.

As the electron wave function is generally rather located on the buckyball surface, the side chains are less likely to have an effect on the electron distribution. Therefore, it seems reasonable that the delocalisation of the electron also causes the LUMO level energy shift for the fullerene derivatives discussed in the previous sections. Similarly, Mollinger et al. addressed the V_{OC} change in ternary blends to modified CT state delocalisation [70]. In conjugated polymers, reorganisation of the polymer geometry around charges has been shown to cause rearrangements of the energy levels [106, 107]. All in all, we generally assume the effective LUMO to be formed between the fullerene's buckyballs causing the gradual shift of the V_{OC}.

5.3.3 Discussion

First of all we want to point out that there are too many factors, like recombination and sample illumination intensity, influencing the V_{OC} of a solar cell device which are not detectable via EPR and beyond the scope of this work. Nevertheless, we will briefly discuss a few possible effects that might explain why the changes on the molecular orbital level are not transferred into the V_{OC}. A wide overview over V_{OC}s in various polymer fullerene blend systems can be found in [108]. Generally, V_{OC} depends linearly on the energetics of the CT state, which in turn is mainly determined by the difference between the donor polymer HOMO and the LUMO of the electron acceptor (see chapter 5.1.1 for comparison). Mollinger et al. attributed the E_{CT} and thus V_{OC} trends to changes in the CT state neighbourhood, alloy formation, or local dipoles [70]. All these effects can explain the shift in V_{OC}. Additionally, the energetic loss between the energy of the interfacial CT state and V_{OC} was shown to be determined almost equally by radiative and non-radiative losses [109, 110]. $V_{OC} = \frac{E_{CT}}{q} - V_{rad} - V_{non-rad}$. These voltage losses do appear in all materials, but are assumed to be in the same order for the different fullerene derivatives. Therefore, they only partly contribute to the observed shift. Voltage losses can also depend on the intermolecular interactions of the donor materials [111], but have not yet been reported for fullerene acceptors.
Concerning the EPR distributions, we want to emphasise that they are not influenced by different optical absorptions. This is evident as continuous illumination yields an equilibrium state where charge transfer occurs much faster ($<10^{-9}$ s) than cw EPR detection (≈100 ns). A general model giving rise to energy shifts in the LUMO of organic semiconductors has been proposed by Schwarze et. al based on long range electrostatic interactions due to quadrupole moments [68]. Despite the fact that they are dealing with strong, out-of-π-plane moments in fluorinated FXZnPc, their results for the HOMO and LUMO level shifts are qualitatively very similar to ours. Therefore, it would be interesting to investigate the quadrupole moment of fullerenes, as this might also have an influence on the energetic landscape and hasn't been done so far to our knowledge.
In general, our EPR data are very well and consistently explained with a Boltzmann distribution between the two LUMO levels of the mixed fullerenes with an energy difference being (0±2) meV for $PC_{60}BM$:$PC_{70}BM$, (18±2) meV for $IC_{60}BA$: $PC_{70}BM$ and (3±2) meV for C_{60}:C_{70}, an overview is given in Figure 5.12. There we did consider uncertainties in literature, the weighting and the evaluation process.

The energy shift is well-described with the formation of an alloy. Alloy formation has been confirmed for PCBM and ICBA mixtures with P3HT by Angmo et al. [112], and in Phthalocyanine:C_{60} mixtures by Olguin et al. [113]. There, the change of the ground state electron density between a Phthalocyanine and C_{60} complex polarises the fullerene, resulting in an interfacial dipole. The alloy effect after excitation might yield an effective LUMO that leaves the materials absorption shapes widely unchanged, what has been observed experimentally [93, 114, 115, 87, 116, 117]. As the situations seem to be fairly different for the different fullerene blends we want to discuss them separately in the next sections. All in all, we want to point out that the LUMO level energies of mixed fullerene derivatives generally seem to align.

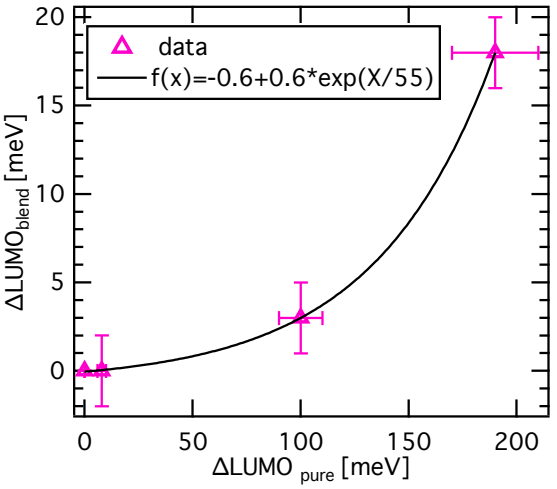

Figure 5.12: Overview of the LUMO level differences in the pure materials and the blend. The alloy formation $\Delta LUMO_{blend}$ seems to depend exponentially on the LUMO level separation $\Delta LUMO_{pure}$ shown as a guide to the eye (black).

$PC_{70}BM$ & $PC_{60}BM$

Here, the inhibited aggregation of $PC_{60}BM$ upon adding $PC_{70}BM$, increases the CT state energy (E_{CT}) and might therefore explain the higher V_{OC}. Piersimoni et. al observed a similar V_{OC} shift to lower values by (80-90) mV for an increasing $PC_{60}BM$ weight percent in MDMO-PPV:$PC_{60}BM$ solar cells [118]. As they saw a $PC_{60}BM$ phase separation into crystalline nano-clusters for increasing weight percents, this is assumed to cause the CT energy- and therefore V_{OC} shift. Similarly to our assumed situation for the molecular orbital levels, it is most likely due to delocalisation of the electron wavefunction over the crystallites [119]. On the other hand, the voltage effect might also be caused by the overlap of the DOS as they are only a few tens of meV wide and the pure material spectra indicated a LUMO separation of only a few tens meV. This assumption holds true for at least $PC_{60}BM$:$PC_{70}BM$ based blends, but can't be applied to the other cases in this work. For overlapping DOSs in a two-electron donor mixture with one acceptor Felekidis et. al suggested that an energetic recalibration could occur due to charges filling a joint density of states [69]. They explain the continuous tuneability of the V_{OC} with a model of quasi Fermi level splitting (Fermi-Dirac statistics). They also quantitatively reproduce the V_{OC} change in their bulk heterojunctions for differ-

ent donor blend ratios. In their experiments a higher HOMO level difference between the donors also caused a more abrupt V_{OC} change, an effect we couldn't observe in our fullerene blends. Therefore, their explanation does not seem to be applicable for the other fullerene mixtures in this work.
All in all, a V_{OC} shift in the OPV device due to crystal formation of $PC_{60}BM$ can be expected, explaining the 30 mV V_{OC} increase in our solar cells for an increasing amount of $PC_{60}BM$. On the molecular level we find two slightly different LUMO levels for pure $PC_{60}BM$ &$PC_{70}BM$ and an energy shift by (6-10) meV to practically 0 meV difference in the blend. In accordance with the aforementioned and following effects the formation of an alloy can explain this shift.

$IC_{60}BA$ & $PC_{70}BM$

Here, the V_{OC} change has already been investigated in literature and addressed to alloy formation [120], LUMO level differences [114], and other effects, an overview is given in [108]. As the substitutions in $IC_{60}BA$ hinder crystallisation we would rather get localised than delocalised wave functions, making crystallisation unlikely to be the reason for the energy shift [121, 119]

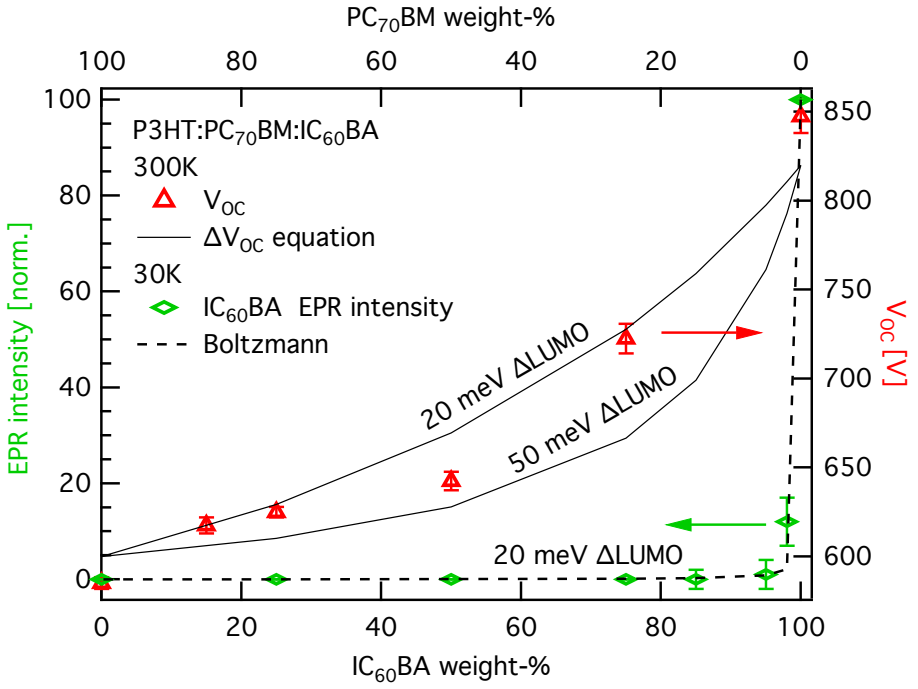

Figure 5.13: P3HT:$IC_{60}BA$:$PC_{70}BM$ V_{OC} and EPR signal intensity correlation. The Boltzmann distribution describes the EPR intensity distribution at 30 K. The V_{OC} at 300 K reasonably follows equation 5.4.

Therefore, for $IC_{60}BA$ and $PC_{70}BM$ the formation of an alloy is presumably the only effect strong enough to explain the LUMO level shift of at least 150 meV. As alloy formation seems to be the dominating effect upon the voltage in this case, it intriguingly can be used to reproduce the V_{OC} shift as shown in Figure 5.13 via the following equation:

$$\Delta V_{OC} = \frac{\Delta LUMO_{pure}}{q} \cdot N_{IC_{60}BA} \tag{5.4}$$

In this empirical equation we simply consider the $\Delta LUMO_{pure}$ level difference of the pure materials as well as the weighted Boltzmann distribution $N_{IC_{60}BA}$ with the $\Delta LUMO_{blend}$ level difference determined for the blend at room temperature (see equation 5.3 for comparison). It nicely reproduces the voltage shift, indicating that the LUMO levels of both fullerenes did shift in energy in the blend to be as close as (18±2) meV, but the V_{OC} sweeps between the two pure material LUMO levels according to their stoichiometry. Therefore, the effective alloy LUMO level seems to be just a linear combination of the two pure material LUMO levels. All in all, it seems that alloy formation dominates all other effects in $IC_{60}BA$ & $PC_{70}BM$ mixtures, making it the perfect model system to investigate alloy formation.

C_{60} & C_{70}

Attributing the voltage change to morphology differences is not a big issue in planar junctions with buckyballs, as shown explicitly for our system by Brendel [93]. On the other hand phase separation at the DIP:fullerene interface could have a relevant effect as orientation, the correlated dipole direction and aggregate size influence the loss mechanisms [122, 123]. As the DIP interface is not assumed to be much different with C_{60} or C_{70}, we would expect a rather small shift. In the solar cell devices investigated by Brendel the V_{OC} increases by up to 50 mV upon addition of C_{70}, despite the LUMO in C_{70} being about 100 mV lower. We assume that this is caused by a combination of the aforementioned mechanisms. Nevertheless, the active layer PL spectra indicate less higher and more lower energetic states consistent with the LUMO shift seen in EPR. A shift of the C_{60} & C_{70} photoemission has also been seen for alkali doped fullerides by Weaver et al. [78], indicating HOMO LUMO level shifts. Our evaluation of the EPR signal intensities revealed an energetic recalibration after excitation leading to an effective LUMO level difference of (4±2) meV, which is significantly smaller than the energy difference of 100 meV determined from pure material energies. This result is consistent with theoretical predictions [45, 105], discussed in detail in the previous section 5.3.2, describing the delocalisation of electron wave functions in C_{60} fullerene clusters

resulting in completely new molecular orbitals and energies. Therefore, the formation of an alloy most probably causes the LUMO level shift of around (90-100) meV.

5.3.4 Summary

Motivated by the continuously tuneable open circuit voltage (V_{OC}) in ternary fullerene-based solar cell devices, we investigated the energetic landscape on the molecular level as a function of the fullerene blend ratios. We have shown the reorganisation of the LUMO levels for five different fullerene derivatives, i.e. three fullerene pairings. While pristine material spectra indicated LUMO level differences of (6-10) meV for $PC_{70}BM$:$PC_{60}BM$, (170-210) meV for $PC_{70}BM$:$IC_{60}BA$ and 100 meV for C_{70}:C_{60}, we were able to estimate energy differences of respectively (0±2) meV, (18±2) meV and (3±2) meV in ternary blends of organic solar cells; an overview is given in Figure 5.12. These quite fascinating results were determined by application of quantitative EPR and a comparison of measured EPR signal intensities with the weight ratio of the contained fullerenes and the weighted Boltzmann distribution. The EPR results determined for $PC_{60}BM$:$PC_{70}BM$ mixtures do indicate the formation of an effective LUMO, while the V_{OC} change in corresponding solar cells is most probably explained by crystallisation. As C_{60} and C_{70} have no side chains that might result in some dipole-dipole alignment related to crystallisation and thus an energy shift, we can assume that the fullerene LUMOs actually interact to form a new orbital. This assumption is supported by theoretical calculations predicting the delocalisation of the electron wave function between buckyballs and our observation of an dimer state in EPR. Why the V_{OC} increases for an increasing C_{70} ratio in the device could not be explained due to the numerous factors influencing the V_{OC}. Quite interesting results have also been determined for the $PC_{70}BM$:$IC_{60}BA$ fullerene configuration. While the V_{OC} of the solar cell device increases by 250 mV for an increasing $IC_{60}BA$ ratio, the electron distribution still behaves just as the two LUMO levels would be separated by only 18 meV. These results corroborate the assumption that a new LUMO orbital is formed if we blend two different fullerene derivatives.

In summary, there are many factors influencing the V_{OC} of a solar cell device. Therefore, the changes of the molecular orbital levels are not always transferred directly into the V_{OC} of the device. Not all of these factors are detectable via EPR and beyond the scope of this work. All in all, it is obvious to see that fullerene LUMO energies in blends can not be treated as separate, but rather as a linear combination resulting in sweeping charge transfer properties.

6 Charge Transfer of (6,5)-SWNTs

The first section will deal with the basic EPR characteristics of (6,5)-SWNTs including inevitable nanotube defects and unintentional doping due to the surrounding atmosphere. In this context we will also investigate the nanotube matrix polymer PFO-BPy necessary to purifiy (6,5)-SWNTs. After the unintentional pre-doping of the first section we will then investigate deliberate chemical *p*-doping of (6,5)-SWNTs with $AuCl_3$ and determine the change induced on a single tube level. Finally, we will investigate the charge transfer (CT) properties of (6,5)-SWNTs with polymers and fullerenes for photophysical applications.

6.1 Materials and Properties

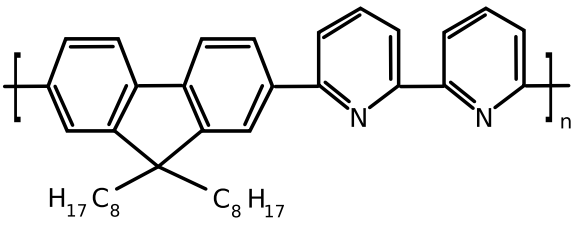

Figure 6.1: Structure of PFO-BPy [(9,9 − *dioctylfluorenyl* − 2,7 − *diyl*) − *alt-co* − (6,6′ − 2,2′ − *bipyridine*)].

PFO-BPy: For simplicity the chemically correct name [(9,9 − *dioctylfluorenyl* − 2,7 − *diyl*) − *alt-co* − (6,6′ − 2,2′ − *bipyridine*)] will be referred to as PFO-BPy in the following. It is a light yellow powder, absorbing at $\lambda_{Abs} = 361\ nm$ in Tetrahydrofuran(THF) solution and emitting in a violet regime $\lambda_{PL} = 411\ nm$ [74]. PFO-BPy is essential to separate (6,5)-nanotubes from other types of nanotubes, described in the following. It belongs to the group of hole transporting polymers.

(6,5)-SWNT: For general information about nanotubes the reader may refer to chapter 3.3. So far no distinct nanotube chiralities can be grown, despite tremendous advances in theoretical simulations elucidating the self-assembly processes of nanotubes and graphene [38]. Our measurements are solely performed with the "chiral" (6,5)-SWNTs, *prepared by Florian Späth and Florian Oberndorfer* from the group of Prof. Hertel, Physical and Theoretical Chemistry, Julius Maximilian University of Würzburg.

Generally, commercial nanotube mixtures one can buy contain a vast variety of different chiralities, from which the desired chirality needs to be extracted. To filter out (6,5)-SWNTs the polymer PFO-BPy, which exclusively wraps around nanotubes with (6,5)-chirality, and Toluene are added to the nanotube mixture. If this solution is then put into an ultrasonic ice bath, the nanotube mixture disentangles and a following ultra centrifugation step separates (6,5)-SWNTs from the rest. The whole preparation process is explained in detail in [124], and yields almost monochiral (6,5)-SWNT dispersions [125, 126]. Further, the polymer-sorted SWNTs exhibit very low residual metallic content and little intertube interactions [127], beneficial conditions to study doping on this material system as discussed in the next section. The tubes investigated in this work were prepared the same way as in [128], where the average nanotube length was measured to be L=1.82 μm with a standard deviation of σ_L=1.12 μm. Hence we assume these results to hold true for our samples. The high value of L is due to the usage of high speed shear force mixing instead of harsh sonication for selective dispersion. SWNT samples dispersed this way exhibit longer tube lengths than any technique involving sonication [129, 130, 131], as high-intensity sonication can shorten the nanotubes. Short SWNTs are unfavourable in the analysis of charge transfer and deliberate doping due to their higher density of tube edges and thus defects, as discussed in the following section.

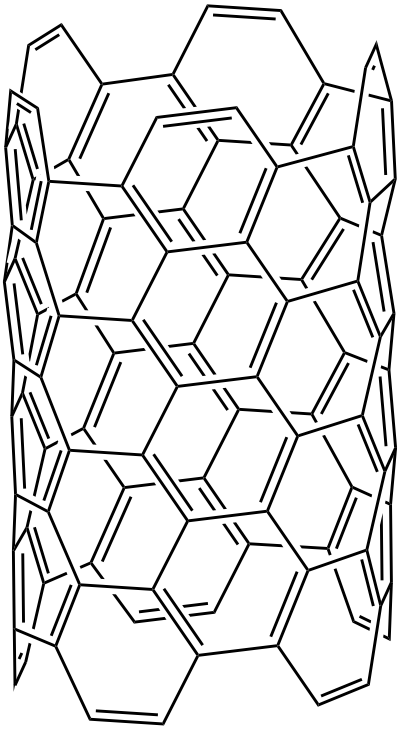

Figure 6.2: Structure of a semiconducting (6,5)-SWNT.

The density of states for (6,5)-SWNTs are shown in Figure 6.3a, *calculated by Friedrich Schöppler* [132]. They are based on a tight binding approach in a single particle picture, not including correlations between electrons or electrons and holes and are therefore of rather illustrative purpose. The tight binding approach includes a free parameter called γ_0, which has been chosen to match literature values of 1.55±0.05 eV for the energy gap of (6,5)-SWNTs in Tetrahydrofuran (THF) [133]. The corresponding absorption measurement of (6,5)-SWNTs is shown in Figure 6.3b, *measured by Florian Späth*. The discrepancy between a 1.55 eV bandgap and the S_1 absorption at 1.24 eV is a direct

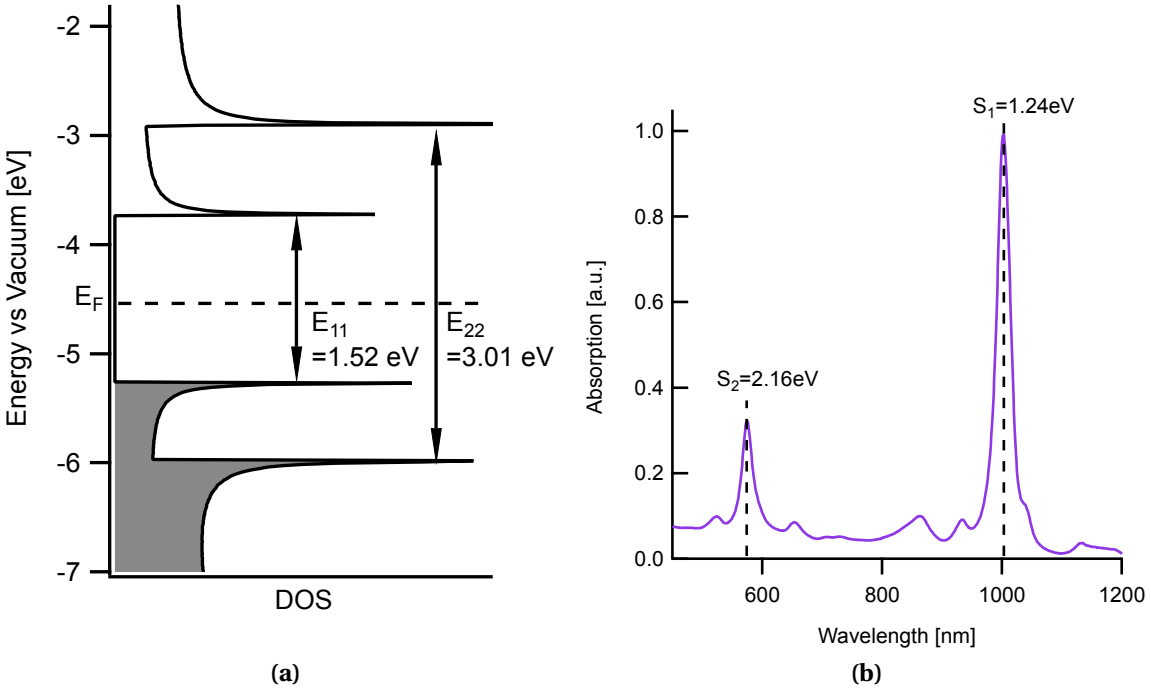

Figure 6.3: (a) Density of states for (6,5)-SWNTs via a simple tight binding approach from [132]. The bandgap of 1.55 eV in THF solution is well reproduced [133]. **(b)** Corresponding absorption spectra of the S_1 and S_2 absorption. The difference between the HOMO and LUMO level energies E_{11} and E_{22} and the S_1 and S_2 absorption can be explained with the approximately 300 meV exciton binding energy.

result of the ignored electron hole interactions. These result in a bound electron-hole pair around 300 meV lower in energy, corresponding to the exciton binding energy.

6.2 Quantification of SWNT Defects and Atmospheric *p*-Doping

In this section, we will investigate the unintentional pre-doping of nanotube mixtures and especially of (6,5)-SWNTs after the extraction process. Parts of this chapter are prepared for publication.

Introduction

Future photonic applications rely on long exciton lifetimes, requiring impurity concentrations that are as low as possible. However, excitons are quenched by either intentionally or unintentionally introduced defects or charge carriers [127, 134, 135, 136, 137, 133, 138, 139], among them being oxygen *p*-doping, resulting from the atmosphere [140], in situ oxygen from aqueous solutions [141], or the water/oxygen redox couple

[142, 143, 144], all of which have been found to be crucial. In low-dimensional semiconductors excess charges are often not freely moving but tend to be trapped. This can be rationalised by the enhanced Coulomb interaction with charged or polarisable particles in the semiconductor environment in low dimensions [145]. Thus, a profound understanding of carrier traps and their trap depth is mandatory. All-optical charge carrier generation in semiconducting SWNTs was found to lead to slow bimolecular recombination lifetimes of several 100 ps, which was attributed to electron and hole localisation [146, 147]. The extreme oxygen sensitivity of the nanotubes' electronic properties has been demonstrated by Collins et al. [140]. The increased electrical conductivity and thermoelectric power in air was attributed to adsorbed oxygen. The role of the oxygen/water redox couple in SWNT field-effect transistors has been studied by Aguirre et al. indicating oxidation depending on the pH level. [142]
Electron paramagnetic resonance is a method that is ideally suited to study defects, doping, charge localisation, and charge transfer in organic and inorganic semiconductors as it is sensitive only to unpaired electrons and allows for identification of the detected spin signatures' environment. In previous works employing EPR, rather raw carbon nanotube mixtures with different chiralities, i.e. also metallic, and double-walled SWNTs even containing residual catalyst were studied. Due to this initial situation the resulting signals couldn't be attributed free of doubt and thus are partially contradictory or inconclusive. Signals with g values reaching from g=2.00-2.07 are reported in literature for carbon nanotubes. By means of multi-frequency EPR on CVD grown SWNTs with various diameters, three overlapping signals at g=2.07 were found and attributed to itinerant spins because of their Pauli susceptibility and their rather large g-shift. An additional inhomogeneous signal at g=2.00 is attributed to defects of the carbon network of the tubes [148]. A g-tensor with the values: 2.0053, 2.0027, 2.0022 for chemically reduced SWNT buckypaper but no pristine SWNT signal [149], and a 4-fold EPR signal increase at around g≈2.0023 after oxygen removal were found [150]. SWNT mixtures containing metallic, semiconducting and also double-walled SWNTs of various chiralities were investigated by Zaka et al. [151]. They couldn't detect an EPR signal in pure SWNTs and attributed the g=2.0012 EPR signal of mixtures solely to catalyst residue. In one of the first EPR studies on pristine and purified (50-70 %SWNTs), and also additionally shortened nanotubes in 1998 by Chen et al. there was no EPR signal visible. For their nanotubes terminated with amide functionalities, i.e. semiconducting-SWNT-CONH$(CH_2)_{17}CH_3$ they found above 10^{-4} unpaired electrons per carbon atom but couldn't assign them to a specific origin [152]. To understand the processes causing undesired SWNT defects to be able to either avoid them in the future, or utilise the gained knowledge for deliberate doping, an elaborate EPR investigation is obliga-

tory. To elucidate the influence of carbon nanotube handling upon the present defects, including the contribution of oxygen and water, and determine what kind of defects these are we focus on EPR signals related to the initial raw CNT material and purified (6,5)-SWNTs.

6.2.1 Experimental Details

Material	Supplier
ComoCat (6,5)-SWNTs	SWeNT SG65i, Lot#MKBZ1159V (Southwest Nano Technologies Inc.)
PFO-BPy	American Dye Source
Acetonitrile	CHROMASOLV, for HPLC (Sigma Aldrich)
Toluene	Analytical reagent grade (Fischer Chemicals)
BDPA	No. 152560 (Sigma Aldrich)

Table 6.1: Here we present all raw materials used in this chapter and the according source of supply.

According to the supplier, the raw CoMoCat nanotube material contains about 95 % carbon, approximately 40 % (6,5)-SWNTs, 55 % other semiconducting SWNTs and 5 % unspecified non-carbon residue. For the first basic measurements, this material was simply dissolved in a 5:1 volume ratio of toluene and acetonitrile and put into an ultrasonic bath (USB) for 15 min. We also added PFO-BPy and put it into the USB for another 15 min to record reference spectra. The purified (6,5)-SWNT materials investigated in the following were prepared as briefly described in the previous section 6.1. The EPR samples were prepared as described in section 4.1.2.

BDPA

To perform quantitative EPR as mentioned in chapter 2.2.2 it is most convenient to use a spin reference sample. The air stable carbon-centered radical $1,3-$ *bis*(*diphenylene*)$-2-$ *phenylallyl* (BDPA), shown in Figure 6.4, is very similar to defects and localised spins in organic materials and therefore perfectly suited for our investigations. It is stabilised by it's propeller-like geometry sterically shielding the radical from potential reaction

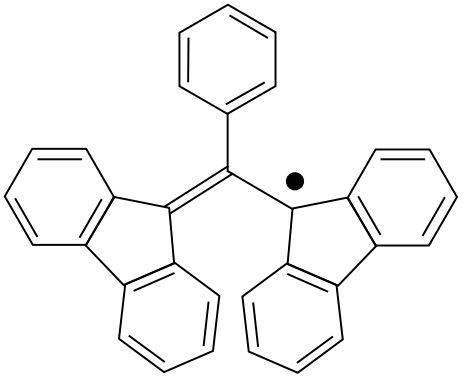

Figure 6.4: $1,3-$ *bis*(*diphenylene*) $-$ $2-$ *phenylallyl* (BDPA) structure used as a spin reference sample for quantitative EPR measurements.

partners [153, 154]. The unpaired electron is predominantly located at the 1- and 3-position of the allyl core and additionally stabilised by delocalization over the attached biphenyl ring systems [155]. The molar mass of the used 1:1 crystalline complex of BDPA with benzene (C33H21*C6H6) is 495.63 g/mol. By controlling the material amount in the reference sample, we can calculate the number of spins contributing to the EPR signal. BDPA is dissolved in benzene and the EPR sample is prepared as described in chapter 4.1.2. All reference samples contain (1.0±0.1)μg of BDPA. This corresponds to (1.22±0.12)·10^{15} molecules.

6.2.2 Raw and Purified Nanotubes

PFO-BPy

First of all the SWNT matrix polymer PFO-BPy was tested and seems to be inert under our measurement conditions. This is expected owing to its energy levels, resulting in an absorption below 400 nm discussed previously in chapter 6.1 and shown explicitly in chapter 6.4.1 Figure 6.21. Nevertheless, it does show a marginal peak at g=2.000 independent of illumination. It most probably origins from a tiny carbon radical residue as this g-factor is similar to an unpaired electron loosely bound to a carbon structure, which is also very close to the free electron's value. As this EPR signal is smaller then the overall signal noise it is negligible for further measurements. Please note, additional cross measurements of blends with the other materials used in this chapter have been carried out. They revealed that PFO-BPy is electrically inert and does not contribute to CT or doping, independent of temperature or illumination. Therefore, it won't be discussed in the following measurements.

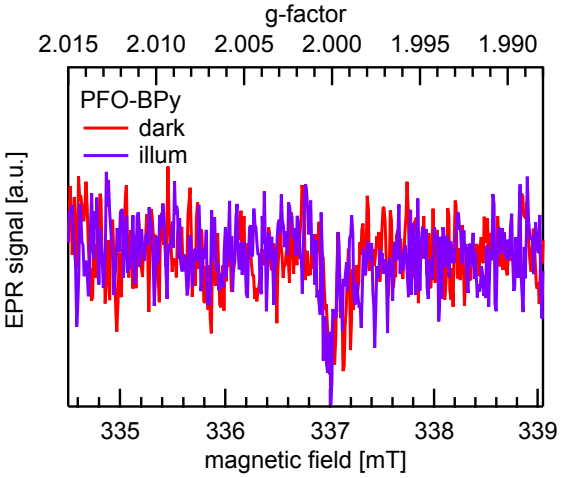

Figure 6.5: PFO-BPy EPR spectrum, the signal intensities are within the region of spectrometer noise and can be ignored in the following measurements.

Nanotube Handling and the Corresponding Defects

The raw nanotube material is commercially available CoMoCat SG65i from Sigma Aldrich. It contains about 95% carbon, approximately 40% (6,5)-SWNTs, 55% are other semiconducting carbon nanotube chiralities and 5% are unspecified non-carbon residue.

The raw material is dissolved in a 5:1 ratio by volume of toluene and acetonitrile with a concentration of 1.25 $^{mg}/_{ml}$. The EPR spectrum of this sample is shown in Figure 6.6a (dark green). In the next preparation step, the aforementioned matrix polymer PFO-BPy is added to the raw CoMoCat material and the resulting EPR spectrum is shown in Figure 6.6a (light green).

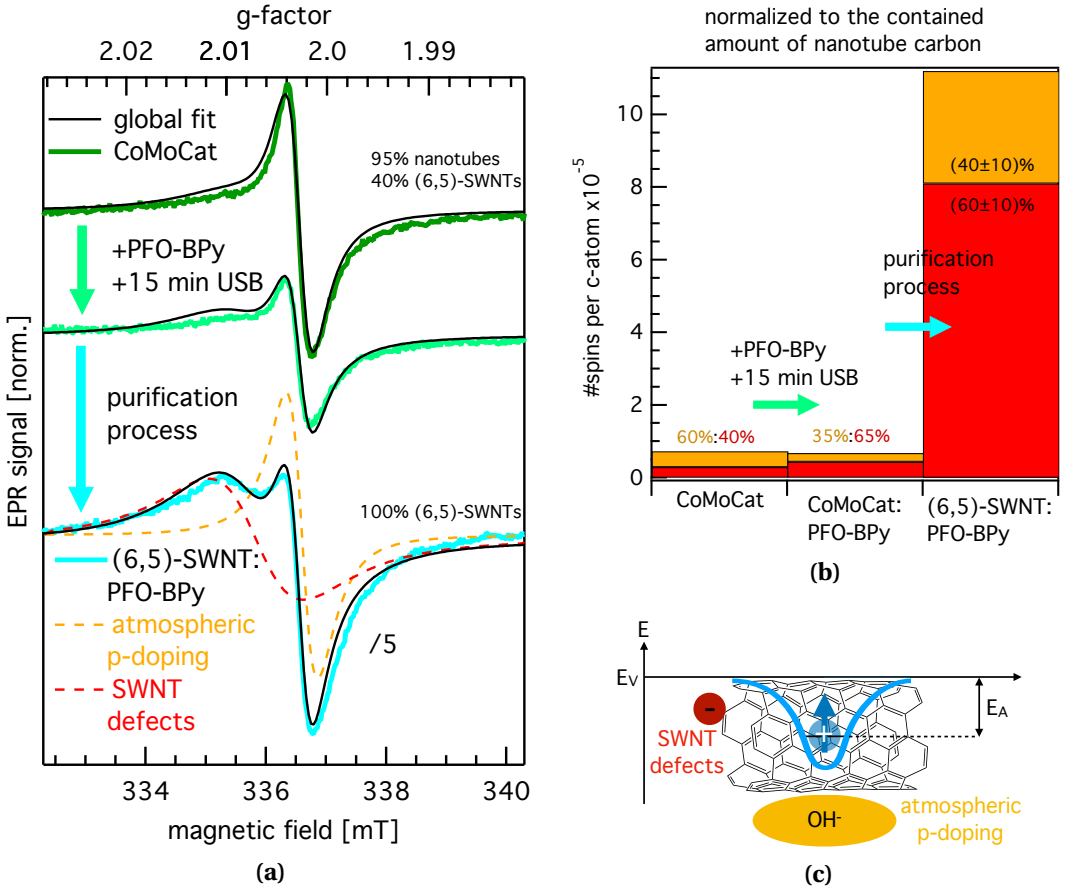

Figure 6.6: a) EPR spectra of the raw CoMoCat material (dark green) containing various SWNT chiralities, after adding the polymer PFO-BPy (light green) and a sample of purified (6,5)-SWNT:PFO-BPy (cyan). Intensities were normalised to the amount of nanotube carbon in the sample. A global fit as well as simulations via EasySpin to all three spectra (black) with two Lorentzian contributions were carried out. They are attributed to SWNT defects (red dashed) and atmospheric *p*-doping (orange dashed). **b)** Signal intensities of both contributions for all samples in **a)** normalized to the contained amount of nanotube carbon. Error margins for the purified (6,5)-SWNT:PFO:BPy are derived from samples with four different (6,5)-SWNT concentrations (see table 6.2). **c)** Schematic representation of a carbon nanotube with an overlaid potential of an adjacent counterion due to atmospheric *p*-doping (orange) of the nanotube, most probably OH^-. A dangling bond at the nanotube edge serves as an example for SWNT defects (red).

The EPR signal deviates only slightly from the raw CoMoCat sample, indicating no CT or doping processes are taking place upon interaction between PFO-BPy and the

nanotube mixture. The purification process follows previously reported procedures [133, 134], and employs the selective SWNT dispersion discovered by Nish et al. [156], and further enhanced for (6,5)-SWNTs by Ozawa et al. [125]. After the purification process, only (6,5)-SWNTs wrapped with the polymer are present in the solution. The corresponding EPR spectrum is more intense (intensity divided by 5 for better comparison) and slightly changes in shape as well, as shown in Figure 6.6a (cyan). A global fit (black) to the differently treated samples including taking different microwave powers into account (see Figure 6.7a for comparison) indicates two Lorentzian signal contributions shown in Figure 6.7b. Here, we tentatively assign them to SWNT defects (red dashed) and atmospheric *p*-doping (orange dashed). Their distinct EPR parameters were additionally determined by simulations carried out with EasySpin [20]. g-factor and linewidth peak-to-peak (lwpp) are g=2.0069±0.0003, lwpp=0.70 mT and g=2.0024±0.0003, lwpp=0.26 mT for SWNT defects and atmospheric *p*-doping, respectively. In the following, their sum is referred to as SWNT EPR background signal.

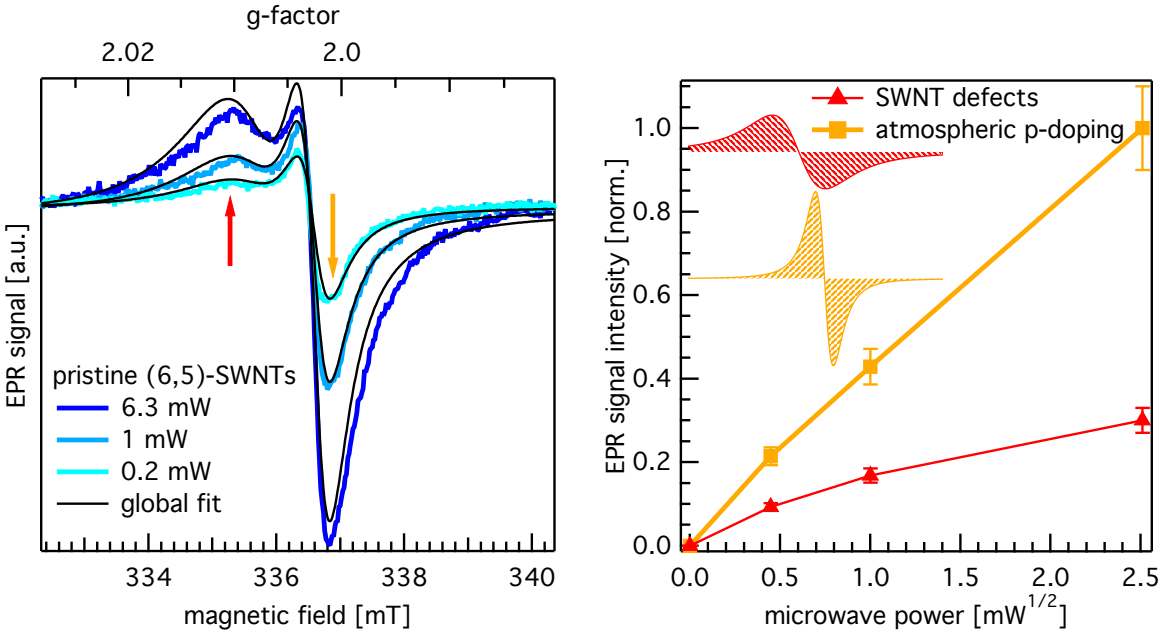

(a) Cavity **(b)** PFO-BPy

Figure 6.7: (a) EPR spectra of a pristine (6,5)-SWNT:PFO-BPy sample (267μg/ml) at various microwave powers together with a global fit consisting of two Lorentzian contributions (black). The different dependences of the peak amplitudes with respect to the microwave power are indicated by a red and orange arrow. **(b)** The double integrals, i.e. EPR signal intensities, of the two global fit contributions from **(a)** are plotted versus the square root of the microwave power. The two different slopes represent different saturation behaviours caused by the samples' T2 spin-spin relaxation times clearly yielding two superimposing signals (see chapter 2.2.1 for comparison). The inset schematically depicts the two disentangled EPR spectra.

Discussion

The quantified EPR signal intensities of all samples with a unit of "number of spins per C-atom" are presented in Figure 6.6b. For the CoMoCat material a concentration of approximately $(0.73\pm0.15)\cdot10^{-5}$ spins per carbon atom is observed, of which approximately 60% is atmospheric *p*-doping and 40% CNT defects. Then the polymer PFO-BPy is added, involving one ultrasonication step to facilitate dispersion. The total number of spins does not change, however the intensities of the two contributions differ. The signal that we tentatively attributed to atmospheric *p*-doping is reduced by almost half to now 35% of the total spin number. Meanwhile, the second signal for SWNT defects increases considerably to 65%. The purification process to remove all CNT chiralities except the (6,5)-SWNTs increases the total number of EPR-detectable species by more than a factor of ten to $(11.1\pm2.6)\cdot10^{-5}$ spins per carbon. These numbers are averaged for samples with four different (6,5)-SWNT concentrations in between 49 and 267 μg/ml (see table 6.2 for comparison).

SWNT sample concentration / $\cdot10^{-5}$ spins per carbon atom	49 $\mu g/ml$	143 $\mu g/ml$	243 $\mu g/ml$	267 $\mu g/ml$
SWNT defects	6.9±1.8	4.7±1.3	4.3±1.0	9.5±2.1
atmospheric *p*-doping	6.5±1.4	4.4±1.0	3.7±0.8	4.0±0.8
total spins	13.4±3.2	9.1±2.3	8.0±1.8	13.5±2.9

Table 6.2: Spin numbers of the reference samples used to calculate the pristine (6,5)-SWNT values given in Figure 6.6b.

Both signal contributions increase by spin number after the purification process. Considering the number of 88 carbon atoms per nm (6,5)-SWNT, we get (5.6±1.4) SWNT defects and (4.1±0.9) atmospheric *p*-doping spins per μm nanotube. For the used purification procedure [128], the average SWNT length is approximately 1.82 μm which would result in 8-13 SWNT defects and around 6-9 spins of atmospheric *p*-doping per nanotube. Altogether this background quantification revealed low impurity (6,5)-SWNTs as the result of the purification process.

We interpret these findings along the following reasoning to justify our assignment of both signal contributions. First, we can assess that both signals do in fact originate from SWNTs, as the EPR signals of the solvents and the PFO-BPy polymer are miniscule in comparison. The total number of radicals in PFO-BPy is independent of sonication and is below $0.2\cdot10^{-5}$ spins per carbon of the polymer. In the hereby used concentrations it would merge with the background noise. Second, it is known that ultrasonication of carbon nanotubes causes shorter average tube lengths by breaking tubes

and thus increases defects, i.e. the total number of defects [157, 128]. Therefore, the stepwise increase of one of the two signal contributions for subsequent sample treatments agrees with an expected increase in inflicted defects and nanotube shortening. Likely candidates are the unsaturated dangling bonds (radicals) at edges of SWNTs as depicted in Figure 6.6c. They are also responsible for similar EPR signals (g-factor and linewidth) in soot and other forms of amorphous carbon. Unsaturated dangling bonds of radical character at SWNT edges are also likely candidates for observed fluorescence quenching at the nanotube ends [127, 158]. Third, the narrow signal is almost identical (g-factor and linewidth) to previously reported oxygen-induced *p*-doping signals for charge transfer complexes between molecular oxygen (O_2) and conjugated polythiophenes [159]. In that case molecular oxygen is loosely adsorbed onto the polymer backbone leading to charge transfer from the polymer. This is comparable to the interaction between SWNTs and adsorbed water-oxygen redox couples most probably yielding OH^- counterions as schematically depicted in Figure 6.6c as a carbon nanotube with a nearby counter charge causing *p*-doping on the nanotube. This signal contribution decreases by half upon addition of PFO-BPy to CoMoCat and ultrasonication. This process of displacing adsorbents by wrapping polymers around the nanotube is again indicative of our assignment. How the oxygen complex might be formed was investigated by Moonoosawmy and Kruse [141]. They investigated the doping effects of acids as well as the in situ formation of molecular oxygen in aqueous solutions of HiPco SWNTs. The oxidation of SWNTs with respect to the solutions' pH values has been investigated by Aguirre et al., showing oxidation for a sufficiently low pH [142]. The (6,5)-SWNT's valence band is calculated and experimentally determined by Hirana et al. to lie at around -(5.05±0.1) eV [160]. This value varies in literature with the level of completeness for the energy level determination of the underlying graphene layer in the cutting lines approach, reaching from Hückel to high level DFT approaches. The concept of cutting lines for SWNTs is discussed in chapter 3.3. Depending on the pH value, pH 6 lies at around -5.1 eV, electrons can be drawn from the nanotubes resulting in *p*-doping. As the pH value for our acetonitrile:toluene solution is undefined we assume it to be sufficiently low to enable *p*-doping.

6.3 Quantification of $AuCl_3$ Induced *p*-Doping

In this section, we will investigate the intriguing processes happening in a (6,5)-SWNT doped with $AuCl_3$. Parts of this chapter are prepared for publication.

Introduction

Precise control over doping of semiconductors, providing mobile charge carriers, or even tailoring the transition from metal to insulator is essential for their application in electronic devices. Therefore, detailed knowledge about the doping process and the resulting free carrier concentration is necessary. As an example, the performance of semiconducting single-wall carbon nanotube (s-SWNT) based technology is claimed to be extremely critical on the doping level. Thermoelectric devices were found to possess the largest power factors at high carrier concentrations achieved by redox-chemical doping [161, 162]. For s-SWNTs redox chemically *p*-doped with $AuCl_3$, photoluminescence imaging [163], as well as changes in the exciton dynamics and energetics [134], suggest that charge carriers are localized due to Coulomb interaction with counterions adsorbed at the SWNT surface [164]. The oxidation of approximately 50% (6,5)-chirality enriched carbon nanotubes, purified and separated from CoMoCat and HiPco base material, was thoroughly investigated by Zheng and Diner [144]. There, the bleaching of the CNT absorption could be observed via UV/vis/NIR spectroscopy attributed to the oxidation of the nanotubes by oxygen. Various SWNT mixtures prepared by different methods have been investigated for charge separation in P3HT:SWNT blends by Niklas et al. where no reduced SWNT EPR signal could be found [149]. Only SWCNT buckypaper, chemically reduced with hydrazine, showed an EPR signal with g values: 2.0053, 2.0027, 2.0022. Rice et al. observed the 4-fold increase of EPR signal intensity after oxygen removal in their acid-purified laser oven nanotubes [150]. Due to their cobalt- and nickel-containing samples the reason for that phenomenon remains unanswered. Nevertheless, tremendous impact of the doping level on the nanotube properties is remarkable and needs clarification.

This work is the first to study highly purified (6,5)-SWNTs with long nanotube length and without catalyst residue. We carefully separate (6,5)-SWNTs from commercially available raw semiconducting-SWNT mixtures, employing modern purification protocols. Here, we use EPR spectroscopy to distinguish, identify and quantify chemically induced *p*-doping in semiconducting (6,5)-SWNTs via the redox active substance $AuCl_3$ from unintentional atmospheric *p*-doping and spin-carrying SWNT defects, discussed in chapter 6.2.2.

6.3.1 Experimental Details

The materials used in this chapter have been purchased according to table 6.3 and will be described in detail in the following.

Material	Supplier
$AuCl_3$	trace metal basis (Sigma Aldrich)
Acetonitrile	CHROMASOLV, for HPLC (Sigma Aldrich)
Toluene	Analytical reagent grade (Fischer Chemicals)
BDPA	No. 152560 (Sigma Aldrich)
Au nanoparticles (⌀5 nm)	Lot#MKCD3137 (Sigma Aldrich)

Table 6.3: Here we present all raw materials used in this chapter and the according source of supply.

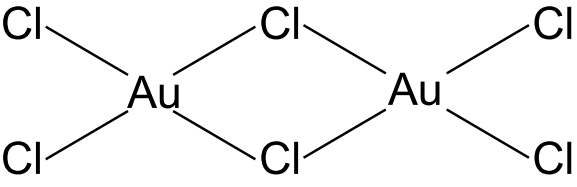

Figure 6.8: $[AuCl_3]_2$ salt used to *p*-dope (6,5)-SWNTs. The $AuCl_3$ redox potential is assumed to be more than 0.75 eV below the highest occupied (6,5)-SWNT valence band, depending on the oxidation state [165].

$AuCl_3$: Gold(III)-chloride is a frequently studied material known to induce chemical *p*-doping in Carbon Nanotubes [166, 165, 164, 163]. In its ground state it exists as a chloride-bridged dimer $[AuCl_3]_2$ as shown in Figure 6.8 and has a molar mass of 303.325 g/mol. $AuCl_3$ oxidizes SWNTs and leads to adsorption of counterions on their sidewalls [167]. The monomer $AuCl_3$ has a spatial extent of 0.85 nm, adsorbing to the SWNT in an approximate center to center distance of about 0.7 nm without and 1.5nm with the polymer present [134]. It does not dissolve in non-polar solvents like toluene. Thus a solvent combination of toluene and acetonitrile with a volume ratio of 5:1 was used to blend it with the (6,5)-SWNTs, as acetonitrile is a polar solvent that dissolves a wide range of ionic and non-polar compounds.

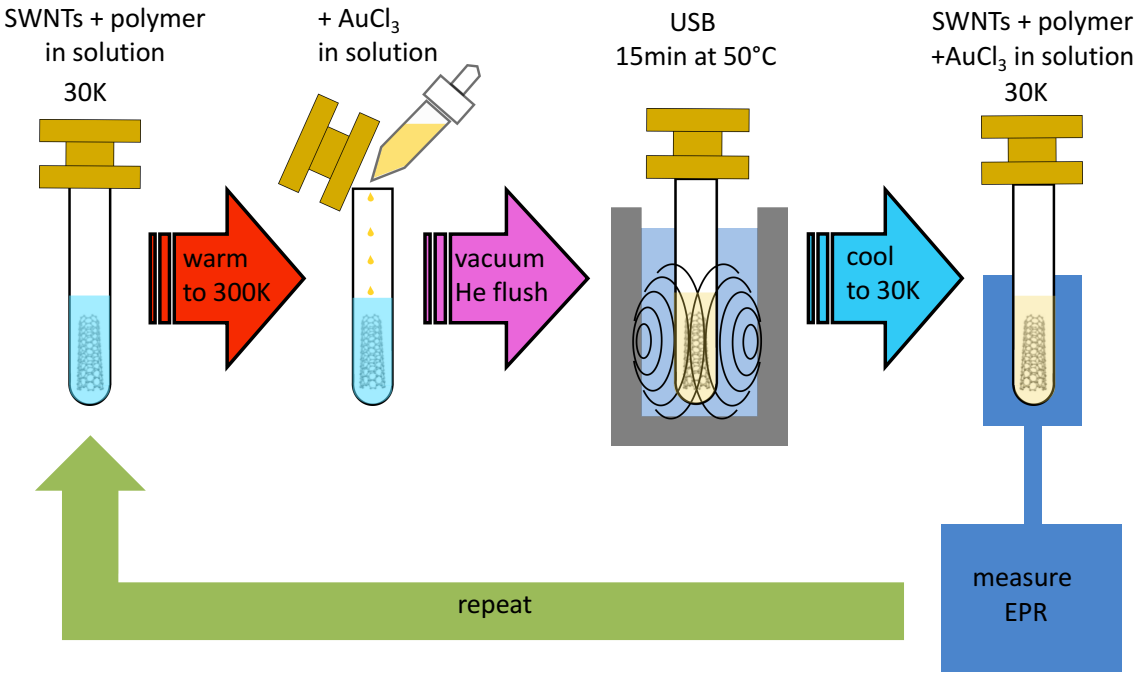

Figure 6.9: Doping cycle for (6,5)-SWNT:PFO-BPy samples in solution. $AuCl_3$ solution is added to the nanotube:polymer solution. After flushing with helium, the sample is put in an ultra-sonic bath (USB). Subsequently it is put in an EPR spectrometer where doping is quantified at 30 K.

Adsorbed $AuCl_3$ on the nanotube surface leads to charge transfer due to favourable redox potentials. This is put into practice by stepwise addition of $AuCl_3$ solution to the SWNT solution (toluene:acetonitrile in a 5:1 volume ratio). The process of chemical *p*-doping induced by $AuCl_3$ involves three steps, as proposed by Kim et al. [164], resulting in Cl−, $AuCl_2^-$ and $AuCl_4^-$ as possible counter ions. The cycle to step wise dope our samples in the experiment is depicted schematically in Figure 6.9. First, $AuCl_3$ dopant is added to the (6,5)-SWNT:PFO-BPy solution. Afterwards, the sample is carefully vacuum pumped and flushed with helium several times to remove remaining air without evaporating solvent. To support the chemical doping process and reverse SWNT agglomeration due to the electrostatic interactions in already doped solutions, the sample is sonicated for 15 min at 50°C. After sonication, the sample is inserted into the EPR setup and cooled down to 30 K for spin quantification. For the next doping cycle, the sample is carefully warmed to 300 K and the process is repeated.

For visualisation we did add an exemplary photo series for our sample with 243 $\mu g/ml$ (6,5)-SWNT shown in Figure 6.10. Thereby the amount of $AuCl_3$ is increased step wise

for five times. One can clearly see the change in colour of the solution transitioning from bright purple to dark purple and gold. This is simply caused by the additional yellow absorption of the $AuCl_3$. The demixing of the solution occurs after doping step 1, and increases in the following steps due to the increasing electrostatic interactions for increasing doping.

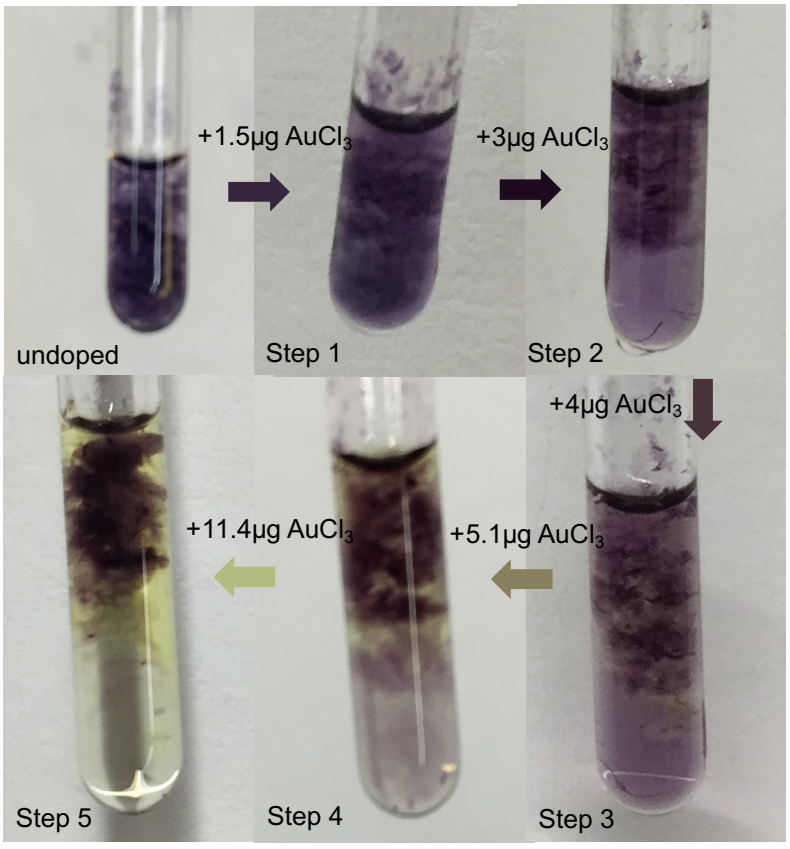

Figure 6.10: Pictures of a 4 mm diameter EPR tube containing 243 $\mu g/ml$ (6,5)-SWNT doped with different amounts of $AuCl_3$, increasing from step 1 to step 5. The increasing electrostatic interactions cause the demixing visible after doping step 1.

All doping runs investigated in this work are shown in table 6.4. The concentration of the nanotube solution without any $AuCl_3$ added is given in the most left row as SWNT starting concentration. In the beginning we always had 50 μL SWNT solution in our EPR tube and then added 10 μL $AuCl_3$ solution in every step. The resulting $AuCl_3$ concentrations are given in the corresponding lines.

SWNT [$\mu g/\mu L$] \ $AuCl_3$ [$\mu g/\mu L$]	1	2	3	4	5	6	7	8	9
53	15	26	34	40	45	66	102	132	161
86	20	40	60	151	245				
143	16	43	100	144	230				
243	25	64	106	151	256				
267	6	12	25	50					

Table 6.4: Overview over all doping measurement runs vertically sorted by the SWNT starting concentrations. We started with 50 μL SWNT solution and stepwise added 10 μL $AuCl_3$ to get the $AuCl_3$ concentrations given in the corresponding line.

6.3.2 Reference Measurements

To exclude any potentially interfering signal we measured the background signal of the spectrometer loaded with an EPR tube filled with helium. No signal contribution from the spectrometer or the EPR tube, i.e. quartzglas could be detected. No significant EPR signal intensities were detectable for Acetonitrile, Toluene, $AuCl_3$ and Au nanoparticles (5 nm diameter) within the relevant g-factor range for SWNT doping reaching from g=1.98 to g=2.03.

Gold

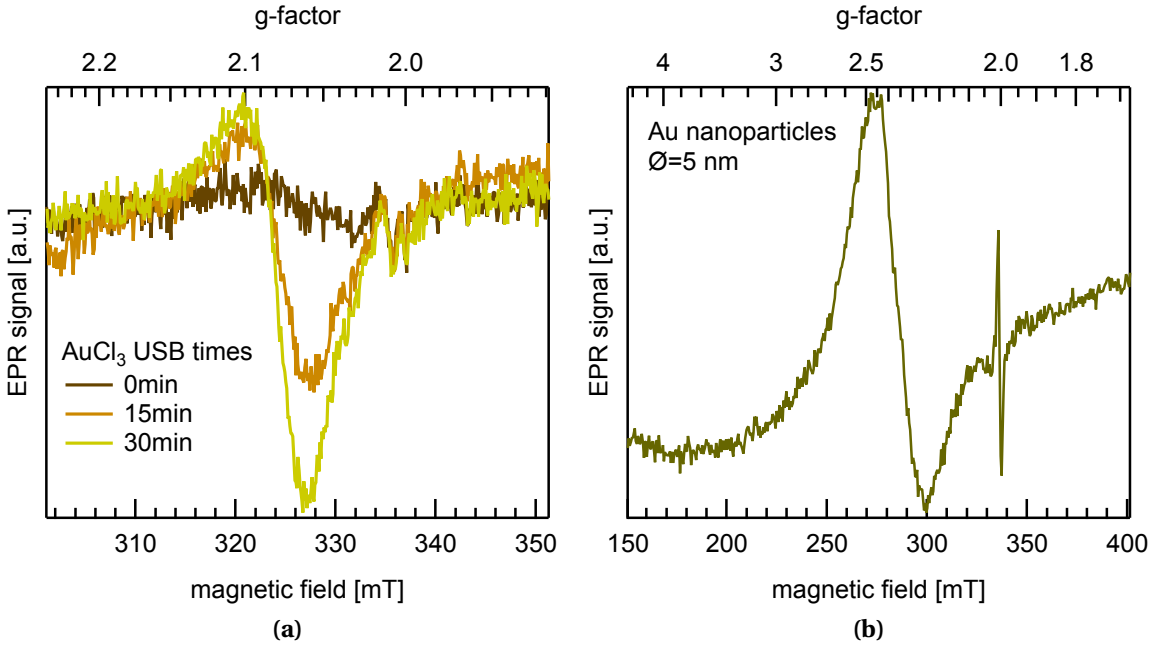

Figure 6.11: EPR spectra measured at 30K, 2mW microwave power and a strong magnetic field modulation (0.04 mT) of **(a)** $AuCl_3$ with 250 $\mu g/ml$ concentration and **(b)** a few mg Au nanoparticles with 5nm diameter.

Nevertheless, we have found a wide gold EPR signature, shown in Figure 6.11a reaching from g=2.0 to further than g=2.2 which is evidence for a strong spin orbit coupling as common in heavy atoms. As only even number oxidation states of gold carry an unpaired spin we assume Au to be in such a state, most probably Au(II). A four-fold hyperfine splitting of the EPR signal due to coupling to the 197 Au nuclear spin of I=3/2 could not be seen, which would be a direct prove for a mononuclear Au(II) complex [168]. The observed signal can only be seen for solutions with very high $AuCl_3$ concentrations above 200 μg/ml. For comparison we add the signal of Au nanoparticles ($\oslash$ 5 nm) reaching from g=2.1 as far as g=3.0, again typical for spins in systems with heavy particles i.e. strong spin orbit coupling. Despite the fact that they are not identical, we can assume both to have spins delocalised over Au. Here it should be noted, that $AuCl_3$ as well as the Au nanoparticles were measured with 2 mW microwave power and 0.04 mT magnetic field modulation to get a decent signal to noise ratio. These values are 10 and two times as high as what is used for the SWNT doping measurements, respectively. Thus, their signal contributions are not relevant for the following measurements, i.e. are below signal noise in the relevant g-factor region.

Verifying Curie's Law

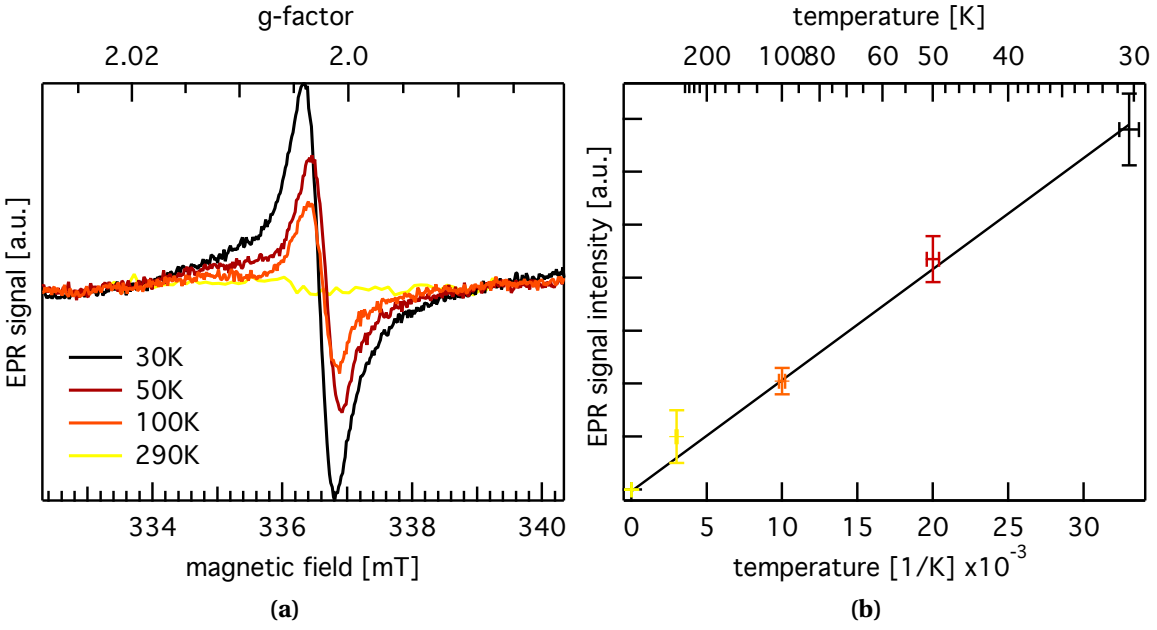

Figure 6.12: (a) EPR spectra for highly doped (6,5)-SWNTs at various temperatures. **(b)** Double integral of the EPR spectra clearly yielding a reciprocal temperature dependency following Curie's law.

To verify a paramagnetic species as source of an EPR signal we investigate it's intensity versus temperature relation shown in Figure 6.12a. The linear dependency of the $AuCl_3$ doped SWNTs' EPR signal intensity versus the reciprocal temperature is shown in Figure 6.12b. This dependency is expected and predicted by Curie's law for paramagnetic species. For maximum signal intensity and best signal to noise ratio we chose 30 K sample temperature for most of our measurements.

Influence of Sonication Time Upon Doping Stability

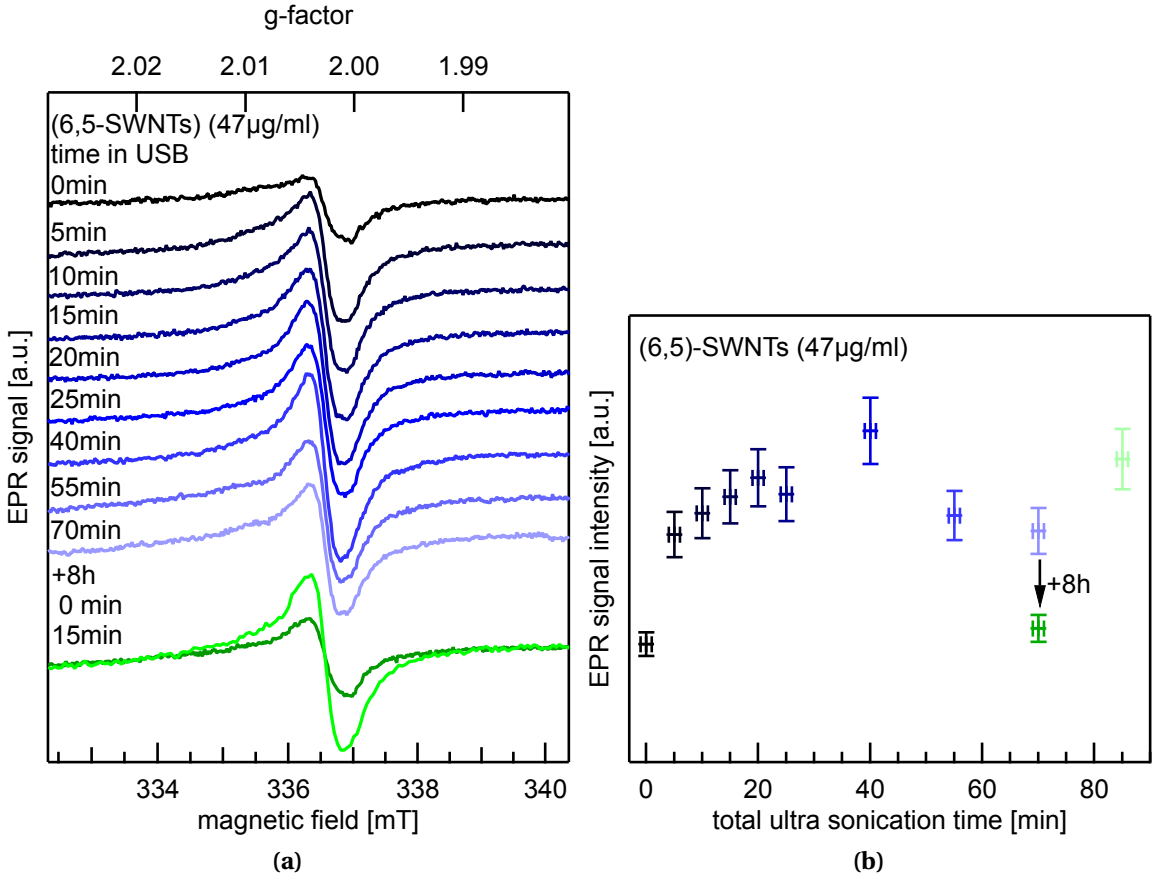

Figure 6.13: **(a)** EPR signal of a (6,5)-SWNT:PFO-BPy (47 μg/ml) sample for extended sonication time in an ultra-sonic bath (USB) after $AuCl_3$ addition (22 μg/ml). Spectra are shifted for better discernibility. **(b)** Peak to peak intensity, i.e. EPR signal intensity of **(a)** vs. the total sonication time.

To investigate the influence of ultra-sonication time on doping stability, a SWNT sample (47 μg/ml) was doped with 22 μg/ml $AuCl_3$ and EPR measurements were taken after various ultra-sonication times as shown in Figure 6.13a. The sample was treated identically to the doping cycle as explained above, without adding more dopant. I.e. between every measurement the sample was warmed up to room temperature, put in-

side the ultra-sonic bath (USB) for a specific time and then again cooled down to 30 K inside the EPR spectrometer. The observed signal shape does not change upon sonication, thus the intensity is directly proportional to the peak to peak intensity, plotted versus the total time spent in the USB in Figure 6.13b. Directly after $AuCl_3$ addition, the sample already shows a strong doping signal even before ultra-sonication. This indicates good intermixing of the two solutions. For 15 up to 55 min of total USB time a slightly increasing, but relatively stable signal intensity can be observed. After a combined 70 min of ultra-sonication the sample was left for 8 hours at ambient temperature before taking the next spectrum. The signal decreases considerably, potentially due to nanotube agglomeration that expels the dopant, or radical reactions. Nevertheless, this effect can be fully reversed by another 15 min in the USB indicating agglomeration as cause of the effect. We conclude that extended ultra-sonication and repeated freezing and thawing of the samples has no influence on the doping process itself and that 15 min USB are a sufficient time period for the following experiments.

6.3.3 Varying Dopant Concentrations

Now that we attributed the origin of the EPR signatures for purified, polymer-wrapped (6,5)-SWNTs we can focus on signals for deliberately induced doping. We present experimental data of samples with low and high SWNT concentrations first before discussing a lattice model describing the SWNT doping process and reproducing the data's curve progression.

Low SWNT Concentrations

Figure 6.14a shows one set of EPR spectra for a low SWNT concentration of 86 μg/ml. Quantitatively similar results were obtained for a sample with 53 μg/ml. Generally, the observed signals and their changes in intensity are qualitatively identical for all studied samples. The purified (6,5)-SWNT signal (cyan) represents the background doping consisting of SWNT defects and atmospheric *p*-doping. It can be fitted using the same contributions of SWNT defects and atmospheric *p*-doping as discussed in section 6.2.2 (black line). The EPR signal significantly increases for the $AuCl_3$ concentration of 20 $\mu g/ml$ (bright blue) and 40 $\mu g/ml$ (dark blue) in the solution, indicating the strong doping effect of $AuCl_3$ on (6,5)-SWNTs. The contribution for the doping induced signal (black dashed) has also been added. For further addition of $AuCl_3$ the signal intriguingly saturates at 60 $\mu g/ml$ (dark purple) and then decreases for stronger doping of 151 to 245 $\mu g/ml$ (magenta), which will be discussed in the following.

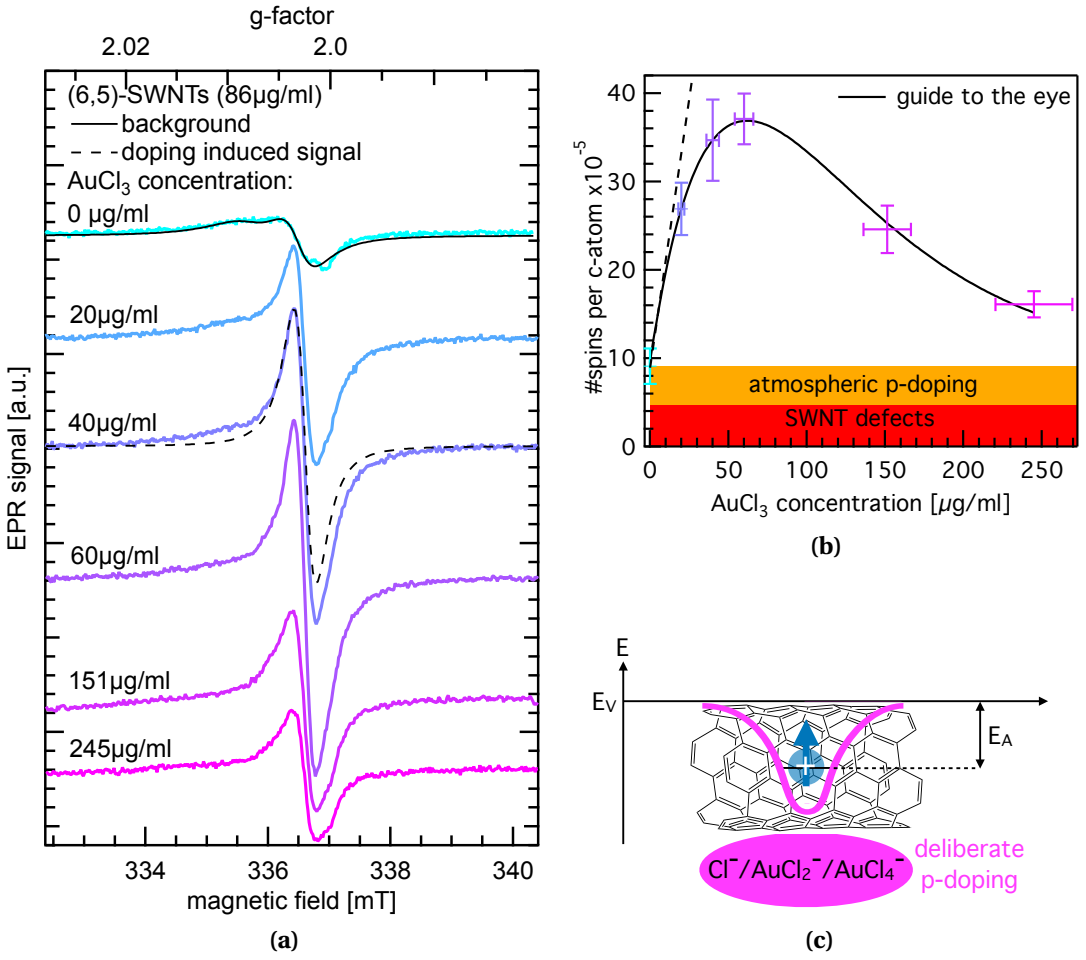

Figure 6.14: Doping of purified (6,5)-SWNT:PFO-BPy solution. **(a)** EPR spectra for a purified sample (cyan) and for increasing $AuCl_3$ dopant additions (blue to magenta). The signals can be fitted using the same background (black line) of SWNT defects and atmospheric *p*-doping as discussed in section 6.2.2, and an additional contribution for the doping induced signal (black dashed). **(b)** Number of EPR active spins per C-atom for increasing $AuCl_3$ doping in addition to the background. Added $AuCl_3$ causes first a linear signal increase (black dashed) followed by an exponential decay (black fit). **(c)** Schematic representation of a carbon nanotube with an overlaid potential of an adjacent Cl^-, $AuCl_2^-$ or $AuCl_4^-$ due to deliberate $AuCl_3$ *p*-doping of the nanotube [164].

Discussion

The EPR signals of atmospheric *p*-doping (g = 2.00235±0.00010) and $AuCl_3$ induced *p*-doping (g = 2.00284±0.00010) are almost identical and reveal only a very slight shift of the line position (g-factor), consistent over all measurements performed. This g-factor difference indicates the slightly different environment for the localised charge on the SWNT being adjacent to either an OH^-, or an Cl^-, $AuCl_2^-$ or $AuCl_4^-$ anion [164], as shown in Figure 6.14c. When both contributions are present at the same time,

they are completely superimposed and indistinguishable by means of X-Band EPR. It should be noted that the oxygen trap depth after ozone exposure was estimated to be 61 meV by Ghosh et al. [169], while the $AuCl_3$ induced trap depth supposedly lies at around 100 meV [134]. Hence adsorption of $AuCl_3$ might be energetically favourable over oxygen-doping and counterions are less localised for the shallower atmospheric *p*-doping. Therefore, the doping yield might actually be underestimated later on due to replacement of the OH^- by Cl^-, $AuCl_2{}^-$ or $AuCl_4{}^-$. The contribution of SWNT defects remains mostly unchanged until very high $AuCl_3$ doping and can thus be subtracted in the following quantitative analysis.

The number of detectable induced spins per C-atom vs. concentration of $AuCl_3$ in the solution for the spectra in Figure 6.14a is given in Figure 6.14b. The background contribution from SWNT defects (red) and atmospheric *p*-doping (orange) is also shown for comparison. On top of the background signal, added $AuCl_3$ causes first a linear signal increase for small dopant concentrations. A fit to the data gives a linear doping yield of about (1.5±0.2)% $^{spins}/_{AuCl_3}$. As we expect the reaction between dopant and SWNTs to be incomplete (leftover $AuCl_3$ stays in solution), we assume this value to be a lower limit for the doping yield. For further doping the EPR signal subsequently decreases again and almost vanishes for large $AuCl_3$ concentrations. The transition from localised, unpaired and thus EPR active spins on (6,5)-SWNTs to paired EPR silent biradicals can be narrowed down to roughly 30 spins per μm SWNT discussed in the following. There are two effects that we ascribe to the observed doping curve and the fitted guide to the eye in Figure 6.14.

First: Formation of diamagnetic biradicals starting at moderate dopant concentrations. As discussed before for the linear doping regime, every single added $AuCl_3$ dopant leads with a certain yield to a localised spin on the SWNT. However, at a higher density of localised charges interactions do occur. The dopant induces a shallow potential well of about 100 meV that is occupied by a single positive charge at low concentrations. Considering this energetic attraction and spin selection rules, it is reasonable to expect pairwise occupation of such a potential well. The two spins pair in an energetically favourable singlet configuration; i.e. a diamagnetic biradical or biradicaloid (see [170] for reference) with total spin S = 0. This configuration is EPR silent and does not add to the doping spin count [171, 172]. Hints on triplets, i.e. total spin S=1 state signatures could not be observed in full- or half field EPR measurements. The signal maximum roughly marks the situation where all additionally induced charge carriers on the nanotube form biradicals and result in an exponential signal decay. Almost the same spin pairing effect yielding EPR silent bipolarons on polypyrrole has been reported by De-

vreux [173]. It results in a quite similar correlation between the number of spins and charges on pyrrole.

Second: A degenerate regime for excessive doping. When SWNTs are doped excessively, the EPR signal vanishes completely. Likewise, the S1 absorption is completely quenched as shown most recently by Eckstein et al. and others [134, 169, 133, 174]. Both are best described with an overlap of the carrier wave functions causing a degenerate density of states at high doping concentrations schematically shown in the next chapter in Figure 6.16a. Quite similar results could be seen for P3HT doped with BCF [175].

A comprehensive model based on the previously discussed effects is elaborately presented in Figure 6.16 in the next chapter. Together with optical measurements it perfectly reproduces our experimental data as shown in Figure 6.17. Our lattice model yields charge carrier sizes of d=(3.5±1) nm perfectly consistent with optical measurement by Eckstein et al. [134] discussed in the next chapter. But before, we need to take a look on samples with higher nanotube concentrations.

High SWNT Concentrations

Besides the aforementioned measurement, we also investigated doping in samples with higher (6,5)-SWNT concentrations. To get a better visual representation of the whole process and take account of the ratio of SWNTs to $AuCl_3$ dopants, we calculated the amount of $AuCl_3$ per μm SWNT from the total weight ratio of $AuCl_3$ to SWNT, i.e. dopant to base, shown on the lower axis. Furthermore, we determine the number of induced spins per μm SWNT by normalising the total number of spins to the contained SWNT amount in our solutions while considering that every nm (6,5)-SWNT is made of 88 C-atoms. These normalisations are necessary to compare different measurement runs with different nanotube and $AuCl_3$ concentrations. In the following we will discuss the differences observed regarding the nanotube concentrations in the samples. The 53 and 86 $\mu g/ml$ samples did behave identically, discussed in detail in the previous section. If we increase the SWNT concentration to 143 $\mu g/ml$ we observe a strong decrease of the curve for the induced spins per μm. This trend continues for the sample with 243 $\mu g/ml$ and 267 $\mu g/ml$ (not shown). With respect to the previously discussed effects, this indicates that the deliberately induced charge carriers start interacting at much lower charge carrier densities, resulting in EPR silent states. A reason for observing these lower densities might be a virtual effect caused by agglomeration, yielding bunches of nanotubes which are only doped on the outmost layer. General solubility measurements of single-walled carbon nanotubes indicate that this might indeed be the reason for the observed phenomenon [176, 177]. The SWNT solubility in toluene

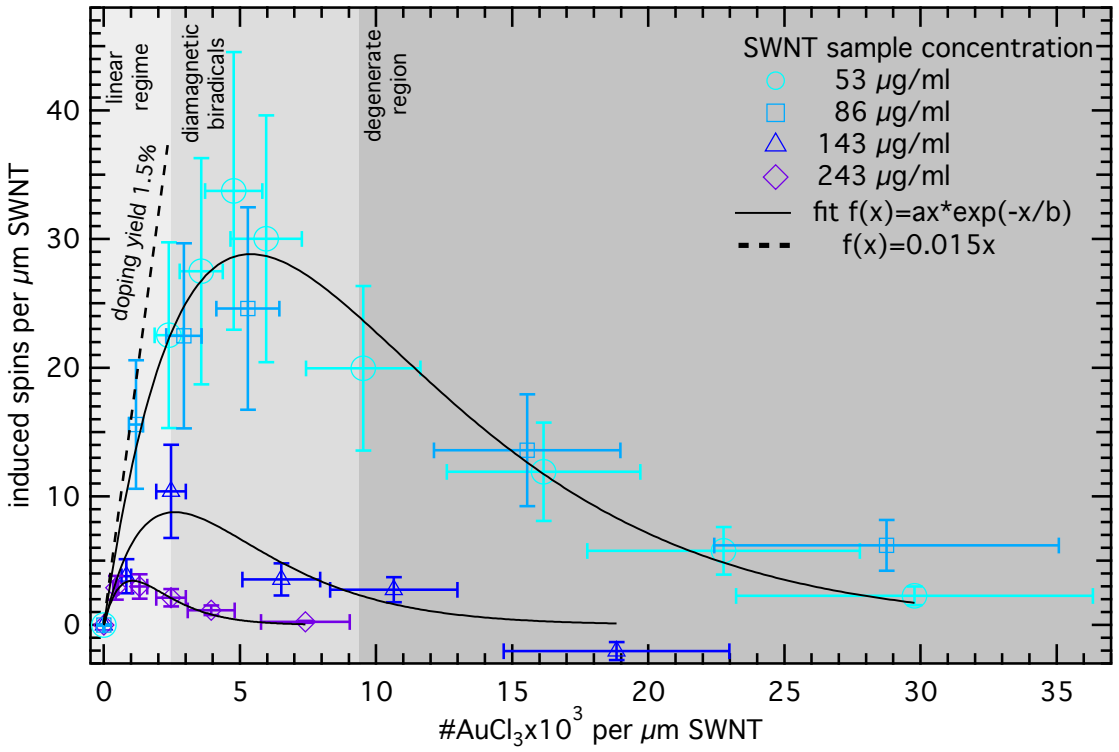

Figure 6.15: Number of EPR active spins per μm SWNT for increasing $AuCl_3$ dopant addition. Axes are calculated as described in the text. In addition to the amount of atmospheric *p*-doping and SWNT defects, added $AuCl_3$ firstly causes a linear signal increase with a slope of (1.5±0.2) % (black dashed). Multiplication with an exponential decay results in the black slope perfectly following the data. Samples with 53 (cyan) and 86 (bright blue) $\mu g/ml$ SWNT concentration are almost identical. For higher concentrations of 143 (dark blue) and 243 (purple) $\mu g/ml$ the curve decreases on the whole, probably caused by agglomeration.

was even investigated theoretically, but sadly only for (10,10)-SWNTs [178]. Due to the fact that we have a 5:1 ratio of toluene and acetonitrile and monochiral (6,5)-SWNTs wrapped with PFO-BPy, the solubility threshold needs to be extracted from experiments focused especially on our experimental situation, being beyond the scope of this work. Nevertheless, we observed hints on agglomeration while investigating the influence of the time spent in the USB upon the EPR signal. They yield a signal decay after letting the solution settle for a few hours, shown in Figure 6.13b in chapter 6.3.2. As an $AuCl_3$ monomer is around 0.85 nm in size it might be hindered from penetrating dense SWNT networks as long as they are consistently wrapped with PFO-BPy (see chapter 6.3.1 and 6.1 for comparison). This seems reasonable, as the PFO-BPy chain measures only 0.5 nm in width due to its benzene and pyridine rings, leaving the C_8H_17 side chains aside. In dilute solution where the polymer chain is randomly distributed the SWNTs should be separated by a few nm. Nevertheless, if the SWNTs

align parallel with the PFO-BPy polymers laying flat upon their surface, dense agglomerates could form which can only be doped on their surface. Simple mass-to-surface estimations assuming ball-like agglomerates yield that this effect could indeed explain the decreasing overall spin densities for increasing SWNT concentrations.

6.3.4 Combining EPR and Optics

To establish a model that considers the aforementioned formation of biradicals or biradicaloids to describe the amount of EPR active species, we need to know the number of deliberately induced charge carriers on the nanotube. Obviously, this value is impossible to determine via EPR. Nevertheless, this problem can be solved by Optical measurements. The SWNT absorption was *measured by Florian Oberndorfer and Klaus Eckstein*. We will explain the model first before combining optical and EPR data.

The Model

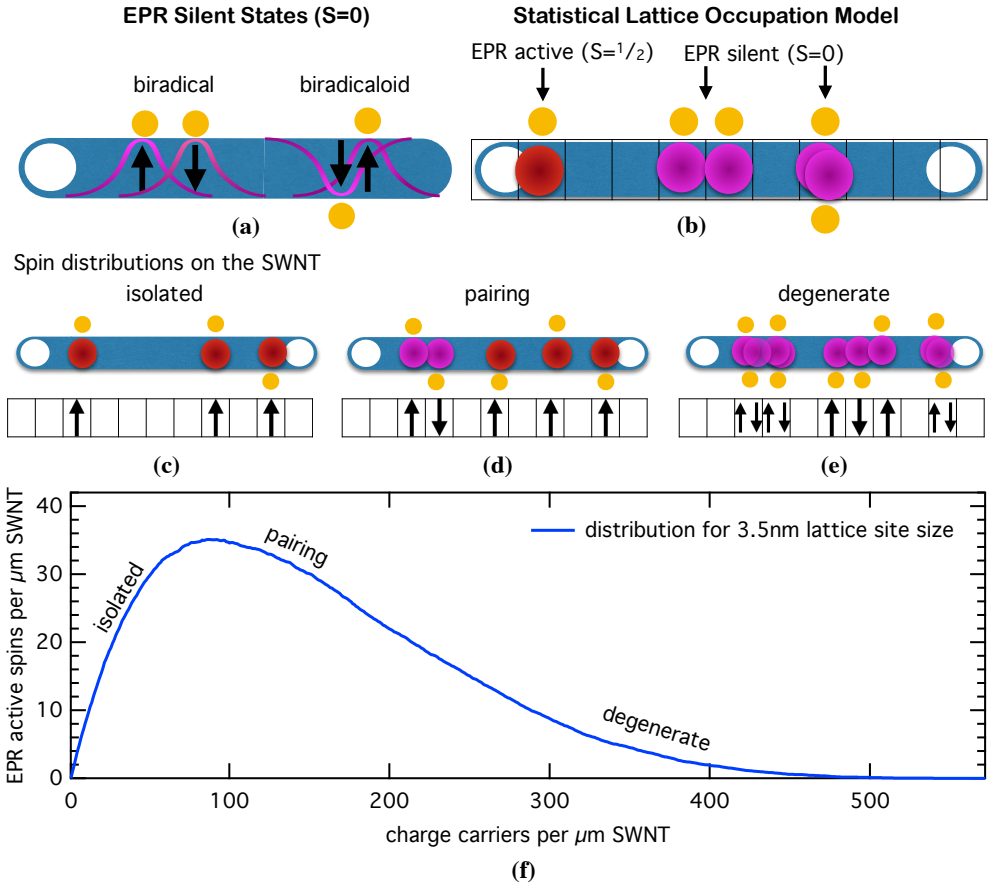

Figure 6.16: **(a)** Two neighbouring singly occupied (S=½, EPR active) lattice sites on a nanotube can form a biradical (S=0, EPR silent) or a biradicaloid, a double occupied lattice site (S=0, EPR silent) if they are within a specific distance. **(b)** Shows the nanotube lattice occupation model considering isolated (red) and pairing (magenta) states depicted in **(a)**. **(c)**, **(d)**, and **(e)** illustrate the doping process of the nanotube's lattice sites reaching from isolated EPR active charges to pairing of charges, to degenerate and EPR silent states, respectively. **(f)** The resulting curve of the discussed statistical lattice occupation model is shown for a lattice site size of 3 nm (blue).

Two neighbouring spin carrying particles (S=½, EPR active) on a nanotube can form a biradical (S=0, EPR silent) if they are close enough, what may also result in a biradicaloid (S=0, EPR silent), both shown in Figure 6.16a. This simple nanotube lattice occupation model is shown in Figure 6.16b considering the states in (a). The lattice sites are uniform but variable in size and can be occupied with one EPR active (red) or two spin carrying particles forming an EPR silent biradicaloid (magenta). The later also counts for two neighbouring sites (magenta). The whole doping process of the nanotube's lattice sites is shown in three exemplary steps with increasing dopant concentrations, starting with single isolated EPR active charges in Figure 6.16c to pairing of charges in (d), to degenerate and EPR silent states in (e). Afterwards, the formation of biradicals and biradicaloids dominates and causes a decrease in EPR active lattice sites. A degenerate (EPR silent), metallic like state of the nanotube is reached after (e) until all lattice sites are double occupied. This metallic like behaviour is explained by a shift of the Fermi level into the valence band, causing carriers to become delocalised. The resulting data curve for the lattice site size of (3.5±1) nm is shown in Figure 6.16f (blue), resulting in 286 sites per μm SWNT we can fill with 572 charges. From (f) we can deduce a maximum amount of around 40 of the lattice sites to be unpaired and EPR active. The previously discussed model is shown implemented in Python code below. Please note that Python is indent sensitive so check carefully before running the script.

```
import csv
import matplotlib.pyplot as plt
import random
from random import randint

def generate_data_set(n,z):#n=number of sites,
    #z=number of averages
    sites_list=[]
    #list of our nanotube lattice sites
    spins_list=[]
    #number of isolated spins per number of charges placed
    avgspins_list=[]
    #list of the averaged runs for the isolated spins

    for i in range(n):
        sites_list.append(0)#list of length of n
    for i in range(2*n):
        spins_list.append(0)#list of length 2n
        avgspins_list.append(0.0)
```

```
        #integer list of the averaged runs
        #for the isolated spins with length 2n

    m=0
    while m <= z:
        avgspins_list=[avgspins_list[i]+
        spins_list[i] for i in range(2*n)]
        #we add spins_list to avgspins_list
        for i in range(2*n):
            spins_list[i]=0
            #need to reset the list entries to 0 after every run
        for i in range(n):
            sites_list[i]=0
            #need to reset the site entries to 0 after every run

        i=0
        while i < 2*(n-1):#repeat the following till all
                #n sites are doubly occupied
                a = randint(0,n-1)#picks a random lattice site
                #between 0<=N<=n-1
                if sites_list[a]==0:#empty lattice site
                    sites_list[a]=1
                    #occupy the picked lattice site
                    i+=1
                elif sites_list[a]==1:#if it is singly occupied
                    sites_list[a]=2#double occupy it
                    i+=1
                else:
                    i=i
                s=0
                #don't consider spin numbers from previous runs
                k=1
                #needs to be reseted
                while k < (n-1):
                #check all 2n sites in the sites_list
                    if sites_list[k-1]==0 and sites_list[k]==1
                    and sites_list[k+1]==0:
                        s+=1#count the number of isolated spins
                        k+=1#and check the next site
                    else:
```

```
                        s=s#in all other cases there's
                        #no isolated spin to count
                        k+=1#check the next site
                spins_list[i]=s#count the number of spins in
                #this i-th round and write it into the list
        m+=1
    avgspins_list[:]=[x/z for x in avgspins_list]
    #normalize to number of iterations
    print avgspins_list
    plt.plot(avgspins_list)
    plt.ylabel('isolated spins per mum SWNT')
    plt.xlabel('#charges per mum SWNT')
    plt.show()
    with open("spins.csv", "w") as outfile:
        #write a csv file with the spin numbers
        csvwriter = csv.writer(outfile, lineterminator='\n')
        for value in avgspins_list:
            csvwriter.writerow([value])

generate_data_set(333,100)
#333 sites correspond to a lattice site size of 3nm
```

Conclusively, the observed EPR intensity curve in Figure 6.15 can qualitatively be well described with our simple nanotube lattice occupation model as shown in Figure 6.16f. Nevertheless, both x-axes are not equivalent, as the number of charge carriers per nanotube can not be determined via EPR. Thus, we will now combine our EPR data with already published optical measurements of the (6,5)-SWNTs S1 absorption shift by Eckstein et al. [134], yielding the charge carrier densities on the nanotubes.

Charge Carriers Versus EPR Active Spins

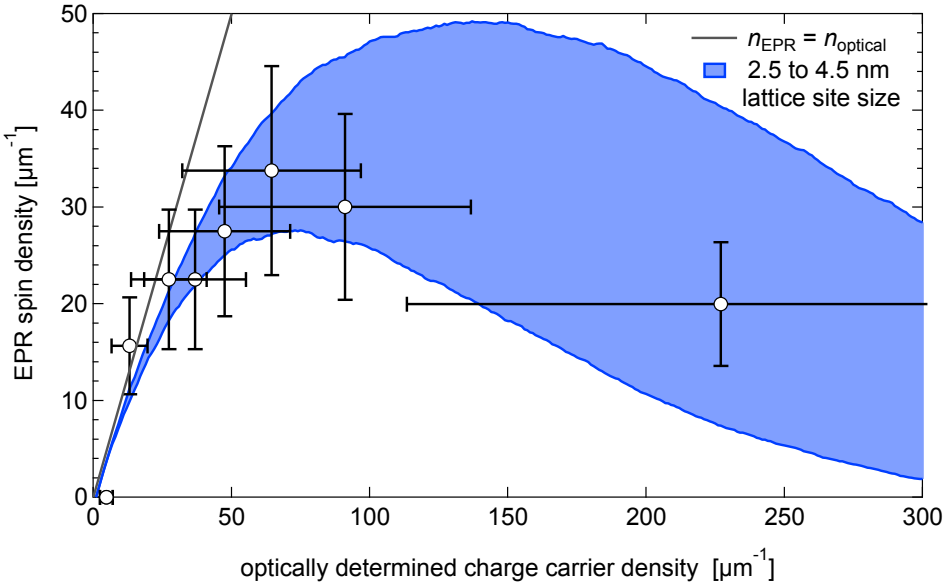

Figure 6.17: The perfect correlation of directly determined spin densities via EPR and indirectly determined carrier densities via absorption measurements, the later is already published [134], is shown for low doping concentrations, i.e. 53 $\mu g/ml$ and 86 $\mu g/ml$. A straight line (black line) where the number of optically determine charge carriers ($n_{optical}$) is equal to the number of EPR active spins (n_{EPR}) is added for comparison. The deviation at higher densities is well described with the lattice occupation model for a lattice site size of (3.5±1) nm (blue).

Convincingly, the directly determined EPR spin densities for our low SWNT concentration samples (53 and 86 $\mu g/ml$) can be correlated with indirectly determined carrier densities from the shift of the nanotube's S1 absorption peak. The absorption measurements have already been published by Eckstein et al. [134]. Both approaches do yield the same results (black circles) for low doping concentrations and are shown together in Figure 6.17. Sadly, the error in the optical measurements is too large for higher charge carrier densities, i.e. above 200 charge carriers per μm, to yield meaningful results. Thus, more reliable results were obtained for the lower charge carrier densities. The outstanding correlation is well described with the aforementioned lattice occupation model for a lattice site size of (3.5±1) nm (blue) explaining the deviation from a straight line (black line).

6.3.5 Summary

For raw semiconducting as well as for purified, undoped (6,5)-SWNT samples, very low signal intensities are observed, stemming from two separate, radical-like spin con-

tributions. One can be attributed to SWNT defects being introduced by the purification process of mixed-chirality CoMoCat material to separate the (6,5)-SWNTs. This contribution may be caused by the shortening of the SWNT which results in defects, such as non-saturated dangling bonds. The second contribution can be associated with what is commonly referred to as intrinsic *p*-doping due to the interaction with the water-oxygen redox couple [169, 141]. Nevertheless, their concentration indicates high nanotube quality. Considering the average length of the tested (6,5)-SWNTs of around 1.82 μm [128], a single-digit number for both paramagnetic species on each SWNT can be estimated, while one μm SWNT corresponds to 88.000 C-atoms. For deliberate $AuCl_3$ doping at low doping concentrations, the charges are mainly isolated and randomly distributed over the SWNTs, suggesting that all carriers are localised in Coulomb traps. This minor doping causes not only a linear increase of detected spin carrying species, but also a correlated quenching and shift of the SWNT's optical S1 absorption [134]. At moderate to high doping concentrations, charges start interacting, enabling the formation of EPR silent diamagnetic biradicals and biradicaloids, i.e. no further increase but rather a decrease in EPR signal intensity can be observed. Above approximately 100 spins per μm nanotube the Fermi level is shifted into the valence band and carriers become delocalised. Hence, the EPR signal, as well as optical S1 absorption vanishes. A lattice model of the doping process suggests that (3.5±1) nm charge spacing is the critical distance for biradical formation.

The bunching process of carbon nanotubes at high nanotube concentrations has to be investigated to determine the underlying interaction of nanotube, polymer and solvent. We could not detect an EPR signal related to an Au complex. To determine what happens to the $AuCl_3$ salt after the doping process, i.e. metallic gold Au(0) or an Au(II) complex formation, it might be necessary to filtrate the solvent from the nanotubes and separate the rest by centrifugation. In conclusion, we can confirm charge carrier confinement at low impurity concentrations in SWNTs with potentially far-reaching implications for future device applications in the area of semiconductor technology.

6.4 Carbon Nanotube Charge Transfer

Currently, the application of carbon nanotubes in already existing devices is vastly investigated to boost the device performance of supercapacitors [179], catalysts [180], terahertz devices [181], and many others [182]. As their extraordinary electronic properties promise improvement concerning optical absorption, charge carrier separation and transport, they are preferably added to photovoltaic devices [183, 184, 185, 186, 187]. In this context, the following chapter will focus especially on the process of charge transfer (CT).

To investigate the contribution of carbon nanotube CT in organic photovoltaics (OPV), it is wise to start with a well known OPV system. Therefore, we blend purified (6,5)-single-wall carbon nanotubes (SWNTs) with either the conjugated polymer P3HT or the fullerene derivative $PC_{60}BM$, both together are a well known benchmark system for OPV. Parts of the following measurements were taken during my time as master student. At first, we will take a look at the materials and their absorption spectra. Additionally, the highest occupied molecular orbitals (HOMOs) and lowest unoccupied molecular orbitals (LUMOs) are shown to illustrate the possible CT interactions after excitation. The light sources used for charge carrier generation are listed as well. To deduce if charges are transferred and separated between the distinct materials electron paramagnetic resonance (EPR) is the method of choice, as this measurement method allows for the determination of the electrons' and holes' environments. The in the following observed (6,5)-SWNT signal of unintentional doping is discussed in chapter 6.2. As we will see, the matrix polymer PFO-BPy, which is necessary to purify (6,5)-SWNTs, is electronically inert under the investigated conditions.

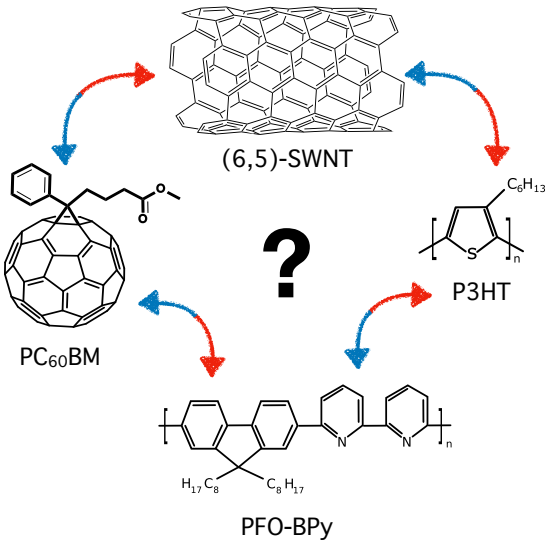

Figure 6.18: Who interacts with whom?

6.4.1 Experimental Details

Materials

Material	Supplier
P3HT >99.995 %	regioregular, Lot#MKBX1586V (Sigma Aldrich)
$PC_{60}BM$ >99.5 %	(Solenne b. v.)
Chlorobenzene >99.8 %	Anhydrous, Lot#STBH6215 (Sigma Aldrich)

Table 6.5: Here we present materials used in this chapter and the according source of supply. (6,5)-SWNTs in PFO-BPy were prepared as discussed previously in section 6.1.

An overview of the materials used in this chapter are given in table 6.5. The (6,5)-SWNT and its matrix polymer PFO-BPy have been described previously in section 6.1.

P3HT: For simplicity the chemically correct name *Poly*(3 – *hexylthiophene* – 2,5 – *diyl*) will be referred to as P3HT in the following, firstly synthesised in this regioregular head to tail structure by Chen et al. [188]. It is a dark brown powder, with an absorption maximum at $\lambda_{Abs} = 445\ nm$ and a photoluminescence at $\lambda_{PL} = 567\ nm$ in Tetrahydrofuran (THF) solution and $\lambda_{PL} = 644\ nm$ in film [74]. Depending on the solvent the HOMO and LUMO are at around -5 eV to -5.2 eV and -3 eV to -3.2 eV, respectively [108, 75]. It is a hole transporting polymer.

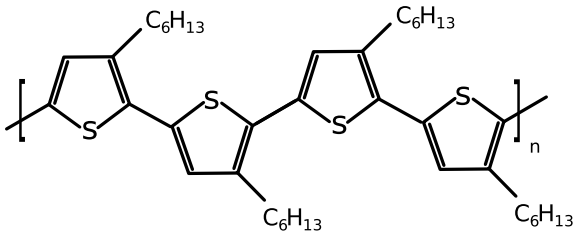

Figure 6.19: Structure of P3HT *Poly*(3 – *hexylthiophene* – 2,5 – *diyl*) (P3HT)

$PC_{60}BM$: The fullerenes chemically correct name is [6,6] – *Phenyl* – *C*61 – *butyric* – *acid* – *methyl-ester*. The main part consists of the C_{60} buckyball. The fullerenes earned their name due to their architectural similarity to structures from the canadian architect Buckminster Fuller [12]. The HOMO and LUMO levels of $PC_{60}BM$ are between -6.0 eV to -5.9 eV and -4.3 eV to -3.7 eV (for comparison see chapter 5.2.1).

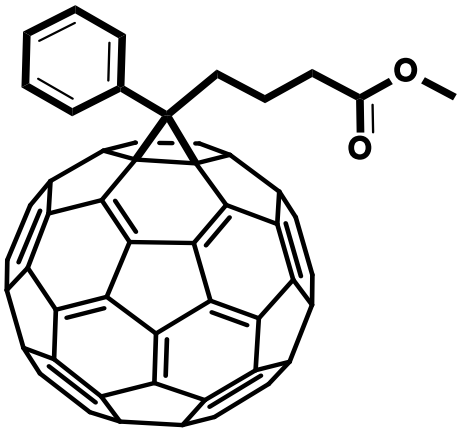

Figure 6.20: Structure of [6,6] – *Phenyl* – *C*61 – *butyric-acid* – *methyl-ester* ($PC_{60}BM$).

Sample Preparation

As organic materials are generally very reactive with oxygen the sample preparation should take place in a preferably oxygen free environment. Nevertheless, often the materials and especially the solvents are already contaminated with oxygen. Hence, reducing this oxygen contamination is also crucial to gain high sample stability. Otherwise, chemical reactions might occur under illumination degrading our samples, i.e. changing the EPR signatures. Therefore, all samples were prepared under nitrogen atmosphere inside a glovebox. The compounds were dissolved and diluted in chlorobenzene separately. Afterwards, they were mixed and shaken to speed up intermixture and then poured into EPR tubes. To minimise air contact the EPR tubes are closed with plastic caps inside the glovebox before taken out. After removing the plastic cap outside the glovebox, the tubes are immediately connected to a vacuum pump, flushed five times with helium and sealed off between (0.2 to 20) mbar helium atmosphere.

Sample	1	2	3	4	5	6	7	8	9	10	11	12	13	14
PFO-BPy [μg]	4000	4000	4000	2000	2000	20	20	20	20	20		20		
SWNT [μg]	4	4	4			4	4	4						
$PC_{60}BM$ [μg]	160			160		16			16		80			2000
P3HT [μg]		40					16			16			80	2000
Solution in *chloro-benzene* in [μL]	240	240	200	240	200	240	240	200	240	240	200	200	200	200

Table 6.6: Samples 1-5 are made with the first, 6-14 with the second (6,5)-SWNT batch from *Florian Späth*. For each sample the mass contribution of the individual components is given, as well as the total amount of solution in *chlorobenzene* poured into the corresponding EPR tube.

We received two different nanotube batches from *Florian Späth*, differing only in their PFO-BPy concentration of $10^{mg/mL}$ and $0.1^{mg/mL}$ for the first- and second batch, respectively. The mass contribution of the individual compounds in the blends are given in table (6.6), together with the total amount of solution in *chlorbenzene* poured into the corresponding EPR tube. The PFO-BPy concentrations didn't influence the signal intensity. The nanotube concentration was calculated from carbon concentration, determined via the (6,5)-SWNT's S1-absorption in solution. Literature gives an S1-absorption cross section error of around 24 % [189], yielding nanotube concentrations of $(20.4 \pm 4.8)^{mg/L}$ for both batches. We also received pure PFO-BPy powder for reference measurements.

Absorption Spectra

The materials absorption spectra are shown qualitatively in Figure 6.21, normalised to their maximum absorption peak in the observed region from 350 nm to 1250 nm. (6,5)-SWNT:PFO-BPy (purple) was measured in solution by *Florian Späth*, showing a steep absorption edge below 400 nm, due to the PFO-BPy bandgap of E_{gap} ≈3 eV. The other two peaks are the characteristic (6,5)-SWNT exciton transitions S1 at 989 nm and S2 at 575 nm. Note that the exciton binding energy is somewhere in the few hundred meV region [190, 191].

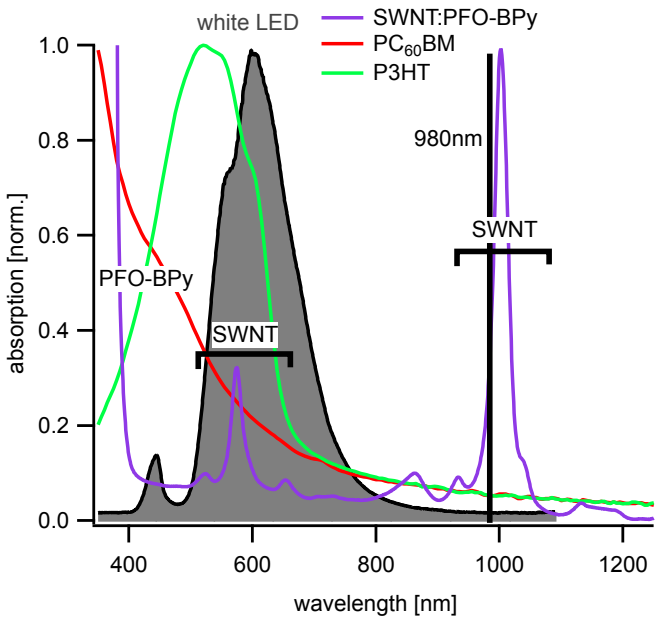

Figure 6.21: Normalised absorption spectra of (6,5)-SWNT:PFO-BPy (purple) measured by *Florian Späth*, P3HT (green) and $PC_{60}BM$ (red), together with the white LED emission spectrum (purple) measured by *Hannes Kraus*.

P3HT (red) and $PC_{60}BM$ (green) were measured in thin films. We also added the white LED's emission spectrum (purple) measured by *Hannes Kraus*, and the used laser light at 980 nm. The illumination powers were determined experimentally to avoid oversaturation and amount to approximately 50 mW for the 980 nm laser. In the case of the white LED, around 0.5 W are transmitted into the cavity. Most importantly, the 980 nm laser only excites (6,5)-SWNTs, whereas the white LED excites all materials.

Energy Levels

The following schemes illustrate the HOMOs and LUMOs for (6,5)-SWNT together with $PC_{60}BM$ or P3HT, shown in Figure 6.22 and 6.23, respectively. For further information on orbital energies see chapter 3 and 5.2.1 . Due to the high density and the corresponding overlap of the orbitals, the values for (6,5)-SWNT orbitals rather correspond to a valence and conduction band gap than specific energy levels [192, 193]. Possible CT processes are indicated with black arrows.

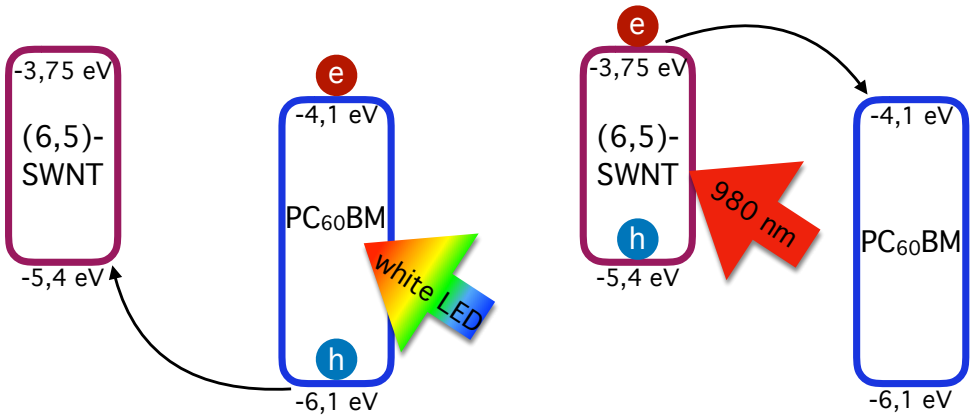

Figure 6.22: HOMO and LUMO levels of (6,5)-SWNT and $PC_{60}BM$ under white LED and 980 nm laser light excitation.

First, we will focus on (6,5)-SWNT and $PC_{60}BM$, shown schematically in Figure 6.22. From the absorption measurements in Figure 6.21 we conclude that the white LED mainly excites $PC_{60}BM$. In this case we expect hole transfer from $PC_{60}BM$ to (6,5)-SWNT, as it is energetically favourable. This CT would result in electrons on $PC_{60}BMs$ and holes on (6,5)-SWNTs. On the other hand, we would expect electron transfer from (6,5)-SWNT to $PC_{60}BM$ under 980 nm laser light illumination, as this wavelength exclusively excites (6,5)-SWNTs. This case also leads to electrons on $PC_{60}BMs$ and holes on (6,5)-SWNTs.

Let us now focus on (6,5)-SWNT and P3HT, schematically shown in Figure 6.23. In the case of P3HT and (6,5)-SWNT the CT situation is less clear. The bandgap of P3HT is larger than for a (6,5)-SWNT. From an energetic point of view it is unclear what to expect with white LED illumination, as both CT processes from P3HT to (6,5)-SWNT might yield lower energy states. The relative positions of the HOMO and LUMO levels indicate a minor energy gain for holes and a big energy gain for electrons to hop from P3HT to (6,5)-SWNT. Therefore, it might be possible that most of the optically generated charge carriers on P3HT are transferred to the nanotubes, where they can recombine on a ps timescale. In the case of 980 nm laser light excitation we exclusively excite (6,5)-SWNTs. Here we can already see the band like structure of (6,5)-SWNT. The energy levels reveal a bandgap of 1.5 eV, whereas 980 nm correspond to 1.27 eV, exciting the S1 exciton transition (an approximately 300 meV bound e-h pair). Due to the band like structure a hole transfer from (6,5)-SWNT to P3HT might be possible resulting in electrons on (6,5)-SWNT and holes on P3HT. An electron transfer from (6,5)-SWNT to

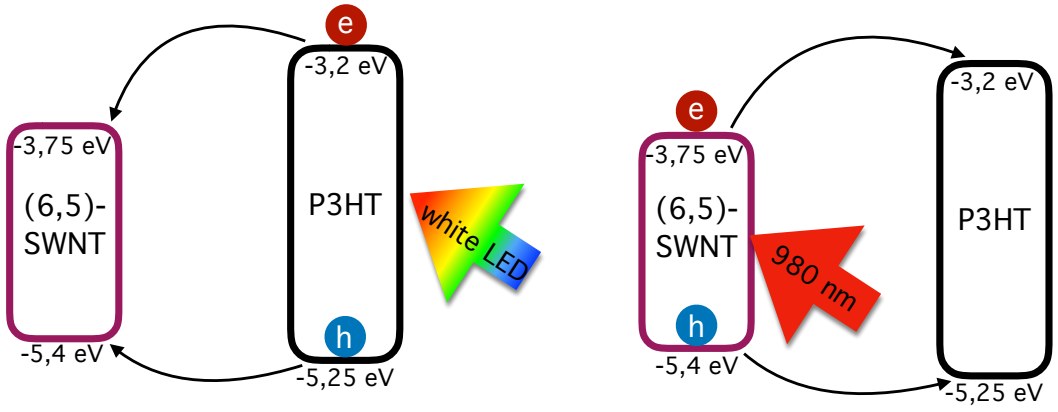

Figure 6.23: HOMO and LUMO levels of (6,5)-SWNT and P3HT under white LED and 980 nm laser light excitation.

P3HT seems energetically not possible. All these assumptions need to be verified, with EPR being the method of choice.

6.4.2 Probing Light Induced Charge Carriers

To exclude any potentially interfering signal we measured the background signal of the spectrometer loaded with an EPR tube only filled with helium. No signal contribution from the spectrometer or the EPR tube, i.e. quartzglas could be detected. First of all materials the matrix polymer PFO-BPy was tested and seemed to be inert under our measurement conditions, as assumed owing to its absorption spectrum. Nevertheless, it does show a marginal peak at $g = 2.000$ independent of illumination (compare Figure 6.5 in the previous section). It most probably origins from a tiny carbon radical residue as this g-factor is similar to an unpaired electron loosely bound to a carbon structure, which is also very close to the free electron's value. As this EPR signal is smaller then the overall signal noise it is negligible for further measurements.

Notation: Spectra measured without illumination are labeled "dark", under illumination with the white LED "white LED", after illumination with the white LED "afterdark", and "980 nm" refers to the used 980 nm laser light wavelength . The used microwave power will be given in Watt "W", the sample temperature in Kelvin "K". Standard parameters are 30 K, 2 mW and 0.15 mT field modulation if not denoted differently.

Simulated spectra are labeled "sim". The g-tensor values are estimated via simulations with EasySpin, running in Matlab environment [20]. The g-factor uncertainty is $\sigma_g = 0.00005$ if not denoted differently. The distinct g-factor distribution g_{Strain}

is responsible for the EPR signal linewidth, with $\sigma_{g_{Strain}} = 0.00005$, equal to around $\sigma_{\Delta H} = 0.005\,\text{mT}$ at the experimental frequency of 9.432 GHz.

The Fullerene EPR Signal

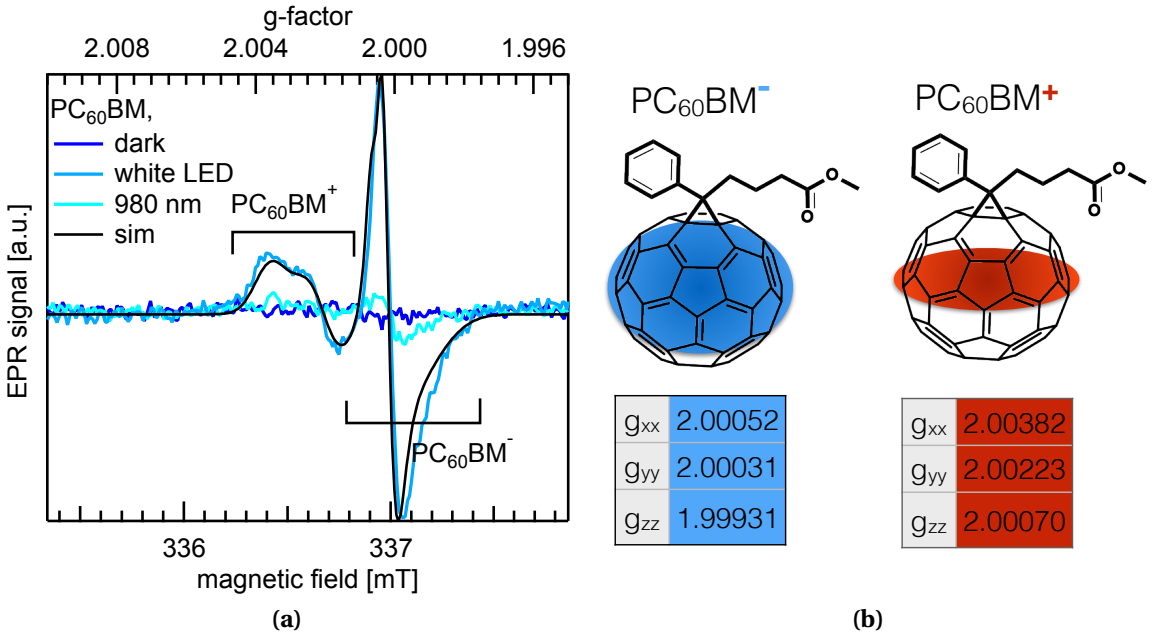

Figure 6.24: **(a)** $PC_{60}BM$ EPR spectra reveal two distinct signals, $PC_{60}BM^-$ [96], and $PC_{60}BM^+$. **(b)** Scheme for an electron or hole localised on the fullerene. The change in wave function distribution and thus g-tensor is most likely caused by the charge carriers effective mass.

To investigate charge transfer between (6,5)-SWNT and $PC_{60}BM$ we first studied pure $PC_{60}BM$ shown in Figure 6.24a. The EPR spectrum in the dark (dark blue) doesn't show any signal, except noise. On the other hand, two signals emerge under illumination with the white LED (bright blue). The signal on the right hand side is centered at an average g-factor of around $g = 2.000$ and has a peak to peak width of 0.1 mT. It can be assigned to $PC_{60}BM^-$ and is already known in literature [96]. The signal on the left hand side is most probably $PC_{60}BM^+$, centered at around $g = 2.002$ it exhibits an anisotropic g-tensor and spreads over around 0.6 mT. Illumination of the sample with 980 nm laser light (cyan) induces a marginal $PC_{60}BM^-$ and $PC_{60}BM^+$ signal, only twice as high as the signal noise. Additionally, EPR investigations at various spectrometer parameters and spectra simulations (black) were performed to ensure the signal assignments to two distinct spin species, i.e. anions and cations.

Discussion

PCBM fullerene derivatives were firstly synthesised in the 1990s by Hummelen et al. [194]. The $PC_{60}BM$ anion EPR signature is well known in literature. It has been investigated by Konkin et al. [97], and Niklas et al. [100], among others, and its properties have been slightly adjusted to our systems [101, 102, 103, 104]. Niklas also used DFT caclulations to show the spin density to be distributed over the buckyball, where the highest g-tensor value corresponds to the axis with the lowest spin density. That photoexcited $PC_{60}BM^+$ exists, i.e. that $PC_{60}BM$ is capable of intermolecular CT, has been shown in pristine $PC_{60}BM$ solar cell devices [195], and thin C_{60} films [196]. It is also indicated by ambipolar field-effect transistors [197], and transport measurements [198]. To firstly verify that we indeed observe two distinct species in our EPR experiments, we performed saturation measurements (not shown) supporting our assignment. C_{60} has been vastly investigated via EPR, but its derivative $PC_{60}BM$ did not get nearly as much attention. As far as we know, the $PC_{60}BM^+$ signal in thin film hasn't been reported in literature yet. As the $PC_{60}BM$ anion is mostly distributed on the C_{60} buckyball, we assume the situation not to be much different for its cation. Hence, the following discussion relies on EPR investigations of cations on C_{60} buckyballs. The C_{60}^+ form has been electrochemically identified by Xie et al. [199]. Reed summarised the reports of EPR spectra ascribed to C_{60}^+ with g-values and line width perfectly consistent with our observations [200]. Nevertheless, they always did show single g-factors, no g-tensors. Therefore, it can be questioned whether the PCBM cation is also localised on the buckyball or the side chain. Why we assume a distribution on the buckyball and an isotropic g-tensor for $PC_{60}BM^+$ will be discussed in the following.
Polymer cations' g-tensors are extraordinary close to the one we observed [201]. That is especially true for the poly-hexylthiophene P3HT (see chapter 5.3.1 for comparison). We did repeat the measurements to exclude P3HT contamination Furthermore, the P3HT g-tensor is generally never that pronounced, but rather smeared out due to averaging of various g-tensor orientations resulting in strained values, i.e. high g_{Strain}. The P3HT g-tensor exhibits narrow g_{Strain} values only in the case of proper layer alignment after annealing [202]. None of the aforementioned can be applied to our case, leaving us with a polymer-like g-tensor which can not be attributed to a polymer. Thus it might seem reasonable to think that the cation on $PC_{60}BM$ is localised on the fullerene side chain. But, the P3HT charge carrier distribution has been calculated via DFT, indicating distributions over at least 10 thiophene units (4 nm) [203]. This is not even close to the size of the phenyl-methyl-ester side chain of the fullerene which would yield a different g-tensor. Additionally, there are no hyperfine couplings observable that might be addressed to the oxygen nuclear spin on the ester group. Therefore, we assume the

cation to be distributed over the buckyball which we will now set our focus on.
The EPR literature values of C_{60} buckyball cations do vary and indicate slightly different charge carrier distributions, i.e. a high sensitivity regarding the environment. For example for C_{60} in dilute solution doped with H_2SO_4 acid a weak narrow resonance at g=2.0030 was seen and assigned to C_{60}^+ by Kukolich [99]. The C_{60} cation in solution with $SbCl_5$ at RT shows a single line between g=2.0023 and 2.0029 with a narrow linewidth of 0.15-0.20 mT [204]. Siedschlag oxidised C_{60} with H-donors using PET conditions resulting in a C_{60}^+ signal at g=2.0021 with 0.8 mT linewidth [205]. C_{60} was also introduced into the $Fe3^+$ zeolite Y, a microporous aluminosilicate, resulting in C_{60}^+ with g=2.0025 and 1 mT linewidth at 298 K [206]. The Eatons did show a hydrogen *p*-doped $C_{60}H^*$ with g=2.0022 and a hyperfine splitting of a_H=33 G [207], something we exclude as we do not observe such a splitting. They also claimed photoexcited C_{60} to be susceptible to reactions with solvent impurities, but as we investigate a thin film there is no solvent to react with.
The fact that most C_{60}^+ g-values in literature are g-factors and not g-tensors can be explained with high sample temperatures and measurements in solution. Due to the (Brownian) motion in a liquid environment the g-tensor anisotropy is averaged out, resulting in simple g-factors. Note that a similar averaging of the g-tensor orientations might also occur in frozen solution if the solvent freezing takes place on a faster time scale than the fullerene crystallisation. In general, a splitting of the g-factor into a g-tensor at cryogenic temperatures can be expected, due to the reduced motion of the molecules and hence less broadening and averaging out of the g-tensor. In general, fullerene line width drops radically, i.e. gets smaller while going from 300 K to liquid nitrogen and even further for liquid helium temperatures [208].
Our elaborate g-tensor investigation yields an anisotropic g-tensor for $PC_{60}BM^+$ shown in Figure 6.24b. The anion distribution on the $PC_{60}BM$ fullerene is schematically highlighted as a blue ball with a slightly higher density around the equator [209]. The corresponding g-tensor is almost isotropic and its' values are shown in the table below also highlighted in blue. The rather restricted cation distribution is highlighted in red with a correspondingly strong anisotropic g-tensor, shown in the table below and also highlighted in red. Due to the deviating effective mass of the hole in comparison to the electron we get a strongly distorted wave function. This wave function is quite similar to electrons on the egg-shaped $PC_{70}BM$ fullerene (see table 5.1 in chapter 5.3.1 for comparison). A similar result can be found for the egg shaped C_{76}^+ with an EPR signature at g=2.0030 [210]. All in all, the elliptical cation distribution along the C_{60} equator of the $PC_{60}BM$ fullerene seems to be a reasonable assumption.

Sidenote: To be absolutely sure about the signal assignment to $PC_{60}BM^+$ there are different supporting measurements possible, but are beyond the scope of this work. Nevertheless, all the aforementioned methods with concentrated or fuming sulfuric acid (H_2SO_4) [99], antimony pentachloride $SbCl_5/Ch_2Cl_2$ [204], Ar_3N^+ and others [211], yielding C_{60} cations can also be utilised to gain $PC_{60}BM$ cations. Additionally, we could use iodine as *p*-dopant for $PC_{60}BM$ thin films. Another option would be solvent doping with for example $AuCl_3$ and then measuring frozen solution, as investigated in the previous chapter with carbon nanotubes.

The Fullerene and SWNT Blend EPR Signal

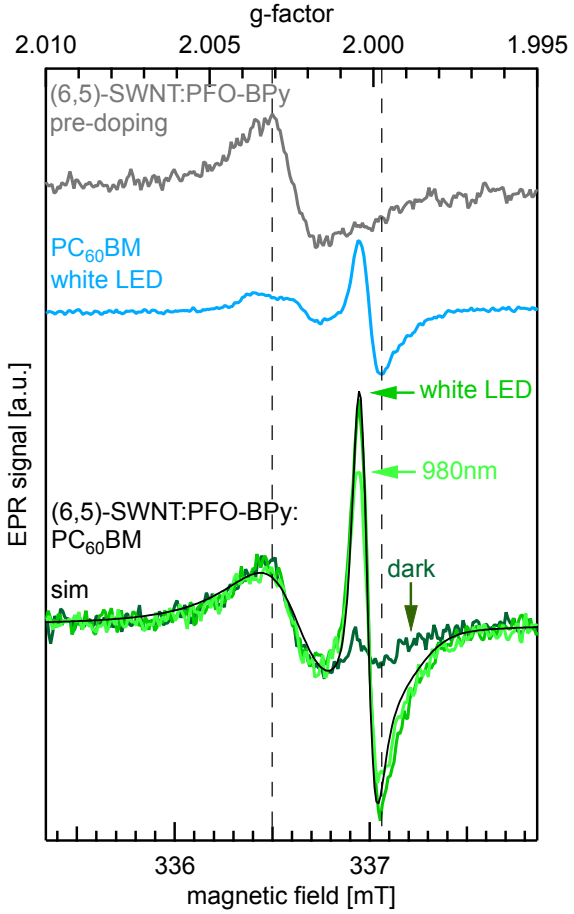

Figure 6.25: EPR spectra of (6,5)-SWNT:PFO-BPy and $PC_{60}BM$ normalised to their material amount. For comparison we did add the pure (6,5)-SWNT:PFO-BPy pre-doping signal (grey) and $PC_{60}BM$ (bright blue) with white LED illumination. The (6,5)-SWNT:PFO-BPy:$PC_{60}BM$ blend reveals almost equal signal intensities for white LED (green) and 980 nm (neon green) excitation. As we only excite the (6,5)-SWNTs at 980 nm and no $PC_{60}BM^+$ can be observed, revealed by simulations (black), we deduce CT between (6,5)-SWNTs and $PC_{60}BM$s.

Now, we are familiar with the EPR signatures of pure $PC_{60}BM$ and (6,5)-SWNT pre-doping (see chapter 6.2). Therefore, we can distinguish both signal contributions in a blend to determine CT, as discussed in the following. Please note, that additional cross measurement with PFO-BPy and $PC_{60}BM$ were carried out. They revealed that PFO-BPy is electronically inert not only as pure material but in mixtures as well and does not alter the EPR signal in intensity or shape, independent of temperature or illumination. Thus, PFO-BPy won't be discussed in the following. The EPR spectra of the (6,5)-SWNT:PFO-BPy:$PC_{60}BM$ blend for different illumination wavelengths are shown in green in Figure 6.25. For comparison, we did add the pre-doping signal of pure (6,5)-SWNT:PFO-BPy (grey) and the $PC_{60}BM$ (bright blue) signal under white LED illumination. All spectra are normalised with respect to the material amounts in the blend. Therefore, the shown intensities are directly comparable. The EPR spectrum of the blend in the dark (dark green) reveals the already known (6,5)-SWNT pre-doping signal. A marginal $PC_{60}BM^-$ contribution can also be seen. If we illuminate the sample with the white LED (bright green) the (6,5)-SWNT signal doesn't change in intensity, whereas a strong $PC_{60}BM^-$ peak emerges. After changing the light source to 980 nm laser light (neon green), the $PC_{60}BM^-$ peak intensity decreases slightly, while the (6,5)-SWNT signal remains unchanged. Simulations (black) for the (6,5)-SWNT background doping signal and $PC_{60}BM^-$ were carried out to reproduce the spectra.

Discussion

A reason for the minor $PC_{60}BM^-$ signal in the blend even without illumination (dark green) might be a not sufficiently dark spectrometer. At cryogenic temperatures of 30 K the charge carriers are immobile and thus recombine slowly and therefore are long-living. If now unintended photons did enter the spectrometer they might result in a minor long living $PC_{60}BM^-$ signal. Therefore, we did heat up the samples to room temperature after every measurement before cooling down again to record the next spectrum. The $PC_{60}BM^-$ signal in the blend under illumination with the white LED (bright green) reaches a quite strong intensity. If we compare it to the pure $PC_{60}BM$ sample (bright blue) it is around twice as high. Furthermore, the $PC_{60}BM^+$ signal can't be observed, indicating the holes to be localised on the nanotube. Why the holes can't be observed will be answered in the following. To confirm the attribution of the signals we performed simulations for all spectra with signal contributions from $PC_{60}BM^-$ and the (6,5)-SWNT pre-doping (a sample curve is shown in black). The $PC_{60}BM^-$ signal in the blend under illumination with 980 nm laser light (neon green) reaches an intensity quite as strong as with the white LED. As exclusively (6,5)-SWNTs absorb at 980 nm, this is a strong hint on electron transfer from (6,5)-SWNTs to $PC_{60}BM$. Neither

$PC_{60}BM^+$ nor (6,5)-$SWNT^+$ can be seen as a result of CT with $PC_{60}BM$. A reason for the lack of an (6,5)-$SWNT^+$ signal might be the exceptional charge carrier mobility on (6,5)-SWNTs, discussed in chapter 3.3. If it is too high, the charge carriers might move too fast for cw EPR detection taking place on a time scale of ≈100 ns. Additionally, the highly mobile charge carrier might delocalise on the nanotube yielding no specific orientation for the corresponding spin. Therefore, the microwave absorption is independent from the external magnetic field. This results in a microwave absorption offset which is not detectable via our lock-in detection technique (see chapter 4.2 for more details). Nevertheless, we observe higher $PC_{60}BM^-$ signal intensities in the blend with (6,5)-SWNTs than in the pure $PC_{60}BM$ sample, independent of white LED or 980 nm illumination. Additionally, there is no $PC_{60}BM^+$ signal observable in the blend. Therefore, we conclude hole transfer from $PC_{60}BM$ to (6,5)-SWNT as well as electron transfer from (6,5)-SWNT to $PC_{60}BM$.

The Polymer EPR Signal

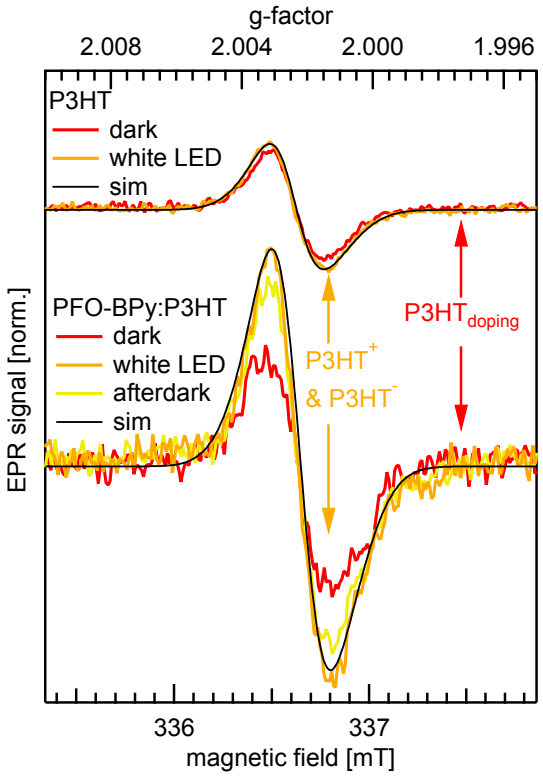

Figure 6.26: EPR spectra for P3HT and PFO-BPy:P3HT, normalised to the material amounts of P3HT. Both samples show a quantitatively similar doping signal $P3HT_{doping}$ without illumination (red). Both sample signals increase under white LED illumination (orange) due to intermolecular $P3HT^+$ and $P3HT^-$ separation. Simulations (black) show identical signal signatures. Neither PFO-BPy:P3HT nor P3HT change their dark signal intensity with 980 nm illumination (not shown). The P3HT afterdark signal, i.e. after switching off the white LED, (not shown) decays back to dark signal height while the PFO-BPy:P3HT afterdark signal (yellow) only slightly decreases. This, and the higher intensity under illumination in comparison to pure P3HT indicate a change in polymer domain size. Thus, PFO-BPy seemingly increases the efficiency of intermolecular CT on P3HTs.

To verify whether PFO-BPy reacts with P3HT or not, we did blend and compare both materials, shown in Figure 6.26. The P3HT and PFO-BPy:P3HT EPR measurements are shown together. The dark signal (red) is centered at $g = 2.0025$ and around 0.3 mT wide from peak to peak. Under illumination (orange), its intensity increases slightly for pure P3HT while it doubles for PFO-BPy:P3HT. After switching off illumination the signal in P3HT decreases back to dark signal height, not shown. In PFO-BPy:P3HT the signal decreases only slightly after switching off illumination, i.e. afterdark (yellow). Simulations (black), performed for all spectra and exemplarily shown for illumination

with the white LED indicate identical signal signatures (ISS) with varying intensity in all cases.

Discussion

The EPR signal of the OPV workhorse P3HT is well known in literature [100, 96], with slight variations depending on the systems it is used in. Additionally, EPR investigations at various spectrometer parameters and spectra simulations (black) were performed to support the following signal assignments. The dark signal (red) centered at g=2.0025 is in both cases most probably caused by P3HT *p*-doping due to oxygen and water, commonly reported in literature [212, 213, 214, 159, 215]. The increase under illumination is caused by $P3HT^{+}$ and $P3HT^{-}$ intermolecular CT [216]. Note that their almost identical g-tensor values are indistinguishable via X-Band EPR [159]. We observe a much stronger signal intensity increase under illumination in the PFO-BPy:P3HT blend than in pure P3HT, but equal signal signatures. As the electron and hole separation is most probably possible due to different P3HT domains [216, 217], it seems reasonable to assume that PFO-BPy changes the formation of P3HT domains. Additionally, the low signal decrease in PFO-BPy:P3HT after switching off the white LED (yellow) indicates slow charge carrier recombination. This is also explained by the change in P3HT domain size. Therefore, we conclude that PFO-BPy only changes the morphology of the EPR samples. Otherwise it is electronically inert, not only as pure material but in all our blends as well.

The Polymer and SWNT Blend EPR Signal

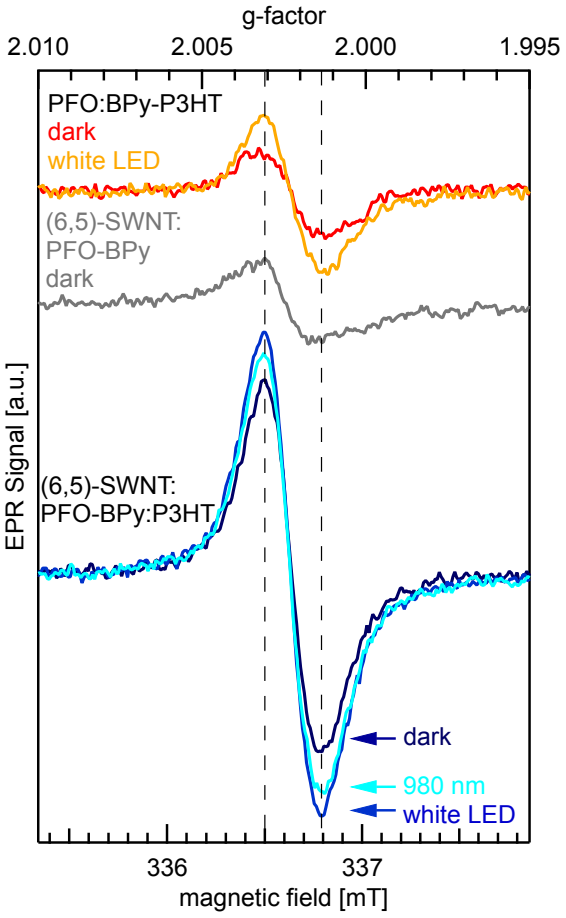

Figure 6.27: EPR spectra of PFO-BPy:P3HT, (6,5)-SWNT:PFO-BPy and their blend for various illumination wavelength. All contain the same amounts of the corresponding materials, thus intensities are directly comparable. The (6,5)-SWNT:PFO-BPy:P3HT dark signal (dark blue) is the superposition of the (6,5)-SWNT (grey) and PFO-BPy:P3HT (red) dark signal. The signal intensity under illumination with the white light LED (navy blue) and the 980 nm light (neon blue) increases yielding almost equal spectra. As only (6,5)-SWNTs absorb at 980 nm and not P3HT, and only the P3HT signal increases under illumination we conclude CT between (6,5)-SWNT and P3HT.

Now, we are familiar with the EPR signatures of (6,5)-SWNT pre-doping (see chapter 6.2) and pure P3HT. Therefore, we can distinguish both signal contributions in a blend to determine CT, as discussed in the following. The (6,5)-SWNT:PFO-BPy:P3HT EPR spectra under illumination with various wavelength are shown in Figure 6.27. We did add the EPR spectra of PFO-BPy:P3HT without- and with illumination (red and orange, respectively) as well as the pre-doping signal of pure (6,5)-SWNT:PFO-BPy (grey) for comparison. The (6,5)-SWNT:PFO-BPy:P3HT dark signal (dark blue) shows an already high signal intensity. Under illumination with the white LED (navy blue) the signal

intensity increases. Sample illumination with 980 nm laser light (neon blue) reaches an almost equal signal intensity as with the white LED (navy blue).

Discussion

The P3HT *p*-doping EPR signal (red) is almost identical to the (6,5)-SWNT pre-doping signal (grey). Therefore, it is not possible to observe a clear separation of the two overlapping signals in the blend (dark blue) even with an elaborate EPR investigation at various spectrometer parameters, like temperature and modulation, as well as illumination strengths. The (6,5)-SWNT:PFO-BPy:P3HT signal does act like it is actually one signal. Only a detailed but unspectacular investigation of the signal broadening for increasing microwave powers indicated two overlapping signals. The similar signal shape and behaviour of SWNT pre- and P3HT *p*-doping seems conclusive as both are mainly the result of oxygen/water *p*-doping. See literature [212, 213, 214, 159, 215] for P3HT oxygen/water interactions and chapter 6.2 for atmospheric doping of (6,5)-SWNT. The already quite strong SWNT:PFO-BPy:P3HT dark signal (dark blue) can be explained by a simple superposition of the (6,5)-SWNT and P3HT doping signals, i.e. the grey and red signal, respectively. The signal intensity increase under illumination, with the white LED (navy blue) can in principle be solely ascribed to P3HT, because illumination of the (6,5)-SWNT sample doesn't lead to higher signal intensities. Also CT between (6,5)-SWNT and P3HT could be an explanation for the signal increase, but is not indicated as the change is quite similar to PFO-BPy:P3HT without (6,5)-SWNT. To verify this, optical measurements in the region of the (6,5)-SWNT luminescence could be employed to determine if electrons and holes are transferred from P3HT to (6,5)-SWNT which recombine radiatively on the nanotube.
An external quantum efficiency (EQE) of 0 % and no photoluminescence (PL) above ≈650 nm indicate no P3HT excitation at 980 nm [216, 218]. Additionally, the PFO-BPy:P3HT sample did not show a signal intensity increase under illumination with 980 nm laser light. As only (6,5)-SWNTs absorb at 980 nm and not P3HT, and only the P3HT signal increases under illumination we conclude CT between (6,5)-SWNT and P3HT. Due to the not existing spectral overlap, a Förster resonance transfer seems unlikely. Regarding the HOMO and LUMO orbitals, discussed in section 6.4.1, an 1 eV energy gap for electron transfer from (6,5)-SWNT to P3HT makes this process seem rather unlikely. Thus, we assume hole transfer from (6,5)-SWNT to P3HT. An electron transfer from P3HT to (6,5)-SWNT might occur, but can't be proven as the holes could also be separated on P3HT domains. Sidenote: We did perform the same measurements with PCDTBT instead of P3HT, where no indications of CT between PCDTBT and (6,5)-SWNTs could be observed.

6.4.3 Summary

In this section we utilised EPR to investigate charge transfer between the (6,5)-SWNT and the fullerene derivative $PC_{60}BM$, as well as the polymer P3HT. We found the (6,5)-SWNT matrix polymer PFO-BPy, necessary for their purification, to be electronically inert in our EPR measurements, thus it does not directly contribute to the EPR spectra or the charge transfer reactions. By comparing EPR signal intensities for white LED illumination as well as 980 nm laser light, where only (6,5)-SWNTs are excited, we revealed hole transfer from $PC_{60}BM$ to (6,5)-SWNT, and electron transfer from (6,5)-SWNT to $PC_{60}BM$. Additionally, we showed the $PC_{60}BM$'s cation g-tensor indicating a charge carrier distribution on the buckyball, significantly perturbed in comparison to the anion. Similarly, we employed 980 nm laser light to investigate (6,5)-SWNT and P3HT CT. As only (6,5)-SWNTs are excited at 980 nm wavelength, we were able to reveal CT from (6,5)-SWNT to P3HT, most probably holes, resulting in an increasing EPR signal intensity. Despite being electronically inert, PFO-BPy seems to influence the formation of domains in P3HT.
All in all we could find some hints of (6,5)-SWNT ambipolarity, i.e. the ability to transport electrons as well as holes on (6,5)-SWNTs in blends with organic semiconductors, extraordinaryly helpful for their application. This has to be investigated in more detail, for example by characterising bilayer solar cells. Ambipolarity of different chirality CNTs was already shown in field effect transistors [219, 220, 221], and is also indicated in our measurements.

7 Summary

In the present work we investigated various charge transfer processes, as the appear in the versatile world of organic semiconductors by probing the spin states of the corresponding charge carrier species via electron paramagnetic resonance (EPR) spectroscopy. All studied material systems are carbon-based compounds, either belonging to the group of polymers, fullerenes, or single-wall carbon nanotubes (SWNTs). At first the properties of spins and several interaction mechanisms with magnetic fields were introduced and the appearance of EPR signals, and how they can be both simulated and quantified was discussed. The materials were introduced briefly, followed by a general description of the sample preparation. Afterwards, the measurement method was discussed together with the spectrometer design.

In the first instance, we addressed the change of the open circuit voltage (V_{OC}) with the fullerene blend stoichiometry in fullerene-based solar cells for organic photovoltaics (OPV). The V_{OC} is decisive for successful charge transfer after optical excitation. The voltage depends strongly on the energy separation between the lowest unoccupied molecular orbital (LUMO) of the donor and the highest occupied molecular orbital (HOMO) of the acceptor. However, in the systems investigated here, two different acceptors were used in different ratios, namely C_{60}, C_{70}, and their derivatives. Although it is known that the V_{OC} of fullerene-based solar cells changes by mixing two different fullerene derivatives and varying their ratios, the associated phenomena are still not fully understood. To understand what happens on the molecular level, EPR experiments were performed at low temperatures. The focus was set on the distribution between the two LUMOs of the fullerene acceptors. By exploiting the Gaussian distribution of the charge carriers in a two-level system, and thus also their spins in the EPR experiment, it could be shown that the LUMOs get closer by a few to a few hundred meV when going from pure fullerene materials to a fullerene mixture. The reason for this strong energetic effect is likely the formation of a fullerene alloy. This conclusion is supported by a distinctive EPR signature corresponding to an electron, delocalised over two different fullerenes.

Further, we investigated the chemical doping mechanism of single-walled carbon nanotubes (SWNTs) with a (6,5)-chirality and their behaviour under optical excitation

by means of EPR spectroscopy. If desired, doping is necessary for the application of nanotubes or generally 1-D materials in semiconductor systems. If undesired, the causes of doping must be known in order to reduce it in the future, if not completely avoid it. The analysed (6.5)-SWNTs were prepared in the group of Prof. Tobias Hertel by purifying a mixture of nanotubes of different chirality in an elaborate process. In order to determine the unintentional doping, EPR spectra of the raw nanotubes as well as after different purification steps were recorded. This facilitated the determination of nanotube defects and atmospheric *p*-doping as the causes of the measured EPR signals. The former has a concentration of 5.6±1.4 spins per μm nanotube, the latter of 4.1±0.9 spins per μm nanotube, while one μm consists of 88,000 carbon atoms. In order to deliberately transfer additional charge carriers to the nanotubes, we added the redox-active substance $AuCl_3$. The associated doping-yield was determined via EPR spectroscopy to be (1.5±0.2)% spins per $AuCl_3$. These results are in outstanding agreement with values determined via photoluminescence spectroscopy in the group of Prof. Tobias Hertel. In addition, a statistical occupation model was developed which can be used to simulate the distribution of EPR active, i.e. unpaired and localised charge carriers on the nanotubes. It was shown that a charge carrier separation of (3.5±1.0) nm can be regarded as a critical distance before spin alignment occurs. Finally, we investigated the charge transfer behaviour of (6,5)-SWNTs together with the polymer P3HT and the fullerene $PC_{60}BM$ after optical excitation. With nanotubes being used as additives in many electronic and optoelectronic systems nowadys, it is essential to know whether nanotubes exchange charge carriers both with polymers and with fullerenes. In order to distinctly generate charge carriers, the different absorption regimes of the materials were used to selectively excite them. It could be shown that electrons can be transferred from (6,5)-SWNTs to $PC_{60}BM$, and holes vice versa. In the case of P3HT charge transfer was confirmed, but the nature of the charge carriers could not be pinpointed as holes with certainty. If the ambipolarity of (6,5)-SWNTs can be verified, i.e. the ability to transfer both electrons and holes, which requires further measurements on EPR spectrometers with higher fields, it would be extremely helpful for their application.

In summary, this work has shown how powerful EPR spectroscopy can be to investigate charge transfer processes in the field of organic semiconductors. It has thus made a contribution to understanding what happens when fullerenes are mixed, what happens when nanotubes are deliberately doped, that there is undesired doping that is difficult to avoid, and that nanotubes can contribute very actively to charge transfer when illuminated.

Zusammenfassung

Die vorliegende Arbeit untersuchte mit Hilfe der Elektron Paramagnetischen Resonanz Spektroskopie (EPR) die Ladungsträgerspins bei Ladungstransfer-Prozessen in organischen Halbleitern. Insbesondere wurden hier verschiedene Kohlenstoffverbindungen betrachtet, welche zur Gruppe der Polymere, Fullerene, oder Kohlenstoff-Nanoröhren gehören. Begonnen haben wir mit den allgemeinen Eigenschaften des Spins, um danach einige seiner Wechselwirkungsmechanismen näher betrachten zu können. Welche Signale verschiedene Spin Spezies im EPR Experiment zeigen und wie man dieses sowohl simulieren, als auch quantifizieren kann wurde ebenfalls dargelegt. Nach einer kurzen Materialvorstellung folgte eine Übersicht über die Probenherstellung. Anschließend wurde die Messmethode und der Aufbau des Spektrometers näher beleuchtet.

Mit den Ergebnissen beginnend, gingen wir auf die Veränderung der Leerlaufspannung in Fulleren Solarzellen für organische photovoltaic (OPV) ein, welche mit der Fulleren Stöchiometry variiert. Die Leerlaufspannung ist entscheidend für das Ladungsstransfer-Verhalten nach erfolgreicher optischer Anregung. Sie hängt stark vom Energieabstand des niedrigsten unbesetzten Molekülorbitals (engl. LUMO) des Donators zum höchsten besetzten Molekülorbital (engl. HOMO) des Akzeptors ab. In den hier betrachteten Fällen wurden allerdings zwei verschiede Akzeptoren in unterschiedlichen Mischungsverhältnissen verwendet, darunter C_{60}, C_{70} und deren Derivate. Obwohl es bekannt ist, dass sich die Leerlaufspannung von Fulleren-basierten Solarzellen ändert wenn man zwei verschiedene Fulleren Typen mischt und deren Verhältnis variiert, ist die Ursache dafür nicht umfassend verstanden. Um zu verstehen was auf der molekularen Ebene geschieht, wurden EPR Experimente bei niedrigen Temperaturen durchgeführt. Der Fokus lag hierbei auf der Verteilung zwischen den beiden LUMOs der Fulleren Akzeptoren. Hierbei wurde die Gaußsche Verteilungs-Statistik der Ladungsträger, und damit auch deren Spins, in einem zwei Niveau System im EPR Experiment ausgenutzt. Es konnte gezeigt werden, dass sich deren Abstand um wenige bis hin zu wenigen Hundert meV annähert wenn man vom reinen Fulleren Material zu einem Fulleren Gemisch übergeht. Die Ursache für diesen starken energetischen Effekt ist wahrscheinlich die Bildung einer Fulleren-Legierung. Diese Schlussfolgerung wird durch ein besonderes EPR Signal unterstützt, das einem Elektron entspricht welches über zwei verschiedene Fullerene delokalisiert ist.

Daraufhin betrachteten wir speziell einwandige Kohlenstoff-Nanoröhren der Chiralität (6,5). Untersucht wurde zunächst die chemische Dotierung dieser Systeme und anschließend ihr Verhalten bei optischer Anregung. Dotierung ist, sofern gewünscht, wichtig für die Anwendung von Nanoröhren, oder 1-D Materialien im Allgemeinen, in

Halbleiter-Systemen. Falls ungewünscht, ist es elementar zu wissen wie diese Dotierung entsteht um sie in Zukunft reduzieren, wenn nicht sogar vollständig vermeiden zu können. Die untersuchten (6,5)-Nanoröhren wurden in der Gruppe von Prof. Tobias Hertel präpariert und in einem aufwändigen Verfahren aus einem Gemisch von Nanoröhren unterschiedlicher Chiralität aufgereinigt. Um zunächst die ungewünschte Dotierung zu ermitteln, wurden EPR Spektren der Nanoröhren in unbehandelter Form, als auch nach unterschiedlichen Aufreinigungsschritten aufgenommen. Dies ermöglichte die Bestimmung von Nanorohr-Defekten und atmosphärischer Dotierung als Ursache für das gemessene EPR Signal. Ersteres hat eine Konzentration von 5,6±1,4 Spins pro μm, letzteres von 4,1±0,9 Spins pro μm Nanorohr, wobei ein μm aus 88.000 Kohlenstoffatomen besteht. Um bewusst zusätzliche Ladungsträger auf die Nanoröhren zu übertragen gaben wir die redox-aktive Substanz $AuCl_3$ hinzu. Die zugehörige Dotiereffizienz konnte zu (1,5±0,2)% spins pro $AuCl_3$ bestimmt werden. Photolumineszenz Spektroskopie in der Gruppe von Prof. Tobias Hertel ermöglichte ebenfalls eine quantitative Bestimmung der Dotierung, welche eine überragende Übereinstimmung mit den per EPR Spektroskopie ermittelten Werten zeigt. Darüber hinaus wurde ein statistisches Modell erarbeitet welches die Verteilung von EPR aktiven, d.h. ungepaarten und lokalisierten Ladungsträgern auf den Nanoröhren simulieren kann. Es zeigte sich, dass ein Abstand von (3,5±1,0) nm zwischen den Ladungsträgern als kritische Distanz angesehen werden kann, bevor deren Spins sich antiparallel ausrichten.

Zum Abschluss betrachten wir das Ladungstransfer-Verhalten von (6,5)-Nanoröhren zusammen mit dem Polymer P3HT und dem Fulleren $PC_{60}BM$ nach optischer Anregung. Da Nanoröhren mittlerweile in sehr vielen elektronischen-, als auch optoelektronischen Systemen as Additiv genutzt werden ist es unverzichtbar zu wissen ob Nanoröhren sowohl mit Polymeren, als auch mit Fullerenen Ladungsträger austauschen. Zur Anregung dieser Ladungsträger wurden die unterschiedlichen Absorptionsbereiche der Materialien ausgenutzt, um gezielt eine selektive Anregung zu erreichen. Dadurch konnte gezeigt werden, dass sowohl Elektronen von Nanoröhren auf $PC_{60}BM$, als auch Löcher in die Gegenrichtung übertragen werden können. Im Falle von P3HT konnte Ladungstransfer bestätigt, aber die Ladungsträger selber nicht mit Sicherheit als Löcher identifiziert werden. Sollte sich die Ambipolarität von (6,5)-Nanoröhren bestätigen, also die Eigenschaft sowohl Elektronen als auch Löcher zu übertragen, wofür noch weitere Meßungen an EPR Spektrometern mit höheren Feldern notwendig wären, wäre dies äußert hilfreich für deren Anwendung.

Zusammenfassend hat diese Arbeit gezeigt wie leistungsfähig die EPR Spektroskopie ist auf dem Gebiet der organischen Halbleitern Ladungstransfer-Prozesse zu untersuchen. Sie hat dadurch einen Beitrag dazu geleistet zu verstehen was passiert wenn

Fullerene gemischt werden, was passiert wenn Nanoröhren gezielt dotiert werden, dass es unerwünschte Dotierung gibt die sich schwer vermeiden lässt, und das Nanoröhren auch bei Beleuchtung sehr aktiv zum Ladungstransfer beitragen können.

Bibliography

[1] C. Brabec, U. Scherf, and V. Dyakonov. *Organic Photovoltaics: Materials, Device Physics, and Manufacturing Technologies*. Wiley, 2011, ISBN=9783527623204. URL: https://books.google.de/books?id=DSGQi34Q36wC.

[2] Derya Baran, Rajy Shahid Ashraf, David A. Hanifi, Maged Abdelsamie, Nicola Gasparini, Jason A. R´ohr, Sarah Holliday, Andrew Wadsworth, Sarah Lockett, Marios Neophytou, Christopher J. M. Emmott, Jenny Nelson, Christoph J. Brabec, Aram Amassia, Alberto Salleo, Thomas Kirchartz, James R. Durrant, and Ian McCulloch. Reducing the efficiency–stability–cost gap of organic photovoltaics with highly efficient and stable small molecule acceptor ternary solar cells. *Nature Materials*, 16:363–369, 2017. doi:10.1038/nmat4797.

[3] Molang Cai, Yongzhen Wu, Han Chen, Xudong Yang, Yinghuai Qiang, and Liyuan Han. Cost-performance analysis of perovskite solar modules. *Advanced Science*, 4(1):1600269, 2017. doi:10.1002/advs.201600269.

[4] Ossila. Die Klimakonferenz in Paris. [Date: 12.06.2019] Link:https://www.bmu.de/themen/klima-energie/klimaschutz/internationale-klimapolitik/pariser-abkommen/.

[5] IBM. Photovoltaics Report, 2015. [Date:10.12.2015] https://www-03.ibm.com/press/us/en/pressrelease/47767.wss.

[6] Qing Cao, Shu-jen Han, Jerry Tersoff, Aaron D Franklin, Yu Zhu, Zhen Zhang, George S. Tulevski, Jianshi Tang, and Wilfried Haensch. End-bonded contacts for carbon nanotube transistors with low, size-independent resistance. *Science*, 350(6256):68–72, 2015. doi:10.1126/science.aac8006.

[7] Andrea Mazzatenta, Michele Giugliano, Stephane Campidelli, Luca Gambazzi, Luca Businaro, Henry Markram, Maurizio Prato, and Laura Ballerini. Interfacing neurons with carbon nanotubes: Electrical signal transfer and synaptic stimulation in cultured brain circuits. *Journal of Neuroscience*, 27(26):6931–6936, 2007. doi:10.1523/JNEUROSCI.1051-07.2007.

[8] Viviana Lovat, Davide Pantarotto, Laura Lagostena, Barbara Cacciari, Micaela Grandolfo, Massimo Righi, Giampiero Spalluto, Maurizio Prato, and Laura Ballerini. Carbon nanotube substrates boost neuronal electrical signaling. *Nano Letters*, 5(6):1107–1110, 2005. doi:10.1021/nl050637m.

[9] Hans C. Ohanian. What is spin. *American Journal of Physics*, 54:500, 1986. doi:http://dx.doi.org/10.1119/1.14580.

[10] Charles P. Poole. *Electron spin resonance: a comprehensive treatise on experimental techniques*. Dover Publications Inc., 1967, ISBN=0-486-69444-5.

[11] Dieter Meschede. *Gerthsen*. Springer Verlag, 2004, ISBN=978-3662459768.

[12] Wolfgang Demtröder. *Experimentalphysik 3: Atome, Moleküle und Festkörper*. Springer-Lehrbuch. Springer Berlin Heidelberg, 2010, ISBN=9783642039119.

[13] D. Halliday, R. Resnick, and J. Walker. *Halliday Physik*. Wiley-VCH, 2001, ISBN=978-3527409198.

[14] Theo Mayer-Kuckuk. *Atomphysik*. Teubner-Studienbücher, 1997, ISBN=3-519-43042-8.

[15] Paul Dirac. The Quantum Theory of the Electron. *Science*, 117, 1928. doi:10.1098/rspa.1928.0023.

[16] Nist. National institute of standards and technology. www.nist.gov [Date:02.06.2019].

[17] H. M. Assenheim. *Introduction to Electron Spin Resonance*. Springer Berlin Heidelberg, 1966, ISBN=978-1-4899-5504-3. doi:10.1007/978-1-4899-5502-9.

[18] Anatole Abragam and Maurice Henry Lecorney Pryce. Theory of the nuclear hyperfine structure of paramagnetic resonance spectra in crystals. *Proceedings of the Royal Society of London*, 205:135–153, 1951. doi:10.1098/rspa.1951.0022.

[19] Stefan Stoll. *Spectral simulations in solid-state electron paramagnetic resonance*. Doctoralthesis, Swiss Federal Instituite of Technology Zürich, 1998.

[20] Stefan Stoll and Arthur Schweiger. EasySpin, a comprehensive software package for spectral simulation and analysis in EPR. *Journal of Magnetic Resonance*, 178, 2006. doi:10.1016/j.jmr.2005.08.013.

[21] John A. Weil and James R. Bolton. *Electron Paramagnetic Resonance: Elementary Theory and Practical Applications*. John Wiley & Sons, Inc, 1994, ISBN=0-471-57234-9.

[22] Daniella Goldfarb and Stefan Stoll. *EPR Spectroscopy: Fundamentals and Methods*. eMagRes Books. John Wiley & Sons, Inc., 2018, ISBN=978-1-119-16298-8.

[23] Gunnar Jeschke. Kurze Einführung in die elektronenparamagnetische Resonanzspektroskopie. *University of Konstanz*, 2008 [Date:23.05.2019]. URL: http://www.epr.ethz.ch/content/dam/ethz/special-interest/chab/physical-chemistry/epr-dam/documents/basicEducation/skripts/epr2007.pdf.

[24] Pieter Zeeman. The Effect of Magnetisation on the Nature of Light Emitted by a Substance. *Nature*, 55, 1897.

[25] W. Gerlach and O. Stern. Der experimentelle nachweis des magnetischen moments des silberatoms. *Zeitschrift für Physik*, 8(1):110–111, Dec 1922. doi:10.1007/BF01329580.

[26] The MathWorks Incorporation, 2015. Version 8.5.0.197613 (R2015a).

[27] Andreas Sperlich. *Electron Paramagnetic Resonance Spectroscopy of Conjugated Polymers and Fullerenes for Organic Photovoltaics*. Doctoralthesis, Julius-Maximilians Universität Würzburg, 2013.

[28] A. Abragam and B. Bleaney. *Electron Paramagnetic Resonance of Transition Ions*. Oxford Classic Texts in the Physical Sciences. OUP Oxford, 2012, ISBN=9780191023002.

[29] E. M. Purcell. Spontaneous emission probabilities at radio frequencies. *Physical Review*, 69:681, 1946.

[30] J. S. Briggs. A derivation of the time-energy uncertainty relation. *Journal of Physics: Conference Series*, 99:012002, 2008. doi:10.1088/1742-6596/99/1/012002.

[31] Raphael D Levine. *Molecular reaction dynamics and chemical reactivity*. Oxford University Press, USA, 1987.

[32] Gunnar Jeschke. Einführung in die ESR-Spektroskopie. *Johannes-Gutenberg-Universität Mainz & Universität Konstanz*, 1998, 2006 [Date:23.05.2019].

URL: https://www.ethz.ch/content/dam/ethz/special-interest/chab/physical-chemistry/epr-dam/documents/basicEducation/skripts/epr_skript_mainz_1998.pdf.

[33] Charles P. Slichter. *Principles of Magnetic Resonance*. Springer Series in Solid-State Sciences. Springer Berlin Heidelberg, 1990, ISBN=978-3-540-50157-2. doi:10.1007/978-3-662-09441-9.

[34] Dave Barr, Sandra S. Eaton, and Gareth R. Eaton. Workshop on Quantitative EPR. *31st Annual International EPR Symposium*, 2008, [Date:23.02.2016] https://epri.uchicago.edu/sites/epri.uchicago.edu/files/uploads/files/Quantitative

[35] G. R. Eaton, S. S. Eaton, D. P. Barr, and R. T. Weber. *Quantitative EPR*. Springer Berlin Heidelberg, 2010, ISBN=9783211929483.

[36] Wolfgang Brütting. *Physics of Organic Semiconductors*. Springer-Lehrbuch. John Wiley & Sons, Inc., 2006, ISBN=9783527405503.

[37] Wolfgang Krätschmer. *Formation of Fullerenes*, pages 7–29. Springer Netherlands, 2006, ISBN=978-1-4020-4135-8. doi:10.1007/1-4020-4135-7_2.

[38] A J Page, F Ding, S Irle, and K Morokuma. Insights into carbon nanotube and graphene formation mechanisms from molecular simulations: a review. *Reports on Progress in Physics*, 78(3):036501, feb 2015. doi:10.1088/0034-4885/78/3/036501.

[39] Ingolf V. Hertel and Claus-Peter Schulz. *Atome, Moleküle und optische Physik 2*. Springer-Lehrbuch. Springer Berlin Heidelberg, 2010, ISBN=978-3-642-11972-9. doi:10.1007/978-3-642-11973-6.

[40] Hermann Haken and Hans Christoph Wolf. *Molekülphysik und Quantenchemie*. Springer-Lehrbuch. Springer Berlin Heidelberg, 2003, ISBN=978-3-662-08827-2. doi:10.1007/978-3-662-08826-5.

[41] Inc. PerkinElmer Informatics, 2018. Version 18.0.

[42] Timothy M. Swager. 50th anniversary perspective: Conducting/semiconducting conjugated polymers. a personal perspective on the past and the future. *Macromolecules*, 50(13):4867–4886, 2017. doi:10.1021/acs.macromol.7b00582.

[43] Marcus Böckmann, Thomas Schemme, Djurre H. de Jong, Cornelia Denz, Andreas Heuer, and Nikos L. Doltsinis. Structure of p3ht crystals, thin films, and

solutions by uv/vis spectral analysis. *Phys. Chem. Chem. Phys.*, 17:28616–28625, 2015. doi:10.1039/C5CP03665H.

[44] Wolfram Koch and Max C. Holthausen. *A Chemist's Guide to Density Functional Theory*. John Wiley & Sons, Inc., 2001, ISBN=3-527-30422-3.

[45] Tatyana E. Shubina, Dmitry I. Sharapa, Christina Schubert, Dirk Zahn, Marcus Halik, Paul A. Keller, Stephen G. Pyne, Sreenu Jennepalli, Dirk M. Guldi, and Timothy Clark. Fullerene van der waals oligomers as electron traps. *Journal of the American Chemical Society*, 136(31):10890–10893, 2014. doi:10.1021/ja505949m.

[46] R. Saito, M. Fujita, G. Dresselhaus, and M. S Dresselhaus. Electronic structure of chiral graphene tubules. *Applied Physics Letters*, 60(18):2204–2206, 1992. doi:10.1063/1.107080.

[47] C. Journet, W. K. Maser, P. Bernier, A. Loiseau, M. Lamy de la Chapelle, S. Lefrant, P. Deniard, R. Lee, and J. E. Fischer. Large-scale production of single-walled carbon nanotubes by the electric-arc technique. *Nature*, 338, 1997. doi:10.1038/41972.

[48] Andreas Thess, Roland Lee, Pavel Nikolaev, Hongjie Dai, Pierre Petit, Jerome Robert, Chunhui Xu, Young Hee Lee, Seong Gon Kim, Andrew G. Rinzler, Daniel T. Colbert, Gustavo E. Scuseria, David Tománek, John E. Fischer, and Richard E. Smalley. Crystalline Ropes of Metallic Carbon Nanotubes. *Science*, 273, 1996. doi:10.1126/science.273.5274.483.

[49] Gene Dresselhaus, Mildred S. Dresselhaus, and Riichiro Saito. *Physical Properties Of Carbon Nanotubes*. World Scientific Publishing Company, 1998, ISBN=9781783262410. URL: https://books.google.de/books?id=fv63CgAAQBAJ, doi:10.1142/9781860943799_0003.

[50] Dodd Gray, Adam McCaughan, and Bhaskar Mookerji. Crystal Structure of Graphite, Graphene and Silicon. *Lecture, Massachusetts Institute of Technology, Cambridge, MA*, 2009, [Date:23.02.2016] http://community.wvu.edu/ miholcomb/graphene.pdf.

[51] C. L. Kane and E. J. Mele. Quantum Spin Hall Effect in Graphene. *Physical Review Letters*, 95(22):226801, 2005. doi:10.1103/PhysRevLett.95.226801.

[52] Supriyo Datta. *Electronic Transport in Mesoscopic Systems*. Cambridge University Press, 1997, ISBN=9780521599436.

[53] Christine M. Isborn, Chun Tang, Ashlie Marini, Erin R. Johnson, Alberto Otero-de-la Roza, and Vincent C. Tung. Carbon Nanotube Chirality Determines Efficiency of Electron Transfer to Fullerene in All-Carbon Photovoltaics. *The Journal of Physical Chemistry Letters*, 2013. doi:10.1021/jz401369s.

[54] Josh M. Holt, Andrew J. Ferguson, Nikos Kopidakis, Brian A. Larsen, Justin Bult, Garry Rumbles, and Jeffrey L. Blackburn. Prolonging charge separation in P3HT-SWNT composites using highly enriched semiconducting nanotubes. *Nano Letters*, 10:4627–4633, 2010. doi:10.1021/nl102753z.

[55] Ge. G. Samsonidze, A R. Saito, D A. Jorio, E M. A. Pimenta, E A. G. Souza Filho, F A. Grüneis, D G. Dresselhaus, and M. S. Dresselhausa. The concept of cutting lines in carbon nanotube science. *Journal of Nanoscience and Nanotechnology*, 3(6):431–458, 2003. doi:doi:10.1166/jnn.2003.231.

[56] Eduardo B. Barros, Ado Jorio, Georgii G. Samsonidze, Rodrigo B. Capaz, Antônio G. Souza Filho, Josué Mendes Filho, Gene Dresselhaus, and Mildred S. Dresselhaus. Review on the symmetry-related properties of carbon nanotubes. *Physics Reports*, 431(6):261 – 302, 2006. doi:10.1016/j.physrep.2006.05.007.

[57] Tayebeh Ameri, Gilles Dennler, Christoph Lungenschmied, and Christoph J. Brabec. Organic tandem solar cells: A review. *Energy Environ. Sci.*, 2:347–363, 2009. doi:10.1039/B817952B.

[58] Andreas Sperlich. *Elektronenspinresonanz-Untersuchungen an Polymerhalbleitern und ihren Blends*. Diploma thesis, Julius-Maximilians Universität Würzburg, 2007.

[59] Hideki Shirakawa, Edwin J. Louis, Alan G. MacDiarmid, Chwan K. Chiang, and Alan J. Heeger. Synthesis of electrically conducting organic polymers: halogen derivatives of polyacetylene, (ch). *J. Chem. Soc., Chem. Commun.*, pages 578–580, 1977. doi:10.1039/C39770000578.

[60] C. W. Tang. Two-layer organic photovoltaic cell. *Applied Physics Letters*, 48(2):183–185, 1986. doi:10.1063/1.96937.

[61] Yakov Frenkel. *Wave Mechanics. Elementary Theory*. Clarendon Press, Oxford, 1932.

[62] Sarah R. Cowan, Anshuman Roy, and Alan J. Heeger. Recombination in polymer-fullerene bulk heterojunction solar cells. *Phys. Rev. B*, 82:245207, Dec 2010. doi:10.1103/PhysRevB.82.245207.

[63] Stefan Väth. *On the Role of Spin States in Organic Semiconductor Devices*. Doctoralthesis, Julius-Maximilians Universität Würzburg, 2016.

[64] Zuo Xiao, Xue Jia, and Liming Ding. Ternary organic solar cells offer 14% power conversion efficiency. *Science Bulletin*, 62(23):1562 – 1564, 2017. doi:10.1016/j.scib.2017.11.003.

[65] Lingxian Meng, Yamin Zhang, Xiangjian Wan, Chenxi Li, Xin Zhang, Yanbo Wang, Xin Ke, Zuo Xiao, Liming Ding, Ruoxi Xia, Hin-Lap Yip, Yong Cao, and Yongsheng Chen. Organic and solution-processed tandem solar cells with 17.3% efficiency. *Science*, 361(6407):1094–1098, 2018. doi:10.1126/science.aat2612.

[66] René A. J. Janssen and Jenny Nelson. Factors limiting device efficiency in organic photovoltaics. *Advanced Materials*, 25(13):1847–1858, 2013. doi:10.1002/adma.201202873.

[67] Fujun Zhang, Zuliang Zhuo, Jian Zhang, Xin Wang, Xiaowei Xu, Zixuan Wang, Yusheng Xin, Jian Wang, Jin Wang, Weihua Tang, Zheng Xu, and Yongsheng Wang. Influence of pc60bm or pc70bm as electron acceptor on the performance of polymer solar cells. *Solar Energy Materials and Solar Cells*, 97:71 – 77, 2012. Dedicated to the Global Organic Photovoltaics (GOPV) conference in Hangzhou, China. doi:10.1016/j.solmat.2011.09.006.

[68] Martin Schwarze, Wolfgang Tress, Beatrice Beyer, Feng Gao, Reinhard Scholz, Carl Poelking, Katrin Ortstein, Alrun A. Günther, Daniel Kasemann, Denis Andrienko, and Karl Leo. Band structure engineering in organic semiconductors. *Science*, 352(6292):1446–1449, 2016. doi:10.1126/science.aaf0590.

[69] N. Felekidis, E. Wang, and M. Kemerink. Open circuit voltage and efficiency in ternary organic photovoltaic blends. *Energy Environ. Sci.*, 9:257–266, 2016. doi:10.1039/C5EE03095A.

[70] Sonya A. Mollinger, Koen Vandewal, and Alberto Salleo. Microstructural and electronic origins of open-circuit voltage tuning in organic solar cells based on ternary blends. *Advanced Energy Materials*, 5(23):1501335, 2015. doi:10.1002/aenm.201501335.

[71] Sean Sweetnam, Rohit Prasanna, Timothy M. Burke, Jonathan A. Bartelt, and Michael D. McGehee. How the energetic landscape in the mixed phase of organic bulk heterojunction solar cells evolves with fullerene content. *The Journal of Physical Chemistry C*, 120(12):6427–6434, 2016. doi:10.1021/acs.jpcc.6b00753.

[72] Carl Poelking, Max Tietze, Chris Elschner, Selina Olthof, Dirk Hertel, Björn Baumeier, Frank Würthner, Klaus Meerholz, Karl Leo, and Denis Andrienko. Impact of mesoscale order on open-circuit voltage in organic solar cells. *Nature Materials*, 14:434–439, 2014. doi:10.1038/nmat4167.

[73] Koen Vandewal, Steve Albrecht, Eric T. Hoke, Kenneth R. Graham, Johannes Widmer, Jessica D. Douglas, Marcel Schubert, William R. Mateker, Jason T. Bloking, George F. Burkhard, Alan Sellinger, Jean M. J. Fréchet, Aram Amassian, Moritz K. Riede, Michael D. McGehee, Dieter Neher, and Alberto Salleo. Efficient charge generation by relaxed charge-transfer states at organic interfaces. *Nature Materials*, 13:63–68, 2014. doi:10.1038/NMAT3807.

[74] Incorporation American Dye Source. Products Catalog 2019. [Date:24.05.2019] https://adsdyes.com/products, 2019.

[75] Sigma-Aldrich. Products. product catalogue, [Date: 20.05.2019] Link:http://www.sigmaaldrich.com/technical-service-home/product-catalog.html, 2019.

[76] A. C. Duerr. *Growth and Structure of DIP Thin-Films and Au Contacts on DIP Thin-Films*. Doctoralthesis, Universität Stuttgart, 2002.

[77] J. Wagner, M. Gruber, A. Hinderhofer, A. Wilke, B. Broeker, J. Frisch, P. Amsalem, A. Vollmer, A. Opitz, N. Koch, F. Schreiber, and W. Bruetting. High fill factor and open circuit voltage in organic photovoltaic cells with diindenoperylene as donor material. *Advanced Functional Materials*, 20(24), 2010. doi:10.1002/adfm.201001028.

[78] J.H. Weaver. Electronic structures of c60, c70 and the fullerides: Photoemission and inverse photoemission studies. *Journal of Physics and Chemistry of Solids*, 53(11):1433 – 1447, 1992. doi:10.1016/0022-3697(92)90237-8.

[79] Andrew Skumanich. Optical absorption spectra of carbon 60 thin films from 0.4 to 6.2 eV. *Chemical Physics Letters*, 5(182), 1991. doi:10.1016/0009-2614(91)90112-M.

[80] Bo-ying Han, K. Hevesi, Li-ming Yu, G. Gensterblum, P. Rudolf, J.-J. Pireaux, P. A. Thiry, and R. Caudano. Electronic transitions and excitations in solid c70 studied by reflection electron energy loss spectroscopy. *Journal of Vacuum Science & Technology A*, 13(3):1606–1608, 1995. doi:10.1116/1.579736.

[81] Wei-ya Zhou, Si-shen Xie, Sheng-fa Qian, Tang Zhou, Ri-an Zhao, Gang Wang, Lu-xi Qian, and Wen-zhi Li. Optical absorption spectra of C70 thin films. *Journal of Applied Physics*, 80(182), 1996. doi:10.1063/1.362747.

[82] Youjun He and Yongfang Li. Fullerene derivative acceptors for high performance polymer solar cells. *Phys. Chem. Chem. Phys.*, 13:1970–1983, 2011. doi:10.1039/C0CP01178A.

[83] Erik Busby, Christopher W. Rochester, Adam J. Moulé, and Delmar S. Larsen. Acceptor dependent polaron recombination dynamics in poly 3-hexyl thiophene: Fullerene composite films. *Chemical Physics Letters*, 513(1):77 – 83, 2011. doi:10.1016/j.cplett.2011.07.066.

[84] Pei Cheng, Yongfang Li, and Xiaowei Zhan. Efficient ternary blend polymer solar cells with indene-c60 bisadduct as an electron-cascade acceptor. *Energy Environ. Sci.*, 7:2005–2011, 2014. doi:10.1039/C3EE44202K.

[85] J. G. Sánchez, J. Ferré-Borrull, L. F. Marsal, J. Pallarès, V. S. Balderrama, and M. Estrada. Performance comparison of bhj organic solar cells based on p3ht with pc70bm and icba. In *2015 IEEE International Autumn Meeting on Power, Electronics and Computing (ROPEC)*, pages 1–4, Nov 2015. doi:10.1109/ROPEC.2015.7395132.

[86] Chun-Qi Sheng, Peng Wang, Ying Shen, Wen-Jie Li, Wen-Hua Zhang, Jun-Fa Zhu, Guo-Qiao Lai, and Hong-Nian Li. Electronic states of IC60ba and PC71bm. *Chinese Physics Letters*, 30(11):117103, nov 2013. doi:10.1088/0256-307x/30/11/117103.

[87] Youjun He, Hsiang-Yu Chen, Jianhui Hou, and Yongfang Li. Indene-c60 bisadduct: A new acceptor for high-performance polymer solar cells. *Journal of the American Chemical Society*, 132(4):1377–1382, 2010. doi:10.1021/ja908602j.

[88] Zhan'ao Tan, Deping Qian, Wenqing Zhang, Liangjie Li, Yuqin Ding, Qi Xu, Fuzhi Wang, and Yongfang Li. Efficient and stable polymer solar cells with solution-processed molybdenum oxide interfacial layer. *J. Mater. Chem. A*, 1:657–664, 2013. doi:10.1039/C2TA00325B.

[89] Chang-Zhi Li, Hin-Lap Yip, and Alex K.-Y. Jen. Functional fullerenes for organic photovoltaics. *J. Mater. Chem.*, 22:4161–4177, 2012. doi:10.1039/C2JM15126J.

[90] Yongfang Li. Fullerene-bisadduct acceptors for polymer solar cells. *Chemistry – An Asian Journal*, 8(10):2316–2328, 2013. doi:10.1002/asia.201300600.

[91] Yifan Yang, Francisco Arias, Luis Echegoyen, L. P. Felipe Chibante, Scott Flanagan, Andrew Robertson, and Lon J. Wilson. Reversible fullerene electrochemistry: Correlation with the homo-lumo energy difference for c60, c70, c76, c78, and c84. *Journal of the American Chemical Society*, 117(29):7801–7804, 1995. doi:10.1021/ja00134a027.

[92] Henry. Ajie, Marcos M. Alvarez, Samir J. Anz, Rainer D. Beck, Francois. Diederich, K. Fostiropoulos, Donald R. Huffman, Wolfgang. Kraetschmer, Yves. Rubin, and . et al. Characterization of the soluble all-carbon molecules c60 and c70. *The Journal of Physical Chemistry*, 94(24):8630–8633, 1990. doi:10.1021/j100387a004.

[93] Michael Brendel. *Correlation between Interface Energetics of Molecular Semiconductors and Opto-Electronic Properties of Planar Organic Solar Cells*. Doctoralthesis, Julius-Maximilians Universität Würzburg, 2017.

[94] A. Foertig, A. Baumann, D. Rauh, V. Dyakonov, and C. Deibel. Charge carrier concentration and temperature dependent recombination in polymer-fullerene solar cells. *Applied Physics Letters*, 95(5):052104, 2009. doi:10.1063/1.3202389.

[95] Oleg G. Poluektov, Salvatore Filippone, Nazario Martín, Andreas Sperlich, Carsten Deibel, and Vladimir Dyakonov. Spin signatures of photogenerated radical anions in polymer-[70]fullerene bulk heterojunctions: High frequency pulsed epr spectroscopy. *The Journal of Physical Chemistry B*, 114(45):14426–14429, 2010. doi:10.1021/jp1012347.

[96] Oleg G. Poluektov, Jens Niklas, Kristy L. Mardis, Serge Beaupré, Mario Lexlerc, Carmen Villegas, Sule Erten-Ela, Juan L. Delgado, Nazario Martin, Andreas Sperlich, and Vladimir Dyakonov. Electronic Structure of Fulleren Heterodimer in Bulk-Heterojunction Blends. *Advanced Energy Materials*, 2014. doi:10.1002/aenm.201301517.

[97] A. Konkin, H.-K. Roth, P. Scharff, A. Aganov, O. Ambacher, and S. Sensfuss. K-band esr studies of structural anisotropy in p3ht and p3ht/pcbm blend polymer solid films: Paramagnetic defects after continuous wave xe-lamp photolysis. *Solid State Communications*, 149(21):893 – 897, 2009. doi:10.1016/j.ssc.2009.01.034.

[98] PM Allemand, G Srdanov, A Koch, K Khemani, F Wudl, Y Rubin, F Diederich, MM Alvarez, SJ Anz, and RL Whetten. The unusual electron spin resonance of fullerene c60 anion radical. *Journal of the American Chemical Society*, 113(7):2780–2781, 1991.

[99] Stephen G. Kukolich and Donald R. Huffman. Epr spectra of c60 anion and cation radicals. *Chemical Physics Letters*, 182(3):263 – 265, 1991. doi:10.1016/0009-2614(91)80212-G.

[100] Jens Niklas, Kristy L. Mardis, and Oleg G. Poluektov. Spin signature of the c60 fullerene anion: A combined x- and d-band epr and dft study. *The Journal of Physical Chemistry Letters*, 9(14):3915–3921, 2018. doi:10.1021/acs.jpclett.8b01613.

[101] Dominique Dubois, Karl M. Kadish, Scott Flanagan, R. E. Haufler, L. P. F. Chibante, and Lon J. Wilson. Spectroelectrochemical study of the c60 and c70 fullerenes and their mono-, di-, tri- and tetraanions. *Journal of the American Chemical Society*, 113(11):4364–4366, 1991. doi:10.1021/ja00011a069.

[102] Frank J. Adrian. Spin-orbit effects in fullerenes. *Chemical Physics*, 211(1):73 – 80, 1996. doi:10.1016/0301-0104(96)00243-1.

[103] John Stinchcombe, Alain Penicaud, P. Bhyrappa, Peter D. W. Boyd, and Christopher A. Reed. Buckminsterfulleride(1-) salts: synthesis, epr, and the jahn-teller distortion of c60-. *Journal of the American Chemical Society*, 115(12):5212–5217, 1993. doi:10.1021/ja00065a037.

[104] Victor I. Krinichnyi and Eugenia I. Yudanova. Light-induced epr study of charge transfer in p3ht/bis-pcbm bulk heterojunctions. *AIP Advances*, 1(2):022131, 2011. doi:10.1063/1.3599411.

[105] Madhu Menon, K. R. Subbaswamy, and Majid Sawtarie. Structure and properties of c_{60} dimers by generalized tight-binding molecular dynamics. *Phys. Rev. B*, 49:13966–13969, May 1994. doi:10.1103/PhysRevB.49.13966.

[106] Artem A. Bakulin, Akshay Rao, Vlad G. Pavelyev, Paul H. M. van Loosdrecht, Maxim S. Pshenichnikov, Dorota Niedzialek, Jérôme Cornil, David Beljonne, and Richard H. Friend. The role of driving energy and delocalized states for charge separation in organic semiconductors. *Science*, 335(6074):1340–1344, 2012. doi:10.1126/science.1217745.

[107] SA Brazovskii and NN Kirova. Excitons, polarons, and bipolarons in conducting polymers. *JETP lett*, 33(4), 1981.

[108] Petr P. Khlyabich, Beate Burkhart, Andrey E. Rudenko, and Barry C. Thompson. Optimization and simplification of polymer–fullerene solar cells through polymer and active layer design. *Polymer*, 54(20):5267 – 5298, 2013. doi:10.1016/j.polymer.2013.07.053.

[109] Koen Vandewal, Kristofer Tvingstedt, Abay Gadisa, Olle Inganäs, and Jean V. Manca. Relating the open-circuit voltage to interface molecular properties of donor:acceptor bulk heterojunction solar cells. *Phys. Rev. B*, 81:125204, Mar 2010. doi:10.1103/PhysRevB.81.125204.

[110] Koen Vandewal, Kristofer Tvingstedt, Abay Gadisa, Olle Ingan´as, and Jean V. Manca. On the origin of the open-circuit voltage of polymer–fullerene solar cells. *Nature Materials*, 8:904—909, November 2009. doi:10.1038/NMAT2548.

[111] M. Dolores Perez, Carsten Borek, Stephen R. Forrest, and Mark E. Thompson. Molecular and morphological influences on the open circuit voltages of organic photovoltaic devices. *Journal of the American Chemical Society*, 131(26):9281–9286, 2009. doi:10.1021/ja9007722.

[112] Dechan Angmo, Morten Bjerring, Niels Chr. Nielsen, Barry C. Thompson, and Frederik C. Krebs. Fullerene alloy formation and the benefits for efficient printing of ternary blend organic solar cells. *J. Mater. Chem. C*, 3:5541–5548, 2015. doi:10.1039/C5TC00781J.

[113] M. Olguin, L. Basurto, R. R. Zope, and T. Baruah. Substituent-level tuning of frontier orbital energy levels in phthalocyanine/c60 donor-acceptor charge transfer pairs. *arXiv e-prints*, August 2013. URL: https://arxiv.org/abs/1308.2001, arXiv:1308.2001.

[114] Petr P. Khlyabich, Beate Burkhart, and Barry C. Thompson. Efficient ternary blend bulk heterojunction solar cells with tunable open-circuit voltage. *Journal of the American Chemical Society*, 133(37):14534–14537, 2011. doi:10.1021/ja205977z.

[115] Tracey M. Clarke and James R. Durrant. Charge photogeneration in organic solar cells. *Chemical Reviews*, 110(11):6736–6767, 2010. doi:10.1021/cr900271s.

[116] Guoqiang Ren, Cody W. Schlenker, Eilaf Ahmed, Selvam Subramaniyan, Selina Olthof, Antoine Kahn, David S. Ginger, and Samson A. Jenekhe. Photoinduced

hole transfer becomes suppressed with diminished driving force in polymer-fullerene solar cells while electron transfer remains active. *Advanced Functional Materials*, 23(10):1238–1249, 2013. doi:10.1002/adfm.201201470.

[117] Hyunbum Kang, Ki-Hyun Kim, Tae Eui Kang, Chul-Hee Cho, Sunhee Park, Sung Cheol Yoon, and Bumjoon J. Kim. Effect of fullerene tris-adducts on the photovoltaic performance of p3ht:fullerene ternary blends. *ACS Applied Materials & Interfaces*, 5(10):4401–4408, 2013. doi:10.1021/am400695e.

[118] Fortunato Piersimoni, Sylvain Chambon, Koen Vandewal, Raoul Mens, Tine Boonen, Abay Gadisa, Marta Izquierdo, Salvatore Filippone, Bart Ruttens, Jan D'Haen, Nazario Martin, Laurence Lutsen, Dirk Vanderzande, Peter Adriaensens, and Jean V. Manca. Influence of fullerene ordering on the energy of the charge-transfer state and open-circuit voltage in polymer:fullerene solar cells. *The Journal of Physical Chemistry C*, 115(21):10873–10880, 2011. doi:10.1021/jp110982m.

[119] Akshay Rao, Akshay Rao, Philip C Y Chow, Simon Gélinas, Cody W Schlenker, Chang-Zhi Li, Hin-Lap Yip, Alex K-Y Jen, David S Ginger, and Richard H Friend. The role of spin in the kinetic control of recombination in organic photovoltaics. *Nature*, 500(7463):435—439, August 2013. doi:10.1038/nature12339.

[120] Robert A. Street, Daniel Davies, Petr P. Khlyabich, Beate Burkhart, and Barry C. Thompson. Origin of the tunable open-circuit voltage in ternary blend bulk heterojunction organic solar cells. *Journal of the American Chemical Society*, 135(3):986–989, 2013. doi:10.1021/ja3112143.

[121] Fiona C. Jamieson, Ester Buchaca Domingo, Thomas McCarthy-Ward, Martin Heeney, Natalie Stingelin, and James R. Durrant. Fullerene crystallisation as a key driver of charge separation in polymer/fullerene bulk heterojunction solar cells. *Chem. Sci.*, 3:485–492, 2012. doi:10.1039/C1SC00674F.

[122] Charlotte Brückner, Frank Würthner, Klaus Meerholz, and Bernd Engels. Structure–property relationships from atomistic multiscale simulations of the relevant processes in organic solar cells. i. thermodynamic aspects. *The Journal of Physical Chemistry C*, 121(1):4–25, 2017. doi:10.1021/acs.jpcc.6b06755.

[123] Charlotte Brückner, Frank Würthner, Klaus Meerholz, and Bernd Engels. Atomistic approach to simulate processes relevant for the efficiencies of organic solar cells as a function of molecular properties. ii. kinetic aspects. *The Journal of Physical Chemistry C*, 121(1):26–51, 2017. doi:10.1021/acs.jpcc.6b11340.

[124] Florian Späth. *Präparation und Charakterisierung einwandiger Kohlenstoffnanorohr-Polyfluoren-Komplexe*. Doctoralthesis, Julius-Maximilians Universität Würzburg, 2015.

[125] Hiroaki Ozawa, Natsuko Ide, Tsuyohiko Fujigaya, Yasuro Niidome, and Naotoshi Nakashima. One-pot separation of highly enriched (6,5)-single-walled carbon nanotubes using a fluorene-based copolymer. *Chemistry Letters*, 40(3):239–241, 2011. doi:10.1246/cl.2011.239.

[126] Widianta Gomulya, Jia Gao, and Maria Antonietta Loi. Conjugated polymer-wrapped carbon nanotubes: physical properties and device applications. *The European Physical Journal B*, 86(10):404, 2013. doi:10.1140/epjb/e2013-40707-9.

[127] Tobias Hertel, Sabine Himmelein, Thomas Ackermann, Dominik Stich, and Jared Crochet. Diffusion limited photoluminescence quantum yields in 1-d semiconductors: Single-wall carbon nanotubes. *ACS Nano*, 4(12):7161–7168, 2010. doi:10.1021/nn101612b.

[128] Arko Graf, Yuriy Zakharko, Stefan P. Schießl, Claudia Backes, Moritz Pfohl, Benjamin S. Flavel, and Jana Zaumseil. Large scale, selective dispersion of long single-walled carbon nanotubes with high photoluminescence quantum yield by shear force mixing. *Carbon*, 106:593–599, 2016. doi:10.1016/j.carbon.2016.05.002.

[129] Shinichiro Mouri, Yuhei Miyauchi, and Kazunari Matsuda. Dispersion-process effects on the photoluminescence quantum yields of single-walled carbon nanotubes dispersed using aromatic polymers. *The Journal of Physical Chemistry C*, 116(18):10282–10286, 2012. doi:10.1021/jp212040y.

[130] Benjamin S. Flavel, Katherine E. Moore, Moritz Pfohl, Manfred M. Kappes, and Frank Hennrich. Separation of single-walled carbon nanotubes with a gel permeation chromatography system. *ACS Nano*, 8(2):1817–1826, 2014. doi:10.1021/nn4062116.

[131] Anton V. Naumov, Dmitri A. Tsyboulski, Sergei M. Bachilo, and Bruce R. Weisman. Length-dependent optical properties of single-walled carbon nanotube samples. *Chemical Physics*, 422:255 – 263, 2013. doi:10.1016/j.chemphys.2012.12.033.

[132] Friedrich Eugen Schöppler. *Photolumineszenzmikroskopie und-spektroskopie halbleitender Kohlenstoffnanoröhren*. Doctoralthesis, Universität Würzburg, 2012.

[133] Holger Hartleb, Florian Späth, and Tobias Hertel. Evidence for Strong Electronic Correlations in the Spectra of Gate-Doped Single-Wall Carbon Nanotubes. *ACS Nano*, 9(10):10461–10470, 2015. doi:10.1021/acsnano.5b04707.

[134] Klaus H. Eckstein, Holger Hartleb, Melanie M. Achsnich, Friedrich Schöppler, and Tobias Hertel. Localized Charges Control Exciton Energetics and Energy Dissipation in Doped Carbon Nanotubes. *ACS Nano*, 11(10):10401–10408, 2017. doi:10.1021/acsnano.7b05543.

[135] Taishi Nishihara, Yasuhiro Yamada, and Yoshihiko Kanemitsu. Dynamics of exciton-hole recombination in hole-doped single-walled carbon nanotubes. *Phys. Rev. B*, 86:075449, Aug 2012. doi:10.1103/PhysRevB.86.075449.

[136] Yusong Bai, Jean-Hubert Olivier, George Bullard, Chaoren Liu, and Michael J. Therien. Dynamics of charged excitons in electronically and morphologically homogeneous single-walled carbon nanotubes. *Proceedings of the National Academy of Sciences*, page 201712971, 2018. doi:10.1073/pnas.1712971115.

[137] Takeshi Koyama, Satoru Shimizu, Yasumitsu Miyata, Hisanori Shinohara, and Arao Nakamura. Ultrafast formation and decay dynamics of trions in p-doped single-walled carbon nanotubes. *Phys. Rev. B*, 87:165430, Apr 2013. doi:10.1103/PhysRevB.87.165430.

[138] Michael J. O'Connell, Ezra E. Eibergen, and Stephen K. Doorn. Chiral selectivity in the charge-transfer bleaching of single-walled carbon-nanotube spectra. *Nature Materials*, pages 412–418, 2005. doi:10.1038/nmat1367.

[139] Mathias Steiner, Marcus Freitag, Vasili Perebeinos, Anton Naumov, Joshua P. Small, Ageeth A. Bol, and Phaedon Avouris. Gate-variable light absorption and emission in a semiconducting carbon nanotube. *Nano Letters*, 9(10):3477–3481, 2009. doi:10.1021/nl9016804.

[140] Philip G. Collins, Keith Bradley, Masa Ishigami, and A Zettl. Extreme Oxygen Sensitivity of Electronic Properties of Carbon Nanotubes. *Science*, 287(5459):1801–1804, mar 2000. doi:10.1126/science.287.5459.1801.

[141] Kevin R. Moonoosawmy and Peter Kruse. Cause and consequence of carbon nanotube doping in water and aqueous media. *Journal of the American Chemical Society*, 132(5):1572–1577, 2010. doi:10.1021/ja906820n.

[142] Carla M. Aguirre, Pierre L. Levesque, Matthieu Paillet, Francois Lapinte, Benoit C. St-Antoine, Patrick Desjardins, and Richard Martel. The Role of the Oxygen/Water Redox Couple in Suppressing Electron Conduction in Field-Effect Transistors. *Advanced Energy Materials*, 2009. doi:10.1002/aenm.200900550.

[143] Gordana Dukovic, Brian E. White, Zhiyong Zhou, Feng Wang, Steffen Jockusch, Michael L. Steigerwald, Tony F. Heinz, Richard A. Friesner, Nicholas J. Turro, and Louis E. Brus. Reversible surface oxidation and efficient luminescence quenching in semiconductor single-wall carbon nanotubes. *Journal of the American Chemical Society*, 126(46):15269–15276, 2004. doi:10.1021/ja046526r.

[144] Ming Zheng and Bruce A. Diner. Solution redox chemistry of carbon nanotubes. *Journal of the American Chemical Society*, 126(47):15490–15494, 2004. doi:10.1021/ja0457967.

[145] Brian A. Gregg, Si-Guang Chen, and Russell A. Cormier. Coulomb forces and doping in organic semiconductors. *Chemistry of Materials*, 16(23):4586–4599, 2004. doi:10.1021/cm049625c.

[146] Silvia M. Santos, Bertrand Yuma, Stéphane Berciaud, Jonah Shaver, Mathieu Gallart, Pierre Gilliot, Laurent Cognet, and Brahim Lounis. All-optical trion generation in single-walled carbon nanotubes. *Phys. Rev. Lett.*, 107:187401, Oct 2011. doi:10.1103/PhysRevLett.107.187401.

[147] B. Yuma, S. Berciaud, J. Besbas, J. Shaver, S. Santos, S. Ghosh, R. B. Weisman, L. Cognet, M. Gallart, M. Ziegler, B. Hönerlage, B. Lounis, and P. Gilliot. Biexciton, single carrier, and trion generation dynamics in single-walled carbon nanotubes. *Phys. Rev. B*, 87:205412, May 2013. doi:10.1103/PhysRevB.87.205412.

[148] B. Corzilius, K.-P. Dinse, K. Hata, M. Haluška, V. Skákalová, and S. Roth. Swnt probed by multi-frequency epr and nonresonant microwave absorption. *physica status solidi (b)*, 245(10):2251–2254, 2008. doi:10.1002/pssb.200879574.

[149] Jens Niklas, Josh M. Holt, Kevin Mistry, Garry Rumbles, Jeffrey L. Blackburn, and Oleg G. Poluektov. Charge Separation in P3HT:SWCNT Blends Studied by EPR: Spin Signature of the Photoinduced Charged State in SWCNT. *The Journal of Physical Chemistry Letters*, 5(3):601–606, feb 2014. doi:10.1021/jz402668h.

[150] William D. Rice, Ralph T. Weber, Ashley D. Leonard, James M. Tour, Pavel Nikolaev, Sivaram Arepalli, Vladimir Berka, Ah-Lim Tsai, and Junichiro Kono. Enhancement of the electron spin resonance of single-walled carbon nanotubes by oxygen removal. *ACS Nano*, 6(3):2165–2173, 2012. doi:10.1021/nn204094s.

[151] Mujtaba Zaka, Yasuhiro Ito, Huiliang Wang, Wenjing Yan, Alex Robertson, Yimin A. Wu, Mark H. Rümmeli, David Staunton, Takeshi Hashimoto, John J. L. Morton, Arzhang Ardavan, G. Andrew D. Briggs, and Jamie H. Warner. Electron paramagnetic resonance investigation of purified catalyst-free single-walled carbon nanotubes. *ACS Nano*, 4(12):7708–7716, 2010. doi:10.1021/nn102602a.

[152] Y Chen, J Chen, H Hu, M.A Hamon, M.E Itkis, and R.C Haddon. Solution-phase epr studies of single-walled carbon nanotubes. *Chemical Physics Letters*, 299(6):532 – 535, 1999. doi:10.1016/S0009-2614(98)01327-X.

[153] David T. Breslin and Marye Anne Fox. Characterization of the excited-state reactivity of a persistent aryl-substituted allyl free radical. *The Journal of Physical Chemistry*, 97(50):13341–13347, 1993. doi:10.1021/j100152a045.

[154] David Griller and Keith U. Ingold. Persistent carbon-centered radicals. *Accounts of Chemical Research*, 9(1):13–19, 1976. doi:10.1021/ar50097a003.

[155] Nagao Azuma, Takehiro Ozawa, and Jun Yamauchi. Molecular and crystal structures of complexes of stable free radical bdpa with benzene and acetone. *Bulletin of the Chemical Society of Japan*, 67(1):31–38, 1994. doi:10.1246/bcsj.67.31.

[156] Adrian Nish, Jeong-Yuan Hwang, James Doig, and Robin J Nicholas. Highly selective dispersion of single-walled carbon nanotubes using aromatic polymers. *Nature nanotechnology*, 2(10):640, 2007. doi:10.1038/nnano.2007.290.

[157] Frank Hennrich, Ralph Krupke, Katharina Arnold, Jan A. Rojas Stütz, Sergei Lebedkin, Thomas Koch, Thomas Schimmel, and Manfred M. Kappes. The mechanism of cavitation-induced scission of single-walled carbon nanotubes. *The Journal of Physical Chemistry B*, 111(8):1932–1937, 2007. doi:10.1021/jp065262n.

[158] Tonya K. Cherukuri, Dmitri A. Tsyboulski, and R. Bruce Weisman. Length- and defect-dependent fluorescence efficiencies of individual single-walled carbon nanotubes. *ACS Nano*, 6(1):843–850, 2012. doi:10.1021/nn2043516.

[159] Andreas Sperlich, Hannes Kraus, Carsten Deibel, Hubert Blok, Jan Schmidt, and Vladimir Dyakonov. Reversible and Irreversible Interactions of Poly (3-hexylthiophene) with Oxygen Studied by Spin-Sensitive Methods. *Physical Chemistry B*, 115:13513–13518, 2011. doi:10.1021/jp2077215.

[160] Yasuhiko Hirana, Gergely Juhasz, Yuhei Miyauchi, Shinichiro Mouri, Kazunari Matsuda, and Naotoshi Nakashima. Empirical Prediction of Electronic Potentials of Single-Walled Carbon Nanotubes With a Specific Chirality (n,m). *Scientific Reports*, 2013. doi:10.1038/srep02959.

[161] Azure D Avery, Ben H Zhou, Jounghee Lee, Eui-Sup Lee, Elisa M Miller, Rachelle Ihly, Devin Wesenberg, Kevin S Mistry, Sarah L Guillot, Barry L Zink, et al. Tailored semiconducting carbon nanotube networks with enhanced thermoelectric properties. *Nature Energy*, 1(4):16033, 2016. doi:10.1038/nenergy.2016.33.

[162] Jeffrey L. Blackburn, Andrew J. Ferguson, Chungyeon Cho, and Jaime C. Grunlan. Carbon-nanotube-based thermoelectric materials and devices. *Advanced Materials*, 30(11):1704386, 2018. doi:10.1002/adma.201704386.

[163] David Griller and Keith U. Ingold. Photoluminescence imaging of electronic-impurity-induced exciton quenching in single-walled carbon nanotubes. *Nature Nanotechnology*, 7:126–132, 2012. doi:10.1038/nnano.2011.227.

[164] S.M. Kim, K.K. Kim, Y.W. Jo, M.H. Park, S.J. Chae, D.L. Duong, C.W. Yang, J. Kong, and Y.H. Lee. Role of anions in the AuCl3-doping of carbon nanotubes. *ACS Nano*, 5(2):1236–1242, 2011. doi:10.1021/nn1028532.

[165] Ki Kang Kim, Seon-Mi Yoon, Hyeon Ki Park, Hyeon-Jin Shin, Soo Min Kim, Jung Jun Bae, Yan Cui, Jong Min Kim, Jae-Young Choi, and Young Hee Lee. Doping strategy of carbon nanotubes with redox chemistry. *New J. Chem.*, 34:2183–2188, 2010. doi:10.1039/C0NJ00138D.

[166] Ki Kang Kim, Jung Jun Bae, Hyeon Ki Park, Soo Min Kim, Hong-Zhang Geng, Kyung Ah Park, Hyeon-Jin Shin, Seon-Mi Yoon, Anass Benayad, Jae-Young Choi, and Young Hee Lee. Fermi level engineering of single-walled carbon nanotubes by aucl3 doping. *Journal of the American Chemical Society*, 130(38):12757–12761, 2008. doi:10.1021/ja8038689.

[167] Hee Cheul Choi, Moonsub Shim, Sarunya Bangsaruntip, and Hongjie Dai. Spontaneous reduction of metal ions on the sidewalls of carbon nanotubes. *Journal of the American Chemical Society*, 124(31):9058–9059, 2002. doi:10.1021/ja026824t.

[168] M. Concepción Gimeno. *The Chemistry of Gold*. John Wiley & Sons, Ltd, 2009. doi:10.1002/9783527623778.ch1.

[169] Saunab Ghosh, Sergei M Bachilo, A Rebecca, and Kathleen M Beckingham. Oxygen Doping Modifies Near infrared Band Gaps in Fluorescent Single-Walled Carbon Nanotubes. *Science (New York, N.Y.)*, 330(6011):2011, 2010. doi:10.1126/science.1196382.

[170] Josef Michl and Vlasta Bonačić-Koutecký. Biradicals and biradicaloids: a unified view. *Tetrahedron*, 44(24):7559 – 7585, 1988. doi:10.1016/S0040-4020(01)86250-5.

[171] Denis Fichou, Gilles Horowitz, and Francis Garnier. Polaron and bipolaron formation on isolated model thiophene oligomers in solution. *Synthetic Metals*, 39(1):125 – 131, 1990. doi:10.1016/0379-6779(90)90207-2.

[172] Tom J Savenije, Andreas Sperlich, Hannes Kraus, Oleg Poluektov, Martin Heeney, and Vladimir Dyakonov. Observation of bi-polarons in blends of conjugated copolymers and fullerene derivatives. *Phys. Chem.*, 13(37):16579–16584, 2011. doi:10.1039/c1cp21607d.

[173] F. Devreux, F. Genoud, M. Nechtschein, and B. Villeret. Esr investigation of polarons and bipolarons in conducting polymers:: the case of polypyrrole. *Synthetic Metals*, 18(1):89 – 94, 1987. Proceedings of the International Conference of Science and Technology of Synthetic Metals. doi:10.1016/0379-6779(87)90859-9.

[174] Andrea J. Lee, Xiaoyong Wang, Lisa J. Carlson, Julie A. Smyder, Bradford Loesch, Xiaomin Tu, Ming Zheng, and Todd D. Krauss. Bright fluorescence from individual single-walled carbon nanotubes. *Nano Letters*, 11(4):1636–1640, 2011. doi:10.1021/nl200077t.

[175] Patrick Pingel, Malavika Arvind, Lisa Kölln, Robert Steyrleuthner, Felix Kraffert, Jan Behrends, Silvia Janietz, and Dieter Neher. p-type doping of poly(3-hexylthiophene) with the strong lewis acid tris(pentafluorophenyl)borane. *Advanced Electronic Materials*, 2(10):1600204, 2016. doi:10.1002/aelm.201600204.

[176] Shane D. Bergin, Zhenyu Sun, David Rickard, Philip V. Streich, James P. Hamilton, and Jonathan N. Coleman. Multicomponent solubility parameters for single-walled carbon nanotube-solvent mixtures. *ACS Nano*, 3(8):2340–2350, 2009. doi:10.1021/nn900493u.

[177] Qiaohuan Cheng, Sourabhi Debnath, Elizabeth Gregan, and Hugh J. Byrne. Ultrasound-assisted swnts dispersion: Effects of sonication parameters and solvent properties. *The Journal of Physical Chemistry C*, 114(19):8821–8827, 2010. doi:10.1021/jp101431h.

[178] M. Grujicic, G. Cao, and W. N. Roy. Atomistic simulations of the solubilization of single-walled carbon nanotubes in toluene. *Journal of Materials Science*, 39(7):2315–2325, Apr 2004. doi:10.1023/B:JMSC.0000019992.56323.4a.

[179] Zhoufei Yang, Jiarui Tian, Zefang Yin, Chaojie Cui, Weizhong Qian, and Fei Wei. Carbon nanotube- and graphene-based nanomaterials and applications in high-voltage supercapacitor: A review. *Carbon*, 141:467 – 480, 2019. doi:10.1016/j.carbon.2018.10.010.

[180] Laura M. Esteves, Hugo A. Oliveira, and Fabio B. Passos. Carbon nanotubes as catalyst support in chemical vapor deposition reaction: A review. *Journal of Industrial and Engineering Chemistry*, 65:1 – 12, 2018. doi:10.1016/j.jiec.2018.04.012.

[181] Ruiqian Wang, Lijuan Xie, Saima Hameed, Chen Wang, and Yibin Ying. Mechanisms and applications of carbon nanotubes in terahertz devices: A review. *Carbon*, 132:42 – 58, 2018. doi:10.1016/j.carbon.2018.02.005.

[182] Michael F. L. De Volder, Sameh H. Tawfick, Ray H. Baughman, and A. John Hart. Carbon nanotubes: Present and future commercial applications. *Science*, 339(6119):535–539, 2013. doi:10.1126/science.1222453.

[183] Diana Gisell Figueroa del Valle, Giuseppe M. Paternò, Andrea Farina, and Francesco Scotognella. Semiconducting carbon nanotubes in photovoltaic blends: The case of ptb7:pc60bm:(6,5) swnt. *Journal of Applied Physics*, 125(8):083101, 2019. doi:10.1063/1.5086504.

[184] Munkhbayar Batmunkh, Mark J. Biggs, and Joseph G. Shapter. Carbon nanotubes for dye-sensitized solar cells. *Small*, 11(25):2963–2989, 2015. doi:10.1002/smll.201403155.

[185] Michael S Arnold, Jeffrey L Blackburn, Jared J Crochet, Stephen K Doorn, Juan G Duque, Aditya Mohite, and Hagen Telg. Recent developments in the photophysics of single-walled carbon nanotubes for their use as active and passive material elements in thin film photovoltaics. *Physical chemistry chemical physics : PCCP*, 15:14896–918, 2013. doi:10.1039/c3cp52752b.

[186] Bernard Ratier, Jean-Michel Nunzi, Matt Aldissi, Thomas M Kraft, and Erwin Buncel. Organic solar cell materials and active layer designs—improvements with carbon nanotubes: a review. *Polymer International*, 61(3):342–354, 2012. doi:10.1002/pi.3233.

[187] L. El Chaar, L.A. lamont, and N. El Zein. Review of photovoltaic technologies. *Renewable and Sustainable Energy Reviews*, 15(5):2165 – 2175, 2011. doi:10.1016/j.rser.2011.01.004.

[188] Tian An Chen and Reuben D. Rieke. The first regioregular head-to-tail poly(3-hexylthiophene-2,5-diyl) and a regiorandom isopolymer: nickel versus palladium catalysis of 2(5)-bromo-5(2)-(bromozincio)-3-hexylthiophene polymerization. *Journal of the American Chemical Society*, 114(25):10087–10088, 1992. doi:10.1021/ja00051a066.

[189] Friedrich Schöppler, Christoph Mann, Tilman C. Hain, Felix M. Neubauer, Giulia Privitera, Francesco Bonaccorso, Daping Chu, Andrea C. Ferrari, and Tobias Hertel. Molar extinction coefficient of single-wall carbon nanotubes. *The Journal of Physical Chemistry C*, 115(30):14682–14686, 2011. doi:10.1021/jp205289h.

[190] J. Maultzsch, R. Pomraenke, S. Reich, E. Chang, D. Prezzi, A. Ruini, E. Molinari, M. S. Strano, C. Thomsen, and C. Lienau. Exciton binding energies in carbon nanotubes from two-photon photoluminescence. *Phys. Rev. B*, 72:241402, Dec 2005. doi:10.1103/PhysRevB.72.241402.

[191] Vasili Perebeinos, J. Tersoff, and Phaedon Avouris. Scaling of excitons in carbon nanotubes. *Phys. Rev. Lett.*, 92:257402, Jun 2004. doi:10.1103/PhysRevLett.92.257402.

[192] Michael J. O. Connell, Sergei M. Bachilo, Chad B. Huffman, Valerie C. Moore, Michael S. Strano, Erik H. Haroz, Kristy L. Rialon, Peter J. Boul, William H. Noon, Carter Kittrell, Jianpeng Ma, Robert H. Hauge, R. Bruce Weisman, and Richard E. Smalley. Band Gap Fluorescence from Individual Single-Walled Carbon Nanotubes. *Science*, 297:593–597, 2002. doi:10.1126/science.1072631.

[193] Jeroen W. G. Wildöer, Liesbeth C. Venema, Andrew G. Rinzler, Richard E. Smalley, and Cees Dekker. Electronic structure of atomically resolved carbon nanotubes. *Nature*, 391:59–62, 1998. doi:10.1038/34139.

[194] Jan C. Hummelen, Brian W. Knight, F. LePeq, Fred Wudl, Jie Yao, and Charles L. Wilkins. Preparation and characterization of fulleroid and methanofullerene

derivatives. *The Journal of Organic Chemistry*, 60(3):532–538, 1995. doi:10.1021/jo00108a012.

[195] Taojun Zhuang, Xiao-Feng Wang, Takeshi Sano, Ziruo Hong, Yang Yang, and Junji Kido. Fullerene derivatives as electron donor for organic photovoltaic cells. *Applied Physics Letters*, 103(20):203301, 2013. doi:10.1063/1.4830037.

[196] Dipankar Sarkar and N.J. Halas. Dember effect in c60 thin films. *Solid State Communications*, 90(4):261 – 265, 1994. doi:10.1016/0038-1098(94)90472-3.

[197] Thomas D. Anthopoulos, Dago M. de Leeuw, Eugenio Cantatore, Sepas Setayesh, Eduard J. Meijer, Cristina Tanase, Jan C. Hummelen, and Paul W. M. Blom. Organic complementary-like inverters employing methanofullerene-based ambipolar field-effect transistors. *Applied Physics Letters*, 85(18):4205–4207, 2004. doi:10.1063/1.1812577.

[198] E. Frankevich, Y. Maruyama, and H. Ogata. Mobility of charge carriers in vapor-phase grown c60 single crystal. *Chemical Physics Letters*, 214(1):39 – 44, 1993. doi:10.1016/0009-2614(93)85452-T.

[199] Qingshan Xie, Francisco Arias, and Luis Echegoyen. Electrochemically-reversible, single-electron oxidation of c60 and c70. *Journal of the American Chemical Society*, 115(21):9818–9819, 1993. doi:10.1021/ja00074a066.

[200] Christopher A. Reed and Robert D. Bolskar. Discrete fulleride anions and fullerenium cations. *Chemical Reviews*, 100(3):1075–1120, 2000. doi:10.1021/cr980017o.

[201] Jens Niklas, Kristy L. Mardis, Brian P. Banks, Gregory M. Grooms, Andreas Sperlich, Vladimir Dyakonov, Serge Beaupré, Mario Leclerc, Tao Xu, Luping Yu, and Oleg G. Poluektov. Highly-efficient charge separation and polaron delocalization in polymer–fullerene bulk-heterojunctions: a comparative multi-frequency epr and dft study. *Phys. Chem. Chem. Phys.*, 15:9562–9574, 2013. doi:10.1039/C3CP51477C.

[202] Hideto Matsuoka, Shinichi Mizutani, Chika Watanabe, and Seigo Yamauchi. High-frequency epr studies on polymer chain morphology in dip-coated films of poly(3-hexylthiophene)/fullerene bulk-heterojunctions. *Bulletin of the Chemical Society of Japan*, 89(3):378–384, 2016. doi:10.1246/bcsj.20150400.

[203] Ekaterina A. Lukina, Alexander A. Popov, Mikhail N. Uvarov, and Leonid V. Kulik. Out-of-phase electron spin echo studies of light-induced charge-transfer states

in p3ht/pcbm composite. *The Journal of Physical Chemistry B*, 119(43):13543–13548, 2015. doi:10.1021/acs.jpcb.5b02142.

[204] Martin Baumgarten and L Gherghel. Electronic properties of charged fullerenes characterized by epr and vis-nir spectroscopy. *Applied Magnetic Resonance*, 11(2):171–182, 1996. doi:10.1007/BF03162052.

[205] Christina Siedschlag, Heinrich Luftmann, Christian Wolff, and Jochen Mattay. [60] fullerene radical cation: Reactions and mechanism. *Tetrahedron*, 55(25):7805–7818, 1999. doi:10.1016/S0040-4020(99)00395-6.

[206] Shunichi Fukuzumi, Tomoyoshi Suenobu, Tsutomu Urano, and Keiko Tanaka. Formation of c60 radical cation in iron (iii)-exchanged zeolite y. *Chemistry letters*, 26(9):875–876, 1997. doi:10.1246/cl.1997.875.

[207] SS Eaton and GR Eaton. Epr spectra of c 60 anions. *Applied Magnetic Resonance*, 11(2):155–170, 1996. doi:10.1007/BF03162051.

[208] Che Chau Yang and Kuo Chu Hwang. Disproportionation of photoexcited c60. *Journal of the American Chemical Society*, 118(19):4693–4698, 1996. doi:10.1021/ja9526401.

[209] Nobuaki Koga and Keiji Morokuma. Ab initio mo study of the c60 anion radical: the jahn—teller distortion and electronic structure. *Chemical physics letters*, 196(1-2):191–196, 1992. doi:10.1016/0009-2614(92)85952-7.

[210] Robert D Bolskar, Rajeev S Mathur, and Christopher A Reed. Synthesis and isolation of a fullerene carbocation (c76+). *Journal of the American Chemical Society*, 118(51):13093–13094, 1996. doi:10.1021/ja962294n.

[211] Jan Fulara, Michael Jakobi, and John P Maier. Electronic and infrared spectra of c+ 60 and c- 60 in neon and argon matrices. *Chemical physics letters*, 211(2-3):227–234, 1993. doi:10.1016/0009-2614(93)85190-Y.

[212] Hua-Hsien Liao, Chia-Ming Yang, Chien-Cheng Liu, Sheng-Fu Horng, Hsin-fei Meng, Jow-tsong Shy, Hua-hsien Liao, Chia-ming Yang, Chien-cheng Liu, Sheng-fu Horng, Hsin-Fei Meng, and Jos-Tsong Shy. Dynamics and reversibility of oxygen doping and de-doping for conjugated polymer. *Journal of Applied Physics*, 103:104506, 2008. doi:10.1063/1.2917419.

[213] Julia Schafferhans, Andreas Baumann, Alexander Wagenpfahl, Carsten Deibel, and Vladimir Dyakonov. Oxygen doping of P3HT:PCBM blends: Influence on

trap states, charge carrier mobility and solar cell performance. *Organic Electronics*, 11, 2010. doi:10.1016/j.orgel.2010.07.016.

[214] Andrea Seemann, H.-J. Egelhaaf, Christoph J. Brabec, and Jens A. Hauch. Influence of oxygen on semi-transparent organic solar cells with gas permeable electrodes. *Organic Electronics*, 10(8):1424–1428, 2009. doi:10.1016/j.orgel.2009.08.001.

[215] L. Lüer, H.-J. Egelhaaf, D. Oelkrug, G. Cerullo, G. Lanzani, B.-H. Huisman, and D. de Leeuw. Oxygen-induced quenching of photoexcited states in polythiophene films. *Organic Electronics*, 5(1):83 – 89, 2004. doi:10.1016/j.orgel.2003.12.005.

[216] Carsten Deibel, Daniel Mack, Julien Gorenflot, Achim Schöll, Stefan Krause, Friedrich Reinert, Daniel Rauh, and Vladimir Dyakonov. Energetics of excited states in the conjugated polymer poly(3-hexylthiophene). *Physical Review B*, 81:085202, 2010. doi:10.1103/PhysRevB.81.085202.

[217] Henning Sirringhaus, PJ Brown, RH Friend, Martin Meedom Nielsen, Klaas Bechgaard, BMW Langeveld-Voss, AJH Spiering, Rene AJ Janssen, EW Meijer, P Herwig, et al. Two-dimensional charge transport in self-organized, high-mobility conjugated polymers. *Nature*, 401(6754):685, 1999. doi:10.1038/44359.

[218] Markus Hallermann, Stephan Haneder, and Enrico Da Como. Charge-transfer states in conjugated polymer/fullerene blends: Below-gap weakly bound excitons for polymer photovoltaics. *Applied Physics Letters*, 053307(93):053307, 2008. doi:10.1063/1.2969295.

[219] Phaedon Avouris and Richard Martel. Progress in carbon nanotube electronics and photonics. *MRS Bulletin*, 35(4):306–313, 2010. doi:10.1557/mrs2010.553.

[220] J. A. Misewich, R. Martel, Ph. Avouris, J. C. Tsang, S. Heinze, and J. Tersoff. Electrically induced optical emission from a carbon nanotube fet. *Science*, 300(5620):783–786, 2003. doi:10.1126/science.1081294.

[221] R. Martel, V. Derycke, C. Lavoie, J. Appenzeller, K. K. Chan, J. Tersoff, and Ph. Avouris. Ambipolar electrical transport in semiconducting single-wall carbon nanotubes. *Phys. Rev. Lett.*, 87:256805, Dec 2001. doi:10.1103/PhysRevLett.87.256805.

Danksagung

- Ich möchte als erstes Prof. Vladimir Dyakonov dafür danken, dass er es mir ermöglichte vom Bachelor bis zum Doktor am Lehrstuhl der EP VI bleiben zu können. Es war eine wunderschöne Zeit, in der ich weitestgehend selbständig basteln und arbeiten durfte. Danke auch, dass ich das Ministry of Fun gründen durfte, um alle Arten von Lehrstuhlaktivitäten und Ausflügen zu planen.
- Ganz besonders danke ich Hex, alias Dr. Andreas Sperlich, der mir von Anfang an als Betreuer zur Seite stand. Ich durfte so sehr viel über Physik lernen und das mit Liebe gebaute Spektrometer weiterführen, Danke.
- Dank geht auch an Dr. Stefan Väth, der mir unter anderem gezeigt hat, wie man organische Solarzellen baut und Organik zum Leuchten bringt, super geil!
- Unbedingt danken möchte ich auch meinen Freunden aus der Chemie, darunter Eileen Welz und Sara Wirsing, mit denen ich einige Zeit das Graduiertenkolleg repräsentieren durfte, und natürlich allen anderen im Graduiertenkolleg, von denen ich sehr viel über Chemie lernen durfte. Hierbei möchte ich besonders Florian Oberndorfer, Florian Späth, Klaus Eckstein und Prof. Tobias Hertel für die herausragende Zusammenarbeit mit Kohlenstoff Nanoröhren danken.
- Herzlichen Dank auch an André Thiem-Riebe und Valentin Baianov für ihre Hilfe bei meinen technischen Fragen, Problemen und meinen Sonderwünschen bei den Laseraufbauten. Diesbezüglich danke ich auch der Elektronik- und Mechanikwerkstatt, ohne die vieles niemals hätte umgesetzt oder repariert werden können.
- Ich möchte explizit Niko, Becky und Luditschka danken! Dank Nikolaius Bonus bin ich nicht nur zu einem umfassenderen Wissen über OLEDs und Spins gekommen, nein ich bin jetzt auch noch international sprachlich überragend aufgestellt und kann dem elitären Geist meines Abschlusses gerecht werden. Qui audet adipiscitur! Danke auch an Becky, die sich einfach alles aus dem Studium merken konnte und ich nicht in meinen Unterlagen wühlen musste. Und Luditschka, du weißt einfach alles, danke für die Erklärungen zur Fehlerrechnung, Mathematika Simulationen und optischen Spektren aller Art. Erwähnenswert sind auch die hochanalytischen Diskussionen mit Chris Kas (Meister der Labplaylist) und un-

seren Mitstreitern aus der Pflaum Gruppe zur Maximierung der Effizienz (zum Fortschritt ins nächste Zeitalter). Danke auch für die Hilfe bei der Justage von Set-Up K.

- Ohne die Bananen hätte ich es nicht geschafft!
- Besonders erwähnen möchte ich auch Bernd Sturdza! Unsere Zusammenarbeit hat nicht nur ein geiles Paper produziert, in dem wir wunderschöne Physik zeigen, sondern auch echte Astralkörper dank unserer Laborfitness. In diesem Zusammenhang möchte ich auch allen anderen des EP6i Sportteams danken, welches auf dem Fußball- und Volleyball Feld geglänzt, aber auch an der Klimmzugstange, geleitet von Krass Fitti, übermenschliches geleistet hat.
- Ich danke auch dem Internet, für die geduldige Beantwortung all meiner Fragen.
- Um außerhalb des geschützten Universitären Raums überleben zu können, danke ich Davide und Marius für all die Hilfe und gemeinsame Zeit.
- Abschließend möchte ich vor allem meiner Familie danken, Mama und Papa Auth, die eine Menge Zeit und Geld in mich investiert haben, um jetzt einen Doktor in der Familie zu haben, der irgendwie doch lieber Radfahren geht als alles andere. Und natürlich auch Alex und Mimi, die mir den Rücken frei hielten, wenn ich mal wieder nicht genau wusste wo der gerade ist.
- _____bitte freilassen, im Gedenken und Dank an alle Vergessenen.